Astrophysical neutrinos at the low and high energy frontiers

by

Lili Yang

A Dissertation Presented in Partial Fulfillment
of the Requirements for the Degree
Doctor of Philosophy

Approved November 2013 by the
Graduate Supervisory Committee:

Cecilia Lunardini, Chair
Ricardo Alarcon
Igor Shovkovy
Francis Timmes
Tanmay Vachaspati

ARIZONA STATE UNIVERSITY

December 2013

ABSTRACT

For this project, the diffuse supernova neutrino background (DSNB) has been calculated based on the recent direct supernova rate measurements and neutrino spectrum from SN1987A. The estimated diffuse $\bar{\nu}_e$ flux is $\sim 0.10 - 0.59\ cm^{-2}s^{-1}$ at 99% confidence level, which is 5 times lower than the Super-Kamiokande 2012 upper limit of 3.0 $cm^{-2}s^{-1}$, above energy threshold of 17.3 MeV. With a Megaton scale water detector, 40 events could be detected above the threshold per year.

In addition, the detectability of neutrino bursts from direct black hole forming collapses (failed supernovae) at Megaton detectors is calculated. These neutrino bursts are energetic and with short time duration, $\sim$ 1s. They could be identified by the time coincidence of $N \geq 2$ or $N \geq 3$ events within 1s time window from nearby (4 – 5 Mpc) failed supernovae. The detection rate of these neutrino bursts could get up to one per decade. This is a realistic way to detect a failed supernova and gives a promising method for studying the physics of direct black hole formation mechanism.

Finally, the absorption of ultra high energy (UHE) neutrinos by the cosmic neutrino background, with full inclusion of the effect of the thermal distribution of the background on the resonant annihilation channel, is discussed. Results are applied to serval models of UHE neutrino sources. Suppression effects are strong for sources that extend beyond z$\sim$ 10. This provides a fascinating probe of the physics of the relic neutrino background in the unexplored redshift interval z $\sim$ 10 – 100.

Ultimately this research will examine the detectability of DSNB, neutrino bursts from failed supernovae and absorption effects in the neutrino spectrum.

ACKNOWLEDGEMENTS

This thesis is not only about what I have studied, but also it is a milestone in my academic career. I would never been able to finish it without the guidance of my advisor, help from my committee members, and support from family and friends.

First and foremost, I would like to express my deepest gratitude to my advisor, Dr. Cecilia Lunardini, for her continuous support and help. I still remember the first time we met in Prof. Ritchie's office on my first day of Ph.D.. Back to that time, I never thought about doing research on neutrino physics, and I even never thought about being a theorist. She is such a patient, kind and warm person with immense knowledge. She inspired me to start my physics career. My appreciation can't be conveyed in words. I would say the luckiest thing these years for me has been to study with her.

I would like to thank the committee members: Prof. Ricardo Alarcon, Prof. Igor Shovkovy, Prof. Francis Timmes, Prof. Tanmay Vachaspati for their encouragement, insightful comments and invaluable advice. I am grateful to Dr. Eray Sabancilar for sharing his knowledge with me.

Last but not least, I would like to thank my parents for their understanding and unconditional support through my degree. I wish to thank my best friend Di Fang for all the help, camaraderie, entertainment and caring. Thanks to my dogs, for always waiting for me at home; no matter how late I work, always being with me.

TABLE OF CONTENTS

Chapter Page

Chapter Page

LIST OF TABLES

LIST OF FIGURES

Figure Page

Figure Page

Figure Page

Figure Page

Figure Page

Chapter 1

Introduction

1.1 Neutrino physics and astrophysics

During the early decades of the last century, experiments on radioactive nuclei demonstrated that in beta decay positrons only take off about half of the energy expected to be released in the nuclear decay. In 1930, W. Pauli proposed that a new type of particle, one which was electrically neutral and at least as light as an electron, would be the solution to the energy crisis. He made his hypothesis, two years before Chadwick discovered the neutron. This particle was originally called the neutral one.

In 1934, Enrico Fermi proposed his famous model for beta decay processes, incorporating the neutrino, which in Italian means the "the little neutral one". This famous theory motivated the study of weak interaction. After more than 20 years, in 1956, Fred Reines and Clyde Cowan [1] announced that the first neutrino was detected in a liquid scintillator detector with the Savannah River nuclear reactor. The neutrino was later known as the partner of the electron. In 1958, Maurice Goldhaber, Lee Grodzins, and Andrew Sunyar at Brookhaven National Laboratory demonstrated neutrinos to possess left-handed helicity [2]. Helicity is one of the most important properties of neutrinos. It interprets the relation between the orientation of the neutrino's spin and the direction of its linear momentum. For neutrinos, left-handed helicity means that the spin vector points opposite to the direction of the linear momentum vector.

In 1962, the second type of neutrino, the muon neutrino, was discovered by Jack Steinberger, Leon Lederman and Melvin Schwartz at Alternating Gradient Synchrotron (AGS) [3]. In 1968, the deep underground experiment in the Homestake mine in South Dakota observed the first electron neutrinos from the sun. This led to the solar neutrino problem, which is that detected neutrinos are about one third of the expected amount in the solar models.

In 1976, the third type of lepton, the tau, was discovered in the SLAC, Stanford Linear Accelerator Center [4]. It was confirmed that there exists a third specie of neutrino, ν_τ, accompanying the tau. In 1987, large underground water detectors, the Kamiokande in the Kamioka mine in Japan and IMB in the Morton salt mine in the US, detected a burst of neutrinos from Supernova 1987A.

In 1989, experiments at Large Electron-Positron (LEP) accelerator at CERN in Switzerland and the SLC at SLAC determined that there are only three species of active light neutrinos, ν_e, ν_μ and ν_τ. In 1991-1992, Soviet-American Gallium Experiment (SAGE) in Russia and Gallium Experiment (GALLEX) in Italy confirmed solar neutrino deficit in radiochemical experiments. In 1998, after analyzing more than 500 days of data, the Super-Kamiokande collaboration announced that neutrinos oscillate and have non-zero mass at the Neutrino '98 conference in Japan.

In July 2000, the Direct Observation of the NU Tau (DONUT) at Fermilab directly observed a tau neutrino for the first time. In 2001, the Sudbury Neutrino Observatory (SNO) in Canada, detected all three types of neutrinos produced by the sun, and provided strong evidence that neutrino oscillations are the cause of the solar neutrino problem [5].

In recent years, the oscillation parameter θ_{13} has been obtained using the data from the reactor experiments Daya Bay in China [6], Reno in Korea [7], Double Chooz in France [8] and the accelerator experiment T2K in Japan [9]. In 2013, IceCube [10] reported the observation of two PeV scale neutrino events, which are the highest energies so far.

In the next decade, we hope to detect extragalactic neutrinos with ultra high energy in such experiments as IceCube, FORTE et cetera. There still remain many questions waiting to be explored, like the absolute scale of neutrino mass, the mass hierarchy, and the Dirac/Majorana nature of the mass. There also exists debate about the sizes or roles in nature of three CP-violating phases, whether neutrinos have nonzero electromagnetic moments, if there are additional neutrino species, and if the universe has a lepton asymmetry.

1.2 Physics of neutrinos

It is well known that the neutrino is one of the fundamental particles that make up the universe, with spin half. Neutrinos are the only fermions carrying no electric charge; therefore they are not affected by electromagnetic force. They are only affected by gravity and by the weak subatomic force involving the exchange of W and Z bosons.

It is a widely-accepted experimental fact that the neutrinos are of three varieties or flavors. Each type is accompanied by its antineutrino which has a different helicity (right-handed). Each neutrino flavor is associated with a charged lepton: electron ν_e and $\bar{\nu}_e$, muon ν_μ and $\bar{\nu}_\mu$, and tauon ν_τ and $\bar{\nu}_\tau$.

Neutrino oscillation experiments have provided compelling evidence that neutrinos change flavor during their propagation. The probability of a neutrino changing flavor depends on the neutrino energy and distance traveled. This will be elaborated in detail later. This phenomenon can only be explained by the unequal masses of neutrinos. Their masses can't all be zero. In other words, neutrinos have distinct masses and mixing. In our study, a three-flavor paradigm is being considered.

1.2.1 Neutrino masses

In the last decades, various experiments have tried to determine the absolute neutrino mass scale. This scale is very important for describing the role of neutrinos in the evolution of the universe. There are three different approaches – cosmological probes (cosmic microwave background and large-scale structure constraints), neutrinoless double β-decay, and direct neutrino mass determination (β decay) [11]. Up until now, the upper limits on the sum of the neutrino masses were $\sum m_\nu < 0.23 eV$ at 95% confidence level by the most recent Planck data [12].

The neutrino oscillations indicate that neutrinos have a non-vanishing mass, with the assumption of three neutrinos and no exotic neutrino interaction. This means that the mass eigenstates ν_i (i=1,2,3) are not equal and are not identical to the flavor eigenstates ν_α ($\alpha = e, \mu, \tau$). Oscillation probabilities depend on the mixing matrix connecting the two bases and on the mass squared differences $\Delta m_{ij}^2 = m_i^2 - m_j^2$. With the recent analysis of neutrino data, the best fit Δm_{21}^2 = $7.5 \times 10^{-5} eV^2$ and $|\Delta m_{31}^2|$ = $2.35 \times 10^{-3} eV^2$ have been measured. There are two possibilities for ordering of neutrino mass eigenstates:

(1). Normal hierarchy, where $m_1 < m_2 < m_3$. In this case, at least two of the three masses are not zero, $m_3 \simeq \sqrt{\Delta m_{23}^2} \gtrsim 4.8 \times 10^{-2}$ eV and $m_2 \gtrsim 8.6 \times 10^{-3}$ eV. The lightest neutrino mass is not constrained.

(2). Inverted hierarchy, where $m_3 < m_2 \simeq m_1$. Here we get $m_1 \simeq m_2 \simeq \sqrt{\Delta m_{23}^2} \gtrsim$ 4.8×10^{-2} eV.

Fig. 1.1 illustrates how the three neutrino masses change with the lightest mass in the two hierarchy cases (i.e. normal hierarchy $m_2^2 = \Delta m_{21}^2 + m_1^2, m_3^2 = \Delta m_{31}^2 + m_1^2$). We could distinguish between a hierarchical mass spectrum, where at least two of the masses differ by one or more orders of magnitude, and a degenerate spectrum with masses of comparable values. As the figure shows, the degenerate case requires the smallest mass ($m_{\text{min}} = m_1$ or m_3 depending on the hierarchy) to exceed a few times 10^{-2} eV.

1.2.2 Neutrino mixing in vacuum

A neutrino is created by the weak interaction with flavor α (α = e, μ, τ). Analogous to quark mixing, neutrino mass eigenstates ν_i are connected to flavor eigenstates ν_α by a

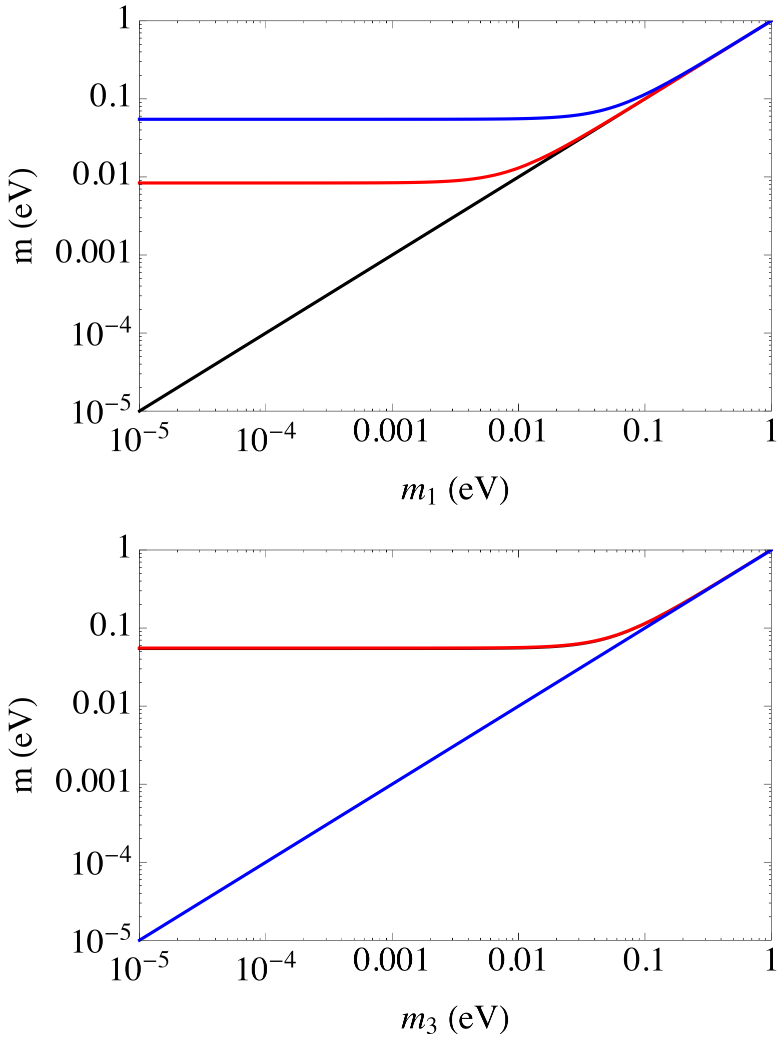

Figure 1.1: The three neutrino masses as a function of the minimum mass m_{min}. The upper (bottom) panel is for the normal (inverted) hierarchy, where $m_{\text{min}} = m_1$ ($m_{\text{min}} = m_3$).

unitary matrix U called the Pontecorvo-Maki-Nakagawa-Sakata matrix (PMNS matrix) [13, 14, 15]:

$$\begin{pmatrix} \nu_e \\ \nu_\mu \\ \nu_\tau \end{pmatrix} = \begin{pmatrix} U_{e1} & U_{e2} & U_{e3} \\ U_{\mu 1} & U_{\mu 2} & U_{\mu 3} \\ U_{\tau 1} & U_{\tau 2} & U_{\tau 3} \end{pmatrix} \cdot \begin{pmatrix} \nu_1 \\ \nu_2 \\ \nu_3 \end{pmatrix} \tag{1.1}$$

with

$$U = \begin{pmatrix} c_{12}c_{13} & s_{12}c_{13} & s_{13}e^{-i\delta} \\ -s_{12}c_{23} - c_{12}s_{23}s_{13}e^{i\delta} & c_{12}c_{23} - s_{12}s_{23}s_{13}e^{i\delta} & s_{23}c_{13} \\ s_{12}s_{23} - c_{12}s_{23}s_{13}e^{i\delta} & -c_{12}s_{23} - s_{12}c_{23}s_{13}e^{i\delta} & c_{23}c_{13} \end{pmatrix} \tag{1.2}$$

where $s_{ij} = sin\theta_{ij}$, $c_{ij} = cos\theta_{ij}$ (i, j= 1,2,3), and the three θ_{ij} are the mixing angles. We have $\sin^2\theta_{12} \simeq 0.31$, $\sin^2\theta_{23} \simeq 0.42$, and $\sin^2\theta_{13} \simeq 0.025$ [12], and δ is CP-violating phases. For Majorana neutrinos, there are two additional Majorana phase. The neutrino mass splittings and mixing for the two hierarchies are shown in Fig. 1.2.

Given that θ_{13} is small, and θ_{23} is very close to $\pi/4$, ν_3 is nearly a 50-50% mixture of ν_μ and ν_τ with a small ν_e component, while ν_1 and ν_2 have large admixtures of all the three flavors (Fig. 1.2).

According to Eq. 1.1, the neutrino flavor states are the superpositions of the neutrino mass states,

$$|\nu_\alpha\rangle = \sum_{i=1}^{3} U_{\alpha i}|\nu_i\rangle \tag{1.3}$$

The neutrino mass eigenstates $|\nu_i\rangle$ in vacuum evolve in time according to

$$|\nu_i(t)\rangle = |\nu_i(0)\rangle e^{-iE_it} = |\nu_i(0)\rangle e^{-i(p_i+\frac{m_i^2}{2p_i})t}, \tag{1.4}$$

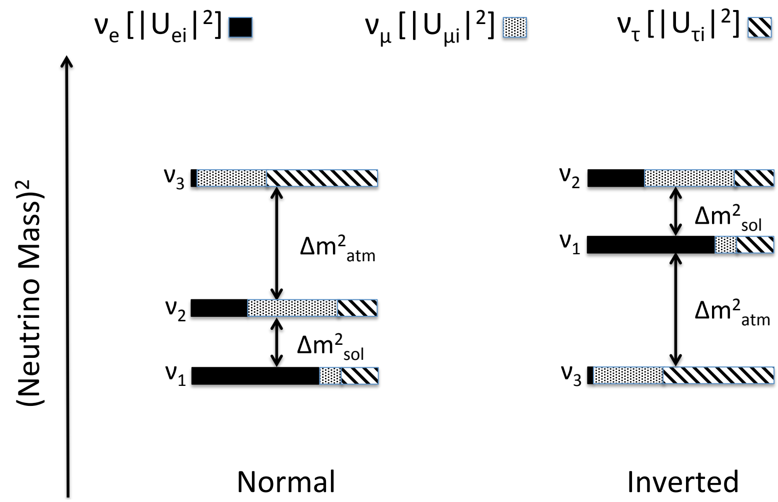

Figure 1.2: A graphical illustration of the mixing between mass and flavor eigenstates. The boxes represent the mass eigenstates, $i = 1,2,3$, the shaded regions represent their flavor admixtures $|U_{\alpha i}|^2$ for $\alpha = e, \mu, \tau$, $|\Delta m^2_{\text{atm}}| = |\Delta m^2_{31}| \approx |\Delta m^2_{32}| = 2.4 \times 10^{-3}$ eV^2 and $\Delta m^2_{\text{sol}} = \Delta m^2_{21} = 7.5 \times 10^{-5}$ eV^2.

where the neutrinos are considered relativistic $m_i \ll E_i$. The time evolved neutrino flavor eigenstate has the form:

$$|\nu_\alpha(t)\rangle = \sum_i U_{\alpha i} e^{-iE_i t} |\nu_i(0)\rangle \tag{1.5}$$

Therefore, the time-dependent oscillation probability for a flavor conversion $\nu_\alpha \to \nu_\beta$ is then

$$P(\nu_\alpha \to \nu_\beta, t) = |A(\nu_\alpha \to \nu_\beta, t)|^2 = |\langle \nu_\beta | \nu_\alpha(t) \rangle|^2 \tag{1.6}$$

$$= \sum_i \sum_j U_{\alpha i} U^*_{\alpha j} U^*_{\beta i} U_{\beta j} e^{-i(E_i - E_j)t} \tag{1.7}$$

Then the survival probability can be obtained as

$$P(\nu_\alpha \to \nu_\alpha) = 1 - \sum_{\alpha \neq \beta} P(\nu_\alpha \to \nu_\beta) \tag{1.8}$$

In the absence of matter effect, the oscillation probability in vacuum is given by

$$\begin{aligned} P(\nu_\alpha \to \nu_\beta) = \quad & \delta_{\alpha\beta} - 4\sum_{i>j=1}^{3} Re(U_{\alpha i}U^*_{\beta i}U^*_{\alpha j}U_{\beta j})sin^2\big(\frac{\Delta m^2_{ij}L}{4E}\big) \\ + \quad & 4\sum_{i>j=1}^{3} Im(U_{\alpha i}U^*_{\beta i}U^*_{\alpha j}U_{\beta j})sin\big(\frac{\Delta m^2_{ij}L}{4E}\big)cos\big(\frac{\Delta m^2_{ij}L}{4E}\big) \end{aligned} \quad (1.9)$$

The general probability formulae are quite complex and really depend on the sign of the mass differences. In a three-neutrino hierarchical spectrum, consider that one mass splitting is dominant, say $|\Delta m^2_{21}| \ll |\Delta m^2_{31}| \simeq |\Delta m^2_{32}|$. Neglecting the effects due to Δm^2_{21}, where $\frac{\Delta m^2_{21}}{2E}L \ll 1$, the transition probability of $\nu_\alpha \to \nu_\beta$ over the long baselines L can be simplified as

$$P(\nu_\alpha \to \nu_\beta) = 4|U_{\alpha 3}|^2|U_{\beta 3}|^2 sin^2\big(\frac{\Delta m^2_{31}}{4E}L\big) \quad (1.10)$$

This case is relevant for atmospheric, reactor and accelerator neutrino experiments, with $\Delta m^2_{31} \approx \Delta m^2_{32} = \Delta m^2_{atm}$, and $\theta_{atm} \simeq \theta_{23}$. In the other case, $\frac{\Delta m^2_{31}}{2E}L \simeq \frac{\Delta m^2_{32}}{2E}L \gg 1$, the oscillations due to Δm^2_{31} and Δm^2_{32} are averaged out. Then the ν_e survival probability is

$$P(\nu_e \to \nu_e) \simeq c^4_{13}\Big[1 - \frac{1}{2}sin^2 2\theta_{12} sin^2\big(\frac{\Delta m^2_{21}}{4E}L\big)\Big] + s^4_{13} \quad (1.11)$$

This case is relevant for reactor neutrino experiments [17].

There are two ways to study neutrino oscillations, appearance or disappearance mode. The probability of a neutrino produced as a given flavor α with energy E, propagating a sufficient distance L from the source and then detected as the same flavor, is called survival probability. If in an experiment, only ν_μ flux is produced at the source and oscillations occur on the way to the distant detector site, one would observe the disappearance of ν_μ as a result. Disappearance behavior has been established by solar ν_e, atmospheric ν_μ and $\bar{\nu}_\mu$ and reactor $\bar{\nu}_e$ in the solar neutrino, Super-Kamokande and KamLAND experiments. Appearance of ν_e in a ν_μ beam has also been observed

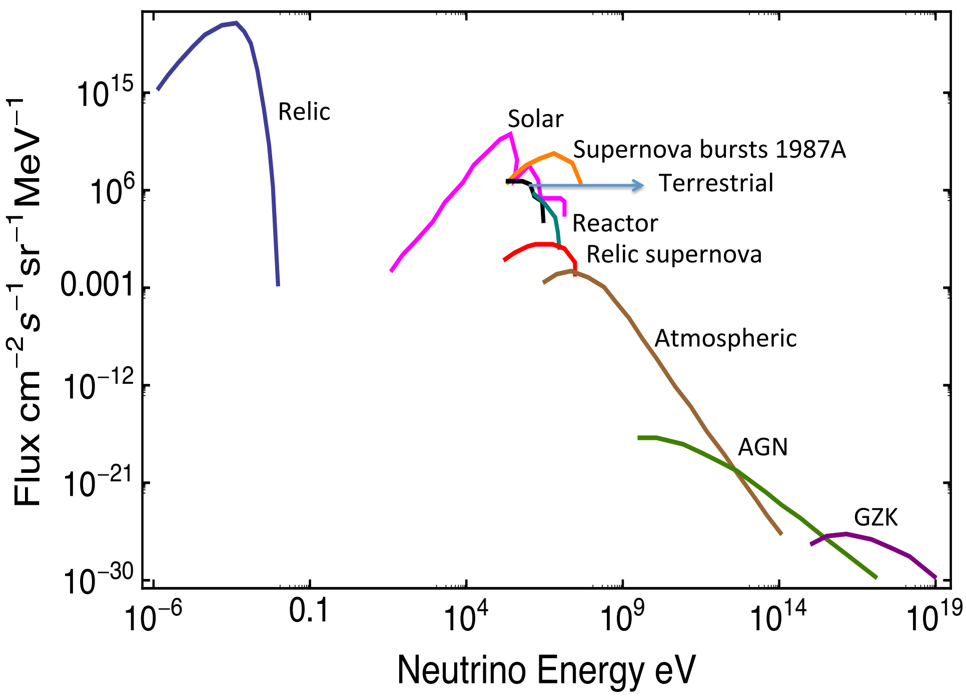

Figure 1.3: Neutrino spectra from the possible neutrino sources.

in T2K and MINOS experiments [16]. After comparing the ratio of the number of observed neutrino events to the expected neutrino of each flavor, according to the transition probability or survival probability formula, one can obtain the mass square difference and mixing angles.

1.3 Neutrino sources

As seen in Fig. 1.3, possible sources of neutrinos include the early universe, the sun, supernovae, natural radioactivity, man-made reactor and accelerator, supernovae remnants, the atmosphere, astrophysical accelerators of cosmic rays. Excepting neutrinos from cosmological backgrounds and baryonic accelerator, all other types have already been detected with the energy band from keV to a few TeV. I will briefly introduce all these neutrino sources below.

1.3.1 Cosmological neutrino background

In the early universe, very soon after the big bang, neutrinos were kept in thermal equilibrium via weak interactions with protons, electrons and neutrons. As the universe expanded and cooled down, the interaction rates decreased rapidly. When the temperature of universe dropped down to $\sim$ MeV, and the mean interaction time for $\nu\bar{\nu} \to e^+e^-$ became longer than the age of the universe, neutrinos decoupled from thermal plasma and streamed away freely.

After neutrino decoupling, only electrons, positrons and photons were left in thermal equilibrium. Photons are heated up by the annihilation of positrons and electrons ($e^+e^- \to 2\gamma$). Applying the conservation of entropy, $S \propto g_i T_i^3 = g_f T_f^3$, the ratio of T_i/T_f can be calculated. Here $g_{i,f}$ is the effective number of particles. For the initial condition, $g_i = g_{e^\pm} + g_s$, with $g_s = 2$ accounting for photons with 2 spin states, and $g_{e^\pm} = 2 \times 2 \times 7/8$ is for the electrons and positrons. The first 2 originates from particle and antiparticle; the second 2 is due to the possible numbers of orientation of the particle spin and the third part 7/8 is because electron/positron is Fermion. Since neutrinos don't take part in the interactions, they keep the temperature as T_i. Therefore the relation between the present neutrino and photon temperature is $T_\nu = (\frac{4}{11})^{1/3} T_\gamma \simeq 1.697 \times 10^{-4}$eV.

These relic neutrinos fill in the whole universe, and are also called cosmic neutrino background (CνB). They only weakly interact with matter and their temperature today is extremely small, ~ 1.945K. Therefore, it's extremely difficult to directly detect them.

Assuming a Friedmann Robertson Walker (FRW), ΛCDM universe, with the Hubble parameter, the universe expansion rate is,

$$H(z) = \frac{\dot{a}}{a} = H_0 \sqrt{\Omega_{\rm m}(1+z)^3 + \Omega_\Lambda}, \tag{1.12}$$

where $H_0 = 70.4$ Mpc/km/s, $a = 1/(1+z)$ is the scale factor, z is the cosmological redshift, and $\Omega_{\rm m} = 0.272$ and $\Omega_\Lambda = 0.728$ are the fractions of the energy density of matter and dark energy respectively [18]. Natural units are used, with $c = \hbar = 1$, setting Boltzmann's constant $k = 1$. Differentiating the scale factor, we obtain the relation between the cosmological time, t, and the redshift, z,

$$dt = \frac{dz}{(1+z)H(z)}, \tag{1.13}$$

and the comoving distance is

$$dr = \frac{dz}{H(z)} , \tag{1.14}$$

so that the comoving volume is given by

$$dV_{\rm c} = r^2 dr d\Omega , \tag{1.15}$$

where $r = r(z)$ is the integral of Eq. (1.14) from present epoch to redshift z. Thus, the physical volume is simply $dV(z) = dV_c/(1+z)^3$.

Standard cosmology predicts the relic abundance of neutrinos with a thermal spectrum, similar to the cosmic microwave background (CMB) photons. Thermal equilibrium is provided by weak interactions, hence the relic neutrinos are produced in flavor eigenstates. The number density of the CνB for a single neutrino specie, is given by the Fermi-Dirac distribution with zero chemical potentials at temperature T as

$$dn(p,T) = \frac{d^3p}{(2\pi)^3} \frac{1}{e^{p/T}+1}, \tag{1.16}$$

where p is the relic neutrino momentum. Therefore, the number density of each neutrino specie is n_ν =56 cm^{-3} at present time. And the number density of relic neutrinos at redshift z will be expressed as $n_\nu(1+z)^3$

1.3.2 solar neutrino

The sun like other stars, creates its energy via nuclear fusion, whose basic fuel is hydrogen. The solar neutrinos are generated by two principal mechanisms: CNO cycle and Proton-Proton (pp) chain. The pp chain produces most of the neutrino fluxes via the reactions

$$p+p \rightarrow d+e^{+}+\nu_e \tag{1.17}$$

$$p+e+p \rightarrow d+\nu_e \tag{1.18}$$

$$e+^{7}Be \rightarrow {}^{7}Li+\nu_e \tag{1.19}$$

$$^{8}B \rightarrow {}^{8}Be^{*}+e^{+}+\nu_e \tag{1.20}$$

$$^{3}He+p \rightarrow {}^{4}He+e^{+}+\nu_e \tag{1.21}$$

The corresponding produced neutrinos are so called pp, pep, ^{7}Be, ^{8}B and hep neutrinos [19]. Their energy can extend up to 19MeV. In the CNO cycle electron capture processes occur in the reactions [20]:

$$^{13}N+e^{-} \rightarrow {}^{13}C+\nu_e, \tag{1.22}$$

$$^{15}O+e^{-} \rightarrow {}^{15}N+\nu_e, \tag{1.23}$$

$$^{17}F+e^{-} \rightarrow {}^{17}O+\nu_e \tag{1.24}$$

The contribution to the neutrino flux from the CNO cycle is small. In a water Cherenkov detector, solar neutrinos leave a directional signature, therefore they can be distinguished from other neutrino fluxes.

1.3.3 Supernova 1987A

On February 24th, 1987, a bright supernova of type IIP was observed. It occurred in the Large Magellanic Cloud, approximately 51.4 kpc from the earth. The neutrino signal arrived on earth two to three hours earlier than visible light. It was the first time scientists observed neutrinos from a supernova. This observation provided strong evidence to support the theoretical models of the mechanism behind the explosion.

SN1987A was observed by the underground neutrino detectors, Irvine-Michigan-Brookhaven (IBM) in US, Kamiokande II in Japan, and Baksan Scintillator Telescope in Russia. This event is considered as the beginning of neutrino astronomy. The detected neutrino signal provided the most direct evidence about supernova neutrino emission, although we still do not know if SN1987A is a typical supernova. In our study, we use SN1987A data as an input for calculating the diffuse supernova neutrino background. A detailed discussion of this will follow in Chapter 2.

1.3.4 Terrestrial neutrinos

Terrestrial electron antineutrinos are mostly produced by natural radioactive decays in the chains of ^{238}U, ^{232}Th and ^{40}K inside the Earth, which are accompanied by radiogenic heat. There are two experiments - KamLAND in Japan and Borexino in Italy - measuring the geo-neutrinos right now. Their spectrum gets up to 3.26 MeV [21].

1.3.5 Man-made neutrinos

Man-made neutrinos refer to neutrinos from nuclear reactors and particle accelerators, with energies up to 14 MeV. These $\bar{\nu}_e$s are produced by β^- decay of neutron-rich fission products of ^{235}U, ^{238}U, ^{239}Pu and ^{241}Pu in nuclear reactors [22]. The reactor neutrino flux arriving at the detector strongly depends on the distance between the reactors, generally several nuclear plants, and detectors. Fig. 1.4 shows the reactor neutrino flux at Kamioka in Japan and Homestake in US. The reactor neutrino flux determines the energy threshold for the detection of diffuse supernova neutrinos.

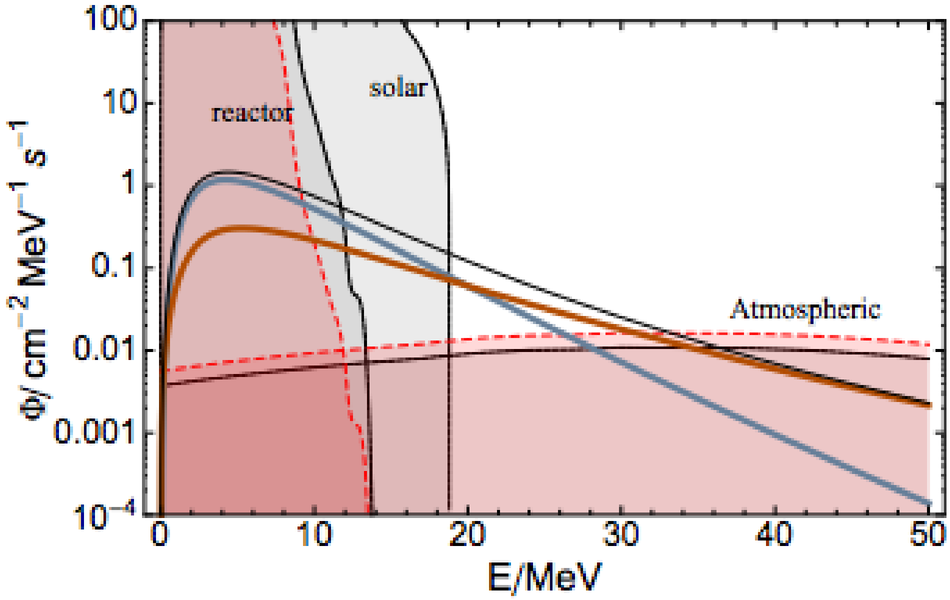

Figure 1.4: Taken from Fig. 4 of [23]. Background $\bar{\nu}_e$ fluxes from atmosphere and reactors and ν_e fluxes from the sun and atmosphere for the Homestake (dashed, red) and Kamioka (solid, grey). The ν_e and $\bar{\nu}_e$ fluxes from the atmosphere are similar, so one of them is shown in the figure. At 10 MeV, the lower to upper curves (orange, blue and black) represent the signal $\bar{\nu}_e$ fluxes from black hole forming collapses, neutron star forming collapses and the total. These fluxes are with Shen et al. equation of state, the survival probability is 0.68, and the fraction of neutron star forming collapses is 0.78. The detailed discussion will be seen in Chapter 3.

1.3.6 Diffuse supernova neutrino background

Supernova relic neutrinos, or diffuse supernova neutrino background, come from all the core-collapse supernovae in the sky, and compose an isotropic flux. The study of the diffuse supernova neutrino background (DSNB) is discussed in Chapter 2 in detail. It is crucial to distinguish it from the backgrounds like atmospheric, solar, and reactor neutrinos in the energy range of $\leq 35 MeV$, as seen in Fig. 1.4.

1.3.7 *Atmospheric neutrinos*

Atmospheric neutrinos are produced when primary cosmic rays hit the Earth's atmosphere, interacting with nuclei. The shower of hadrons produced (mostly pions) takes up to 98%, and electrons created take 2% of the primary cosmic ray energy. The secondary hadrons decay into electron and muon neutrinos. The dominant decay chains are

$$\pi^+ \to \mu^+ \nu_\mu \quad \mu^+ \to e^+ \nu_e \bar{\nu}_\mu \tag{1.25}$$

$$\pi^- \to \mu^- \bar{\nu}_\mu \quad \mu^+ \to e^- \bar{\nu}_e \nu_\mu \tag{1.26}$$

Depending on the energy of the primary cosmic rays, kaon decay also contributes to the neutrino fluxes in the way of

$$K^\pm \to \mu^\pm \nu_\mu (\bar{\nu}_\mu) \tag{1.27}$$

$$K_L \to \pi^\pm e^\pm \nu_e (\bar{\nu}_e) \tag{1.28}$$

Atmospheric neutrino studies is one of the most important fields in neutrino physics. The atmospheric $\bar{\nu}_e$ flux has the same isotropic distribution as the DSNB, and is the dominant neutrino background, which exceeds the DSNB at energy higher than 30-40 MeV. The atmospheric neutrino flux depends on the location of the detector. Here I use the flux calculated by the FLUKA Monte Carlo simulation [24], which can be seen in Fig. 1.4 for Kamioka.

1.3.8 *GZK neutrinos*

The extremely high energy cosmic rays, E $> 5 \times 10^{19}$ eV, collide with the cosmic microwave background (CMB) photons via the Δ resonance to produce pions as

$$p + \gamma_{CMB} \to \Delta^+ \to n + \pi^+ \tag{1.29}$$

The produced pions would proceed to decay to high energy neutrinos which are called GZK neutrinos after Greisen, Zatseptin and Kuzmin [25, 26]. These neutrinos would point back to their source, freely cross the universe, and are a guaranteed flux of extraterrestrial high energy neutrinos.

1.4 Neutrino detectors

Neutrinos have not been directly observed, because they only interact via the weak interaction. However, the by-products of neutrino interactions with electrons and nuclei can be observed by the detectors. There are three main kinds of technologies involved in neutrino detection: water Cherenkov, liquid argon and liquid scintillator.

1.4.1 Cherenkov detectors

Cherenkov neutrino detectors, like Super-Kamiokande in Japan and IceCube at the South Pole, are designed to observe the Cherenkov photons emitted from the secondary charged particles produced in neutrino interactions in water or ice. Neutrinos observed in the Cherenkov detector interact in two ways: charged-current (CC) interaction, $\nu_l + N \rightarrow l + X$, ($l$ presents the lepton flavor), the leading lepton would be detected; neutral-current (NC) interaction, e.g. the elastic scattering of neutrinos on electrons. Cherenkov radiation is produced when a charged particle traversing a medium at velocity v exceeds the phase velocity of light in that medium (c/n, n is the refractive index of that medium, c is the speed of light in vacuum). The angle (called Cherenkov angle) between the emitted light and the track of the particle is shown in Fig. 1.5. Therefore it can be calculated as

$$cos\theta = \frac{\frac{c}{n}t}{\beta ct} = \frac{1}{n\beta} \tag{1.30}$$

here $\beta =$ v/c, is the ratio of particle velocity and speed of light, which is independent of time. The maximum value of β is 1, so the maximum Cherenkov angle is $cos\theta_{max} = \frac{1}{n}$.

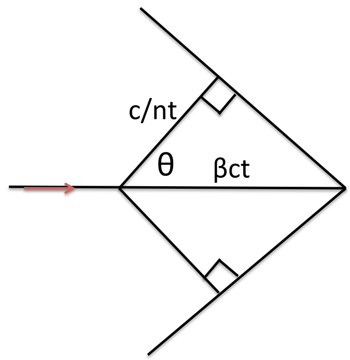

Figure 1.5: The geometry of Cherenkov light and charged particle.

The Super-Kamiokande (SK) experiment is a water Cherenkov neutrino detector in the Kamioka Mine in Gifu, Japan with a fiducial volume of 22.5 kton water and 13000 photomultiplier tubes (PMT). As a supernova neutrino detector, SK mainly detects three types of interactions [27].

(1). Inverse beta decay (IBD)

$$\bar{\nu}_e + p \rightarrow n + e^+ \tag{1.31}$$

This charged current quasi elastic interaction is the most important detection reaction with the largest cross section among all the channels. The emitted positron retains most of the energy of the incoming neutrino, and is detected from its Cherenkov light.

(2). Electron elastic scattering (NC and CC)

$$\nu_l + e^- \rightarrow \nu_l + e^- \tag{1.32}$$

For supernova neutrinos, a small percentage of events are from this interaction. Although the cross section of this interaction is small compared to that of IBD, the recoiled electrons retain the directional information of the incoming neutrinos, unlike the products of the IBD reaction.

(3). Neutral current scattering of neutrinos on oxygen

$$\nu_l +^{16} O \rightarrow \nu_l + \gamma + X \tag{1.33}$$

This reaction produces a nucleus X, which could be ^{15}O or ^{15}N, accompanying the emission of gamma rays.

The background analysis and other issues will be discussed in more detail later.

IceCube is a cubic kilometer water Cherenkov detectors, and consists of 5160 digital optical modules (DOM), installed on 86 strings [10]. Each DOM incorporates a 10” photomultiplier tube. IceCube searches for astrophysical neutrinos with energy from 100 GeV to 10^9 GeV. Events are recorded in the DOM and can be distinguished by two patterns, track-like and spherical modes, as seen in Fig. 1.6. Track-like events originate from neutrino-induced muons produced in ν_μ CC interaction. Cascade events are from electromagnetic (ν_τ decay, ν_e CC interactions) or hadronic showers (τ decay, $\nu_{e,\mu,\tau}$ NC and CC interactions) as shown in Fig. 1.6.

1.4.2 Liquid argon time projection chambers

A liquid argon time projection chamber was first proposed in 1977 [29]. In a large high-purity liquid argon detector, neutrinos interact with argon nuclei and produce charged particles. The ionization charge produced along the charged particle tracks is drifted by a uniform electric field, and signals are collected on wire planes. The data on charge amplitude, wire position, and arrival times are precisely recorded and are used to reconstruct the event [30].

This technique has excellent capacity for tracking and reconstruction. The detector is most sensitive to ν_e via the CC interaction,

$$\nu_e +^{40} Ar \rightarrow X + e^-, \tag{1.34}$$

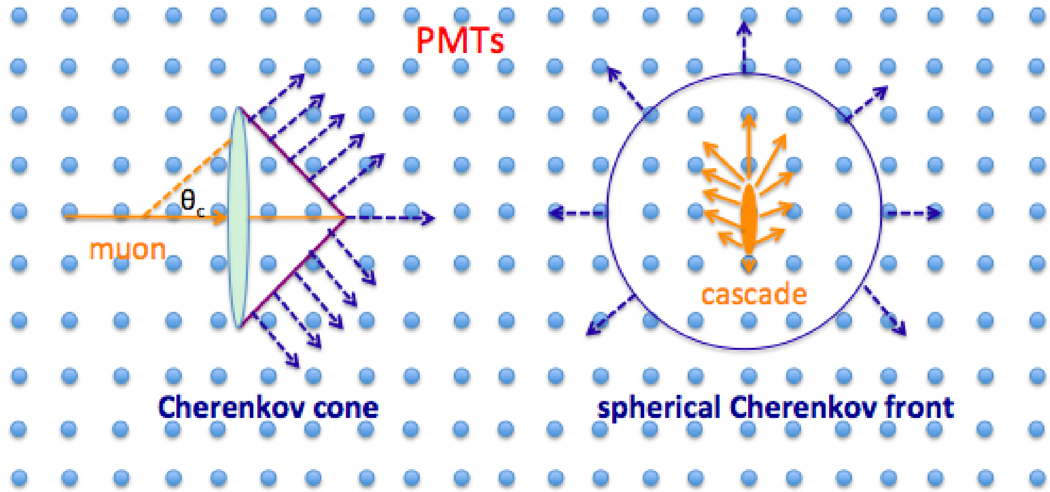

Figure 1.6: Track and cascade events geometry.

where X presents any possible products. NC scattering and electron scattering on ^{40}Ar are also possible [31].

1.4.3 Liquid scintillator detectors

Liquid scintillator detectors are composed of large volumes of hydrocarbons, which have the approximate chemical formulae C_nH_{2n} . The detector could detect neutrinos via elastic scattering on electrons and scattering on hydrogen and carbon nuclei. IBD is the dominant reaction for supernova neutrinos

Liquid scintillator detectors have high energy resolution, low energy threshold and are excellent for antineutrinos detection by IBD. This technology has been well developed for 50 years. However, it is much more expensive than water Cherenkov.

1.4.4 UHE neutrino detectors

With the purpose of investigating source candidates like AGNs and cosmogenic neutrinos, high-energy neutrino telescopes are undergoing a rapid development. Radio Cherenkov techniques making use of the Askaryan effect are successful for detecting UHE neutrinos. The Askaryan effect is based on the Cherenkov effect. It is the phenomenon that when neutral particles (e.g. neutrinos) passing through a dense dielectric medium induce a charge excess which emits a cone of coherent radiation. The Askaryan effect is applied for neutral particles, and therefore, UHE neutrinos could be tracked. More important, these neutrinos point towards the sources, so this effect can help us to find the origin of cosmic rays.

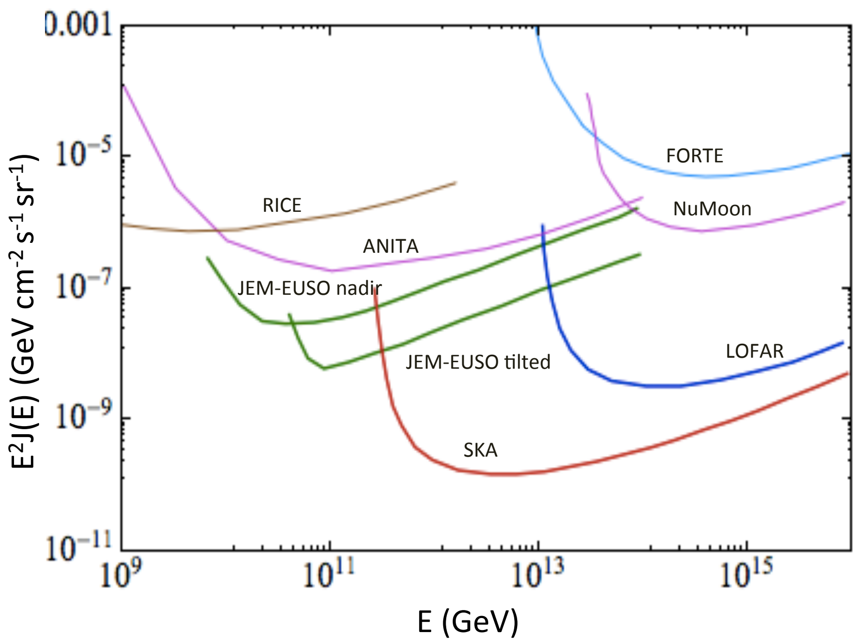

Figure 1.7: Existing upper bounds on the UHE neutrino flux from GLUE, NuMoon, FORTE, ANITA, RICE, and expected sensitivities at JEM-EUSO (nadir and tilted modes), LOFAR and SKA as labeled in the figure

Some projects use the moon as a target, searching for radio bursts, as with GLUE [32], NuMoon [33] and RESUN [34]. UHE neutrinos interact with baryons in the lunar regolith, resulting in a hadronic shower of particles with about 20% electrons excess. These electrons create a short duration pulse of radio Cherenkov radiation. The pulse is emitted in a Cherenkov cone of $\theta_c \sim 55^\circ$, and detected by radio telescopes [34].

The FORTE [35] satellite searches the Cherenkov radio bursts resulting from neutrino electromagnetic showers in the Greenland ice sheet. And RICE [36] and ANITA [37] use the polar cap in Antarctica as target medium. The space science mission JEM-EUSO [38] is planning to observe the fluorescent light emitted from extensive air showers with the Earth's atmosphere as a target [39].

The LOFAR [40] is a new radio telescope working at low frequencies, 10 – 200 MHz, using the Moon as target. It is a pathfinder of the SKA [41]. The SKA will operate in the GHz regime. Both of them are in planning stages. In Fig. 4.7, the upper bounds and sensitivities of these experiments are shown.

Chapter 2

Supernova rate and diffuse supernova neutrino flux

2.1 Star and supernova

2.1.1 Star's life

Stars are an important component of the universe. They are born in the high density region of a nebula, a cloud of dust and gas. Gravity causes dust and gas to contract and condense into a core. More atoms are attracted into the center, which is a process of accretion. The core is heated up due to atom collisions. The protostar is formed. With the higher density and temperature of the core, nuclear reactions ignite, fusing hydrogen into helium. These reactions release energy, and equilibrium is reached when the gas pressure balances with gravity. At this point, accretion stops, and we have a main sequence star.

The evolution of a star is determined by its initial mass and metallicity. Stars with small mass, M $< 1.5\ M_{\odot}$ (with $M_{\odot}$ solar mass), remain in main sequence for billions of years, however those with large mass, M $> 8\ M_{\odot}$, only a few million years. That is because larger stars have to fuse faster to keep equilibrium. As the proportion of helium increases, the star slowly increases its temperature and density. To maintain stability and equilibrium, when the temperature is high enough, helium begins fusing into carbon.

For massive stars, the temperature can increase further up to the point when carbon fusion begins. Continuing, neon, oxygen, silicon and then iron are produced. Shell burning keeps adding mass to the central core until the mass of core reaches the order of Chandrasekhar mass, the presupernova state. For most massive supernova progenitors, the result of the silicon-burning stage is the production of iron. The iron core is at the center of the canonical onion skin structure with progressively lighter elements from the inside out [43], as seen in Fig. 2.1.

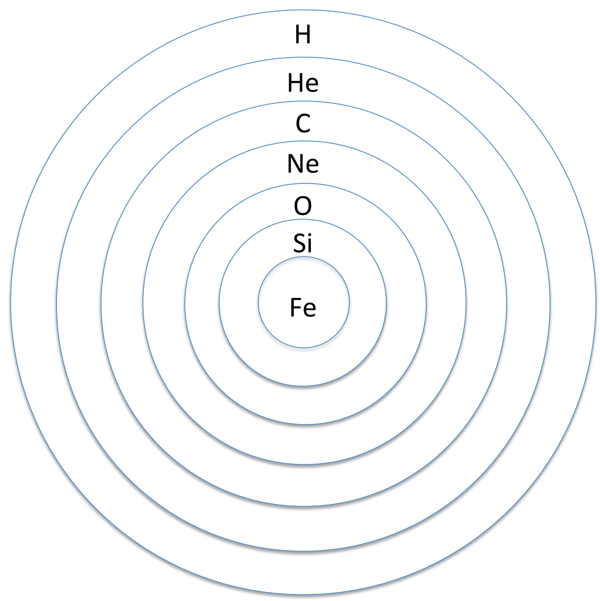

Figure 2.1: Onion layer structure core of a massive star.

Up until the last burning stage, the mass of the star is supported against gravity by the released energy from fusion of lighter elements to heavier ones. However, since iron is the most stable element with the highest binding energy, it does not undergo fusion. The core has to absorb energy to fuse into a heavier element. Therefore, there is not sufficient energy to support the gravity, and the core contraction quickly turns into collapse. This process lasts less than 1 second, and increases the temperature and density of the core. A shockwave is formed and causes an explosion, which is known as supernova. The core can be compressed into a neutron star. For extremely massive stars (M $\geq$ 25 $M_{\odot}$), the core can directly form a black hole.

A supernova (SN) marks the end of the stellar evolution process of a massive star as an explosion, ejecting the thermonuclear burning products into the interstellar medium. The synthesis of heavy elements in supernovae is a candidate mechanism which could explain the abundances of heavy elements. On the basis of the light curves

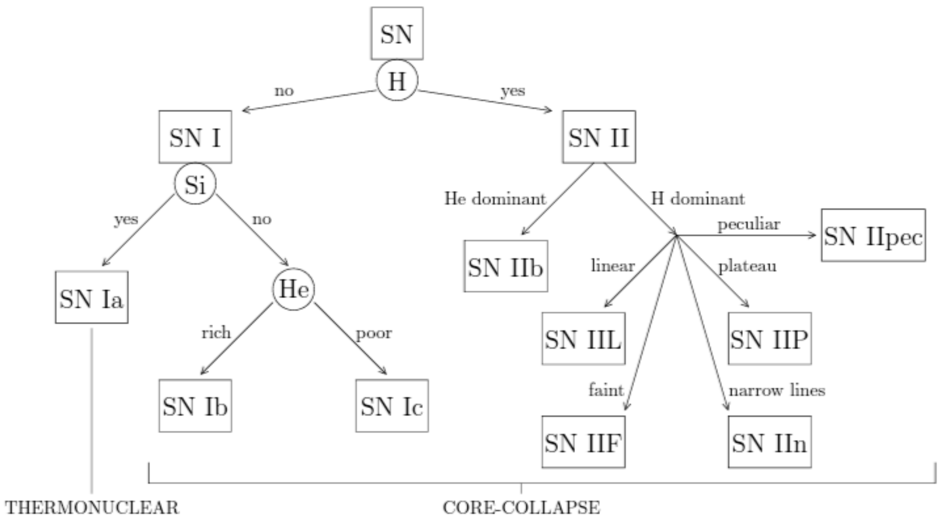

Figure 2.2: Supernova classification from Figure 15.1 of [42].

and features of spectral lines, supernovae are classified into two wide categories, type I and type II. Generally speaking, these two types are characterized by the absence or presence of hydrogen lines in the light spectrum. Type I are distinguished into different subgroups by the presence or absence of Si absorption lines, which are Ia, and Ib/c, as seen in Fig. 2.2 [42]. Type Ia are observed in all galaxies, whereas Type Ib and Type Ic have been seen only in spiral galaxies near sites of recent star formation (HII regions). Type II are mainly observed in spiral galaxies, spiral arms and HII regions, and are typically absent in regular galaxies (elliptical galaxies).

Type Ib/c and II are generated from the core collapse of massive stars. Type Ia supernovae, also called thermonuclear supernovae, are produced from the explosion of white dwarfs. From the point of view of the mechanism that generates the supernova, type Ib/c are more similar to II. They are more interesting than Type Ia to us, because they emit most of their energy as neutrinos and leave neutron stars and black holes as remnants.

Type II supernovae are distinguished by the details of spectra and light curve shape, including IIL, IIP, IIn, IIF, etc. In light curves, we see type IIP have a plateau light phase, and IIL just decay after the maximum to reach a linear luminosity decline. SN1987A was a case of type IIP. For more detailed information, see Chapter 3.

2.1.2 Physics of core collapse

As the core contracts, electrons get absorbed by protons to produce neutrons and electron neutrinos, carrying large amounts of energy. Electron capture accelerates the collapse and results in the reduction of Y_e, the electron number per nucleon. The pressure support is also reduced by photodissociation of heavy nuclei,

$$\gamma + ^{56}_{26}Fe \rightleftharpoons 13\alpha + 4n \tag{2.1}$$

The neutrino opacity is dominated by coherent neutrino-nucleus scattering, $\nu + (A,Z) \rightarrow \nu + (A,Z)$, which is a neutral current weak interaction. Coherent scattering means that, if a neutrino has small enough momentum (up to $\sim$ 50 MeV), and collides with a nucleus, this nucleus will recoil as a whole [44]:

The mean free paths for this interaction can be expressed as

$$\lambda \approx \frac{1}{n\sigma_\nu} \approx 10^7 cm \left(\frac{10^{12} gcm^{-3}}{\rho}\right) \frac{A}{N^2} \left(\frac{10MeV}{\varepsilon_\nu^2}\right) \tag{2.2}$$

where n is the number density of nuclei, σ is the cross section of scattering, ρ is the matter density, ε_ν is the neutrino energy, A is the number of nucleons and N is the number of neutrons. When the diffusion time of neutrinos (R^2/λ, R is the radius of the core), $\sim$ 10s, is much longer than freefall collapse time, which is less than 1 second, neutrinos are dynamically trapped in the collapsing core. As a result, deleptonization stops and the lepton number is preserved. Despite the neutrino trapping, the collapse is still occurring and density keeps increasing.

Once the density of the core exceeds nuclear matter density, the inner core rebounds into the still infalling outer core, creating shock waves which eject the stellar envelope. The shock quickly loses energy due to the dissociation of infalling heavy nuclei into free nucleons. Neutrinos stream away behind the shock [45]. If the weakened shock is able to expel the star, supernova explosion would be generated, on the time scale of $\sim$ 100 ms. Later, collapse will stop and form a neutron core. This neutron star has a 10 – 20 km radius, with a density comparable to nuclear matter density of $10^{14} g/cm^3$, and contains 90 percent neutrons and 10 percent protons. The progenitors with mass of 25 – 40 $M_\odot$ and lower metallicity could initially collapse to a neutron star. Later, due to the too much fallback of envelope onto the neutron star, the pressure of degenerate nucleons is not sufficient to maintain the stability, and a black hole is formed. Summary, the outcome and mechanism of a collapse various depending on the core profiles, rotation and metallicity.

However, numerical simulations find that, for star whose mass is between 8 – 25 $M_\odot$, the shock loses energy severely and stalls about 100ms after the bounce. The shock does not have sufficient energy to reach the outer layers of the stars. The infalling material passes the shock and accretes on the core. The supernova explosion can be achieved only if the shock is revived by some mechanism that is able to renew its energy. It is thought that the energy deposition by the huge neutrino flux produced thermally in the proto-neutron star [47] can revive the shock.

2.1.3 The supernova rate

The cosmic supernova rate (SNR) can be obtained directly from observational measurements or by the measurements of star formation rate (SFR). Since the SFR represents the birth rate of stars, while SNR presents the death rate of massive stars, and the massive stars that could generate core-collapse supernovae have short life time $\sim 30(M/8M_{\odot})^{-2.5}\ 10^6$ yrs, it is expected that the SNR should follow the same evolutionary trends in redshift as the cosmic SFR. The direct SNR measurements are discussed in the section below. I will discuss the SFR analysis first.

The stellar mass distribution in a newly formed population is given by the Initial Mass Function (IMF), an empirical function. The IMF is well described by a power-law form, which was first suggested by Salpeter in 1955 [46], $\xi(m) \propto m^{-2.35}$.

Here, $\xi(m)dm$ represents the number of stars with mass between m and $m+dm$. Considering that the canonical mass limits for core collapse supernovae are from $8M_{\odot}$ to $50M_{\odot}$. Then the relation of SNR and SFR can be presented as:

$$R_{SN}(z) = \frac{\int_{8M_{\odot}}^{50M_{\odot}} dm\xi(m)}{\int_{0}^{125M_{\odot}} dmm\xi(m)} R_{SF}(z) \simeq 10^{-2} M_{\odot}^{-1} R_{SF}(z) \tag{2.3}$$

The limits of integration in the denominator part are 0 – 125 $M_{\odot}$, and are supposed to include the main sequence stars. Extracting the SNR from the SFR, with Eq. 2.3 has some benefits. SFR measurements can get up to higher redshift, $z \sim 7$, which is really difficult to reach for supernova observation. Secondly, the SFR tells us the birth story of stars. Even if their deaths are not optically luminous, they are included in Eq. 2.3. Instead, the SNR only includes luminous core collapse supernovae. However, the SFR method has some uncertainties: the lower and upper mass limits of core collapse are not confirmed, and especially the lower cuts affect the fraction of core collapse supernovae strongly. Moreover, the relation of SNR and SFR could be redshift dependent.

As of today, the SFR has been well measured as seen in Fig. 2.3 (Fig. 1 in [48]). There are two methods to fit the data [48], one is piecewise and another is continuous as,

$$R_{SF}(z) \propto \begin{cases} (1+z)^{\beta} & z<1 \\ (1+z)^{\alpha} & 1<z<4.5 \\ (1+z)^{\gamma} & 4.5<z \end{cases} \tag{2.4}$$

$$R_{SF}(z) \propto \frac{a+bz}{1+(z/c)^{d}} \tag{2.5}$$

where α, β, γ, a, b, c, d are fit parameters. In [48], the best fitting values for these parameters are shown as a=0.0170, b=0.13, c=3.3, d=5.3, $\alpha=-0.26$, $\beta=-3.28$, $\gamma=-7.8$.

In our study, we consider SNR measurements, because we have ten data, and it is more direct. We apply the piecewise function, Eq. 2.4, to the SNR for its transparency [31]. We take $\alpha=-0.26$ and $\gamma=-7.8$ [48] and take β and R(0) (the SNR today) are fit parameters. We obtain the SNR function as:

$$SNR(z) = R(0) \begin{cases} (1+z)^{\beta} & z<1 \\ 2^{\beta+0.26}(1+z)^{-0.26} & 1<z<4.5 \\ 2.23\times 10^{5}\times 2^{\beta}(1+z)^{-7.8} & 4.5<z \end{cases} \tag{2.6}$$

The R(0) favored by the SFR is $1.33\times 10^{-4} h_{70}^{3} 10^{-4}/yr/Mpc^{3}$, and is a factor of 2 higher than the direct SNR measurements. As discussed in [49], this is most likely due to missing many dim or dark supernovae, because the SNR measurements are only sensitive to optically luminous core-collapse supernovae.

2.2 Supernova neutrinos

2.2.1 Neutrino emission from supernovae

A core collapse supernova emits 99% of its gravitational binding energy as neutrinos. There are basically two processes during a core collapse that contribute to the observ-

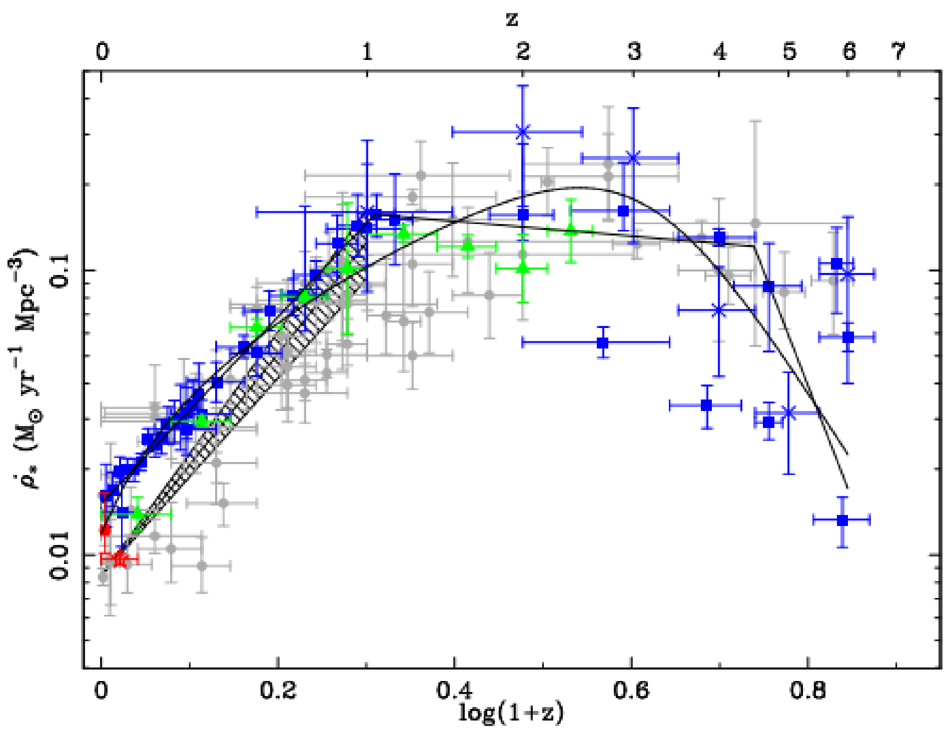

Figure 2.3: Evolution of SFR density with redshift. All the data are shown as grey points, green triangles, open red star, filled red circles, blue squares, and blue crosses. The two solid lines are the best fitting parametric forms.

able neutrino flux. The first one occurs when the outgoing shock passes the neutrino sphere during a few ms, resulting in the emission of electron neutrinos by electron capture process. This is usually called a deleptonization neutrino burst, which lasts for about hundred ms. The second one is from the Kelvin-Helmholtz cooling phase of proto-neutron star with an emission of neutrinos of all flavors. These neutrinos originate from reactions such as $e^+e^- \to \nu_l\bar{\nu}_l$, $n+p \to n+p+\nu_l+\bar{\nu}_l$. The medium is composed of protons, neutrons and electrons, and the neutrinos don't have enough energy to create muons and tauons. Electron neutrinos and anti-neutrinos interact with matter via charged current and neutral current processes. However, the other flavor of neutrinos (ν_μ, ν_τ) only have neutral current interactions. Therefore they decouple from matter in the deeper and higher density region of the star, and for this reason they have higher temperatures. Moreover, ν_es interact with neutrons with a shorter mean free path than $\bar{\nu}_e$s with protons, due to the overabundance of neutrons compare to protons. Hence ν_es have lower decoupling temperatures. Then the hierarchy of average energy becomes $\langle E_e\rangle < \langle E_{\bar{e}}\rangle < \langle E_x\rangle$, hereafter x indicates μ, τ flavor neutrino [51]. Long-term cooling calculations find perfect equipartition of the luminosities between the six neutrino species [50].

Several groups have performed simulations of the neutrino spectrum from supernovae, i.e. the Lawrence Livermore group (1998) [52], Burrows, Thompson and Pinto (2003) [53], Keil, Raffelt and Janka (2003) [54] and Oak Ridge-Basel Group [50]. We adopt the neutrino spectrum of each species w obtained by the Monte Carlo simulation given by Keil, Raffelt and Janka (2003):

$$F_w^0 = \frac{dN_w}{dE} \simeq \frac{(1+\alpha_w)^{1+\alpha_w} L_w}{\Gamma(1+\alpha_w) {E_{0w}}^2} \left(\frac{E}{E_{0w}}\right)^{\alpha_w} e^{-(1+\alpha_w)E/E_{0w}}, \tag{2.7}$$

where L_w is the luminosity, E_{0w} is average energy, and Γ is the Gamma function. The numerical parameter α_w describe the shape of spectrum. Typical values for these parameters are $\alpha_x = 2.5$, $\alpha_x = 3.5$, average energy $E_{0x} = 15MeV$, $E_{0\bar{e}} = 18MeV$, luminosity $L_{\bar{e}} \sim L_x \sim 5 \cdot 10^{52} ergs$.

2.2.2 Oscillation of supernova neutrinos

Neutrino oscillations have been verified by solar and atmospheric neutrino observation and long baseline experiments. Supernova neutrinos undergo flavor conversions near the SN core, in the SN envelope, on the way to the earth and through the earth. In supernovae, neutrinos not only interact with the medium through which they propagate (MSW effect [55, 56]), but also with each other due to the high density of neutrino gas [57]. Overall, conversion depends on the mass square difference $\Delta m_{ij}^2 = m_i^2 - m_j^2$, all three mixing angles (θ_{12}, θ_{23}, θ_{13}), the neutrino energy, and the medium density and composition of propagation. θ_{12} and θ_{23} are well known [12] and recently θ_{13} has been well measured by Daya Bay [6], Reno [7] and T2K [9]. Studying supernova neutrino oscillation gives us a chance to reveal the neutrino mass hierarchy.

The Hamiltonian 3×3 matrix of the system can be expressed as,

$$H = H_0 + H_m + H_{\nu\nu} \tag{2.8}$$

Here H_0 is the Hamiltonian in vacuum, that can be written as,

$$H_0 = \frac{\Delta m_{13}^2}{2E}\begin{pmatrix} s_{13}^2 & 0 & c_{13}s_{13} \\ 0 & 0 & 0 \\ c_{13}s_{13} & 0 & c_{13}^2 \end{pmatrix} + \frac{\Delta m_{12}^2}{2E}\begin{pmatrix} c_{13}^2 s_{12}^2 & c_{12}c_{13}s_{12} & -c_{13}s_{12}^2 s_{13} \\ c_{12}c_{13}s_{12} & C_{12}^2 & -c_{12}s_{12}s_{13} \\ -c_{13}s_{12}^2 s_{13} & -c_{12}s_{12}s_{13} & s_{12}^2 s_{13}^2 \end{pmatrix} \tag{2.9}$$

The other two terms are the matter term H_m, and the neutrino-neutrino term $H_{\nu\nu}$. I will discuss them in detail below.

2.2.2.1 Collective neutrino oscillation

Early studies of supernova neutrino oscillations focused on MSW-like effects [58], assuming the effect of neutrino-neutrino interactions was small. However, it was found that coherent scattering of neutrinos with other neutrinos could have a significant effect [59] to the MSW. During the accretion phase, the neutrino-neutrino collective effects cause non-linear neutrino flavor conversions, long before the MSW flavor conversions start.

To investigate the collective neutrino oscillations, single-angle and multi-angle schemes are commonly used [57]. Both apply the neutrino bulb model, where the supernova environment is spherical symmetric around the center of the proto-neutron star. A multi-angle neutrino-neutrino interaction scheme assumes axial symmetry, but not complete spherically symmetric. On the other hand a single-angle scheme supposes the neutrino evolution is simply spherically symmetric.

The Hamiltonian of the ν-ν oscillation with the multi-angle dependence as studied in [60, 61] is

$$H_{\nu\nu} = \sqrt{2}G_F \int d\mathbf{p}'(1-\hat{\mathbf{p}}\cdot\hat{\mathbf{p}}')(\rho_{p'}-\bar{\rho}_{p'}) \tag{2.10}$$

where G_F is the Fermi constant, $\hat{\mathbf{p}}$ and $\hat{\mathbf{p}'}$ are the unit vector of the propagation direction of the colliding neutrinos. The density matrices for neutrinos and antineutrinos are $\rho_{p'}$ and $\bar{\rho}_{p'}$ respectively, whose diagonal elements are neutrino densities, $\rho_{p'} = diag(n_{\nu_e}, n_{\nu_\mu}, n_{\nu_\tau})$, $\bar{\rho}_{p'} = diag(n_{\bar{\nu}_e}, n_{\bar{\nu}_\mu}, n_{\bar{\nu}_\tau})$, and off-diagonal elements encode phase information due to flavor oscillations.

In a supernova, ν_μ, ν_τ and their antiparticles are produced at identical rates. Following the standard terminology, we define the non-electron flavor states as $\nu_{x,y} = cos\theta_{23}\nu_\mu \mp sin\theta_{23}\nu_\tau$ [62], here $\theta_{23} \simeq \frac{\pi}{4}$ is the atmospheric mixing angle. Since the initial ν_x and ν_y fluxes are identical, the primary neutrino fluxes can be expressed in terms of ν_e, $\bar{\nu}_e$ and ν_x.

The multi-angle neutrino-neutrino interactions between ν_e and ν_y are driven by the atmospheric mass difference $\Delta m^2_{atm} = 2.35\times10^{-3}eV^2$ [63] and the mixing angle θ_{13}, where $sin^2\theta_{13} = 0.02$ [6]; while $\nu_e \leftrightarrow \nu_y$ oscillation is driven by Δm^2_{sol}. The third state, ν_x contributes to the collective effects negligibly as studied in [64]. However, it undergoes MSW effects at later time. The neutrino fluxes after collective oscillation can be expressed as:

$$F^c_{\nu_e} = P_c F^0_{\nu_e} + (1-P_c)F^0_{\nu_y} \tag{2.11}$$

$$F^c_{\bar{\nu}_e} = \bar{P}_c F^0_{\bar{\nu}_e} + (1-\bar{P}_c)F^0_{\bar{\nu}_y} \tag{2.12}$$

where P_c and $\bar{P}_c$ are the survival probabilities of ν_e and $\bar{\nu}_e$ after self-induced flavor conversions, strongly depending on the mass hierarchy and neutrino flux density. The neutrino spectral swap (flavor exchange) $\nu_e \leftrightarrow \nu_x$, occurs as discussed in [65] in various conditions. Poring the cooling phase, multiple spectral splits could occur [66].

After the primary fluxes $F^0_{\nu_e}$ undergo the neutrino-neutrino interaction, they will have traditional MSW effects at larger radii. In the medium, the potential difference of ν_e and ν_x due to the charged current scattering of ν_e on electrons [67] is

$$V = \sqrt{2} G_F N_e, \tag{2.13}$$

where N_e is the number density of electrons.

The corresponding eigenstates and eigenvalues of the Hamiltonian depend on V. The neutrino evolution equation is

$$i\frac{d}{dt}\begin{pmatrix} \nu_e \\ \\ \nu_x \end{pmatrix} = \begin{pmatrix} -\frac{\Delta m^2}{4E}cos2\theta + V & \frac{\Delta m^2}{4E}sin2\theta \\ \\ \frac{\Delta m^2}{4E}sin2\theta & \frac{\Delta m^2}{4E}cos2\theta \end{pmatrix}\begin{pmatrix} \nu_e \\ \\ \nu_x \end{pmatrix} \tag{2.14}$$

So the mixing angle in matter θ_m is expressed as

$$sin^2 2\theta_m = \frac{sin^2 2\theta \cdot \left(\frac{\Delta m^2}{2E}\right)^2}{\left[\frac{\Delta m^2}{2E}cos2\theta - \sqrt{2}G_F N_e\right]^2 + \left(\frac{\Delta m^2}{2E}\right)^2 sin2\theta} \tag{2.15}$$

Therefore, we can see that the resonance occurs when $sin^2 2\theta_m = 1$ (i.e. at maximal mixing),

$$\sqrt{2}G_F N_e = \frac{\Delta m^2}{2E}cos2\theta \tag{2.16}$$

In the resonance layer, the density is

$$\rho_{res} \approx \frac{\Delta m^2 m_N}{2\sqrt{2}G_F E Y_e}cos2\theta \approx 1.4\times 10^6 gcm^{-3}\frac{\Delta m^2}{1eV^2}\frac{10MeV}{E}\frac{0.5}{Y_e}cos2\theta \tag{2.17}$$

where m_N is the mass of the nucleon, θ is the mixing angle and E is the neutrino energy. There are two resonance (level crossing) layers, associated with (Δm^2_{atm}, θ_{13}), and (Δm^2_{sol}, θ_{12}), respectively [68].

For $\Delta m^2_{atm} \sim 2.3\times 10^{-3} eV^2$, the required density is about 10^3 to $10^4 g\cdot cm^{-3}$. This is known as the H-resonance layer (higher density). For $\Delta m^2_{sol} \sim 7.6\times 10^{-5} eV^2$,

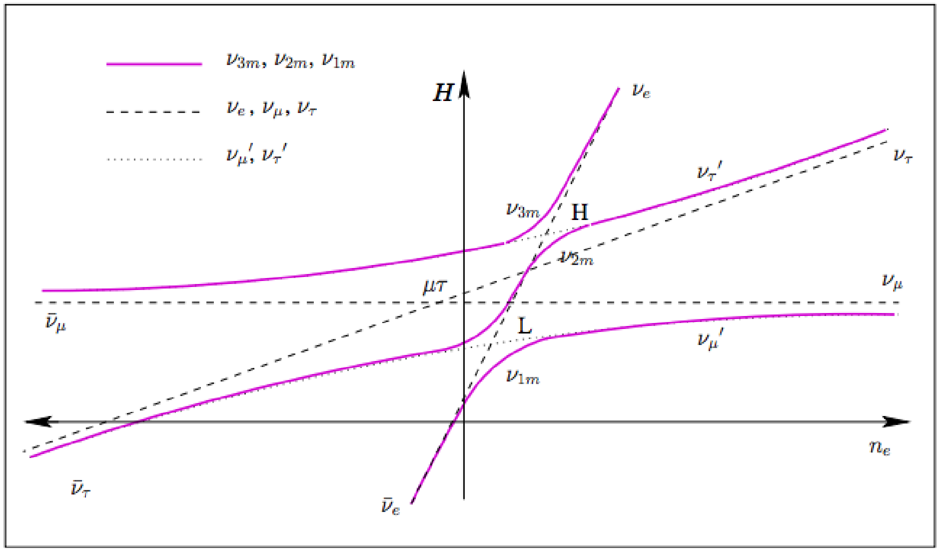

Figure 2.4: Level crossing scheme in supernova versus electron number density n_e for normal hierarchy from Fig. 1 of [69]. The semi-plane with negative density describes the conversion of antineutrinos.

the density is about 10 $g \times cm^{-3}$, called the L-resonance layer (lower density). These two layers are both in the outer supernova envelope, far outside the core of the star.

If the mass hierarchy is normal (inverted), the H-resonance occurs in the neutrino (anti-neutrino) channel, instead, the L-resonance always occurs in the neutrino channel as seen in Fig. 2.4 and 2.5. One may calculate the transition probability P_H – the probability that a neutrino jumps between the matter eigenstates of the Hamiltonian by using the Landau-Zenner-Stuckelberg formula and the profile,

$$P_H = exp\Big[- \big(\frac{E_r}{E}\big)^{2/3}\Big] \tag{2.18}$$

$$E_r = 1.08 \cdot 10^7 MeV \big(\frac{|\Delta m^2_{32}|}{10^{-3} eV^2}\big) C^{1/2} sin^3\theta_{13} \tag{2.19}$$

where C=1 – 15 as described in [70]. The adiabaticity parameter γ determines the dynamics of conversion,

$$\gamma \equiv \frac{\Delta m^2}{2E_\nu} \frac{sin^2 2\theta}{cos 2\theta} \frac{n_e}{|dn_e/dr|} \tag{2.20}$$

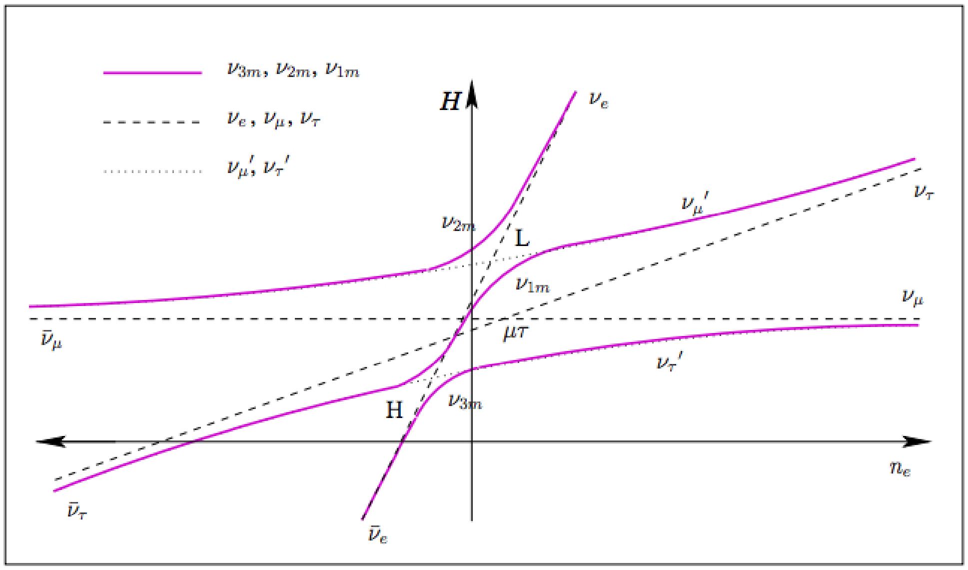

Figure 2.5: Level crossing scheme in supernova vs electron number density n_e for inverted hierarchy from Fig. 2 of [69]. The semi-plane with negative density describes the conversion of antineutrinos.

where n_e is the electron number density, θ is the mixing angle [71]. When $\gamma \gg 1$, corresponding to small jump probability, adiabatic conversion occurs, where strong flavor exchanged is realized. When $\gamma \ll 1$, the resonance is called nonadiabatic, and no conversion occurs. The flavor conversions in these two resonances are independent, and the total survival probability is the product of the survival probabilities in these two separate layers. Therefore the survival probability for the MSW effects only, can be calculated for normal hierarchy:

$$P_M \simeq P_H sin^2\theta_{12} + [1 - P_H(1 + sin^2\theta_{12})]sin^2\theta_{13} \tag{2.21}$$

$$\bar{P}_M \simeq cos^2\theta_{12}(1 - sin^2\theta_{13}) \tag{2.22}$$

For inverted hierarchy:

$$P_M \simeq sin^2\theta_{12}(1 - sin^2\theta_{13}) \tag{2.23}$$

$$\bar{P}_M \simeq P_H cos^2\theta_{12} + [1 - P_H(1 + cos^2\theta_{12})]sin^2\theta_{13} \tag{2.24}$$

Therefore, the emerging neutrino fluxes from SN after collective oscillation and MSW effect can be expressed as

$$F_{\nu_e} = P_M F^c_{\nu_e} + (1 - P_M) F_{\nu_x} \tag{2.25}$$

$$F_{\bar{\nu}_e} = \bar{p}_M F^c_{\bar{\nu}_e} + (1 - \bar{p}_M) F^c_{\bar{\nu}_x} \tag{2.26}$$

After neutrinos escape from the SN, we suppose they travel through vacuum before arriving at the detector. Then for normal hierarchy the detected fluxes are:

$$F_{\nu_e} = sin^2\theta_{12}(F^0_{\nu_e} - F^0_{\nu_x})[\bar{P}_c(2P_H - 1) + 1 - P_H] + F^0_{\nu_x} \tag{2.27}$$

$$F_{\bar{\nu}_e} = cos^2\theta_{12}\bar{P}_c(F^0_{\bar{\nu}_e} - F^0_{\bar{\nu}_x}) + F^0_{\bar{\nu}_x} \tag{2.28}$$

For inverted hierarchy:

$$F_{\nu_e} = sin^2\theta_{12}P_c(F^0_{\nu_e} - F^0_{\nu_x}) + F^0_{\nu_x} \tag{2.29}$$

$$F_{\bar{\nu}_e} = cos^2\theta_{12}(F^0_{\bar{\nu}_e} - F^0_{\bar{\nu}_x})[\bar{P}_c(2P_H - 1) + 1 - P_H] + F^0_{\bar{\nu}_x} \tag{2.30}$$

Therefore, we can get the total survival probability of $\bar{\nu}_e$ after leaving the star $\bar{P}_{nh} = cos^2\theta_{12}\bar{P}_c$ for NH and $\bar{P}_{ih} = cos^2\theta_{12}[\bar{P}_c(2P_H - 1) + 1 - P_H]$ for IH. If the hierarchy is inverted, the time-averaged survival probability is ~ 0 for the measured value of θ_{13} and then the final detected $\bar{\nu}_e$ flux is only the original ν_x flux [68].

After the neutrinos exit the SN, they arrive at the Earth as mass eigenstates. The conversion probabilities through the Earth $P_{i.e.}$ is given by [68]. In our calculation, we neglect the earth effects compare to other effects. For simplicity, we take the $\bar{\nu}_e$ survival probability $\bar{P}$ as 0 and 0.68 for normal and inverted hierarchies.

2.2.3 SN1987A

Following [73], we do an SN1987A data analysis, including twelve data points from from Kamiokande II and eight from IMB. All of these neutrinos were detected by the inverse beta decay, where the emitted positron was measured by its Cherenkov light. Taking into account of the flavor conversion of neutrinos, we use the set of five parameters, $L_{\bar{e}}, L_x, E_{0\bar{e}}, E_x, \bar{P}$.

Due to the sparse number of events in the detector, the maximum likelihood method is adopted following [74, 75]. The energy range of detected events is divided into a few bins. The expected number of events in each energy bin can be expressed as n_i, depending on $L_{\bar{e}}, L_x, E_{0\bar{e}}, E_x, \bar{P}$. The actual events number in this bin is N_i. The probability for an outcome with N_i events in i-th bin is P_i,

$$P_i = \frac{n_i^{N_i}}{N_i!} e^{-n_i} \tag{2.31}$$

The likelihood function is expressed as (see Appendix A),

$$\mathscr{L} = \prod_{i=1}^{N_{bin}} P_i, \tag{2.32}$$

where N_{bin} is the number of bins. The expected number of detected events in i-th bin is given by,

$$n_i = \int_{E_i-\Delta E}^{E_i+\Delta E} \frac{N_p}{4\pi D^2} \sigma(E+\Delta M) F_{\bar{\nu}_e}(E+\Delta M) dE \tag{2.33}$$

$$\sigma = \sigma_0 \Big(\frac{E}{m_e}\Big)\Big(1-\frac{\Delta M}{E}\Big)\Big[1-\frac{2\Delta M}{E}+\frac{\Delta M^2-m_e^2}{E^2}\Big]^{1/2} \tag{2.34}$$

where the interval of integration $[E_i-\Delta E, E_i+\Delta E]$ corresponds to the energy bin, D is the distance from SN1987A to the Earth, ΔM is the neutron proton mass difference which is 1.29 MeV, σ is the cross section of inverse beta decay, m_e is the electron mass and $F_{\bar{\nu}_e}(E+\Delta M)$ is the electron antineutrino flux at the detector. Here the energy resolution function is not included in the calculation, due to the method of dividing the energy bins with consideration of energy uncertainties ε. The size of each energy bin is $\sim 2\varepsilon$.

Applying the calculation to Kamiokande II and IMB data separately, we could get $\mathscr{L}_{K2}$, $\mathscr{L}_{IMB}$. The total χ^2 is,

$$\chi^2_{87} = -2ln\big(\mathscr{L}_{K2} \cdot \mathscr{L}_{IMB}\big) \tag{2.35}$$

We perform the maximum likelihood analysis, finding the minimum value of this quantity, $\chi^2_{87,min}$ and scan this five parameter space, with the condition,

$$\chi^2(L_{\bar{e}}, L_x, E_{0\bar{e}}, E_x, \bar{P}) - \chi^2_{87,min} \leq \chi(k), \tag{2.36}$$

where k is the number of parameters, here k=5. Find the allowed region at 68.3%, 90%, 99% confidence level, with $\chi(5) = 5.86, 9.24, 15.09$ respectively (see Appendix A).

The best fit value of χ^2 is 84.2, with corresponding parameters ($L_{\bar{e}}$, L_x, $E_{0\bar{e}}$, E_x, $\bar{P}$)= ($4.0 \cdot 10^{43}$ ergs, $0.8 \cdot 10^{43}$ ergs, 4.2 MeV, 14.9 MeV, 0.68). In the allowed parameter space, we do projections on the E_x - $E_{0\bar{e}}$ plane. As discussed before, $E_{0x} > E_{0\bar{e}}$, see Fig. 2.6. The regions of $E_{0x} < 8MeV$ and $E_{0\bar{e}} < 5MeV$ are excluded, and $E_{0\bar{e}}$ is no more than 16 MeV. For IH, there are only x flavor neutrinos contributing to the neutrino flux. We find the contour plot for L_x and E_{0x} as in Fig. 2.7. The allowed E_{0x} is between 9 – 15MeV and L_x is 0.2 – 1.3 $\times 10^{53}$ ergs.

2.3 Supernova rate analysis

2.3.1 Direct SNR measurements

In recent years, direct measurements of cosmic core collapse supernovae have been rapidly improved. In total, we have ten direct measurements with statistic and systematic errors at different redshift. These data cover redshift from 0 to 1.11. These data and references are listed in the table below.

Data point number 1 comes from Botticella et al, who use Southern inTermediate Redshift ESO Supernova Search (STRESS). In their work, the major systematic

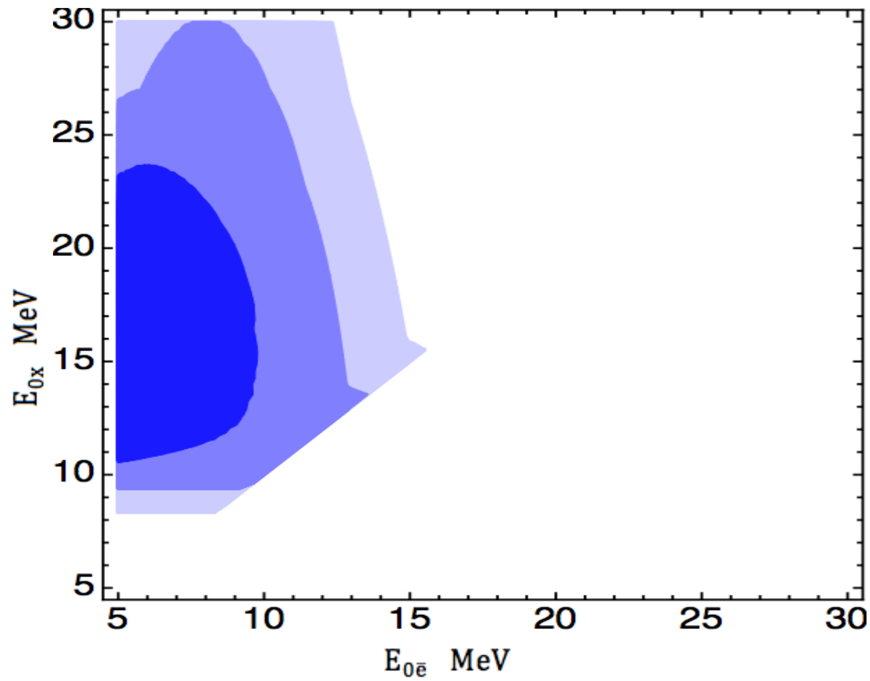

Figure 2.6: Projections of 68%, 90% and 99% confidence level regions (the darker, medium and light blue) allowed by SN1987A data on the $E_{0\bar{e}}$ - E_{0x} plane.

Table 2.1: The direct measurements of supernova rate at average redshift z.

Number	Average Redshift	$R_{SN}h_{70}^3 10^{-4}/yr/Mpc^3$	Reference
1	0.21	$1.15^{+0.43+0.42}_{-0.33-0.32}$	Botticella et al [76]
2	0.01	$0.43^{+0.17}_{-0.17}$	Cappellaro et al [77]
3	0	$0.62^{+0.07+0.17}_{-0.07-0.15}$	Li et al [78]
4	0.39	$3.29^{+3.08+1.98}_{-1.78-1.45}$	Melinder et al [79]
5	0.73	$6.40^{+5.3+3.65}_{-3.12-2.11}$	Melinder et al [79]
6	0.66	$6.9^{+2.552+9.59}_{-2.76-4.63}$	Graur et al [80]
7	0.3	$1.63^{+0.34+0.37}_{-0.34-0.28}$	Bazin et al [81]
8	0.39	$3.0^{+1.28+1.04}_{-0.94-0.57}$	Dahlen et al [82]
9	0.73	$7.39^{+1.86+3.20}_{-1.52-1.6}$	Dahlen et al [82]
10	1.11	$9.57^{+3.76+4.96}_{-2.8-2.8}$	Dahlen et al [82]

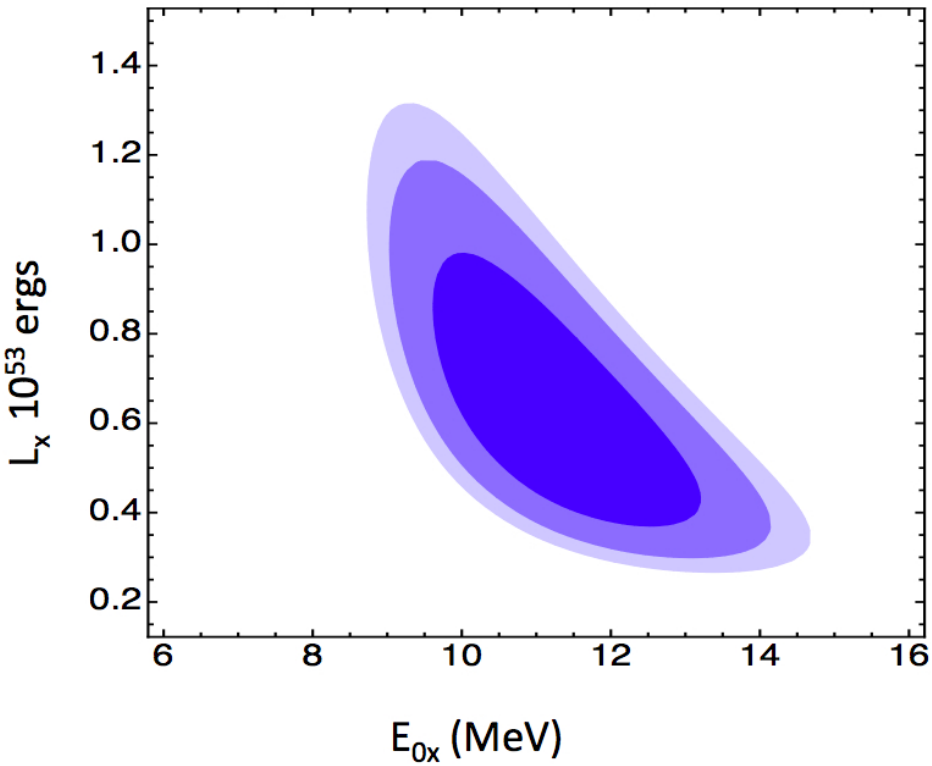

Figure 2.7: Projections of 68%, 90% and 99% confidence level regions (the darker, medium and light blue) allowed by SN1987A data on the E_{0x} - L_x plane.

uncertainty is due to the lack of a spectroscopic classification for a large fraction of the SN candidates. For the CC SN rate the estimate of the detection efficiency and the dust extinction correction are also important sources of uncertainty. For their SN sample, the statistical and systematic uncertainties are comparable. Due to the growing number of detected SNe, statistical uncertainty will decrease in the future. Therefore, systematic errors will soon dominate the overall uncertainty.

No.2 data is from Cappellaro et al., who use a sample of 137 supernovae in a reference sample of about 10^4 galaxies. The errors quoted are purely statistical. The most severe concern for systematic error is also the lack of spectroscopic classification for all candidates.

No.3 data is from Li et al, who use the Lick Observatory Supernova Search. They use Poisson statistics for statistical errors. For most of the rates the systematic errors are roughly the same size as the statistical errors. They emphasize that the final systematic errors are quite uncertain due to the rough estimates from several components.

No. 4 and 5 are from Melinder et al., who use the Stockholm VIMOS Supernova Survey. In their work, the statistical errors are calculated with chosen redshift bins, with a reasonable number of sources in each bin to obtain similar statistical errors. Because of the low number of SNe, the statistical errors are high. The systematic errors are from misclassification, redshift uncertainties, detection efficiencies, photometric errors, etc.. The summed systematic errors are roughly half of the statistical errors. The main contribution to the systematic errors comes from misclassification.

No. 6 data is from Graur et al, who use Subaru Deep Field. They use 1σ Poisson uncertainty as statistical errors. The systematic errors are mainly from misclassification, which is uncertain and greater than statistical errors.

No. 7 data is from Bazin et al, who use Supernova Legacy Survey. Their systematic errors come from type misidentification and redshift migration due to the use of photometric redshifts, which is an estimation of the distance of an object using photometry to determine the redshift. The statistical error comes from the limited number of redshift pairs they have used for the simulation. These two kinds of errors are comparable.

No. 8, 9 and 10 data are from Dahlen et al., who use Hubble Space Telescope. In their research, they investigate a number of possible sources for systematic errors, in which the main source is misclassification. The summed systematic errors are still smaller than the statistical.

Taking into account of the various uncertainties, in our work we have three parts of calculation: first with statistical errors only, the second with both statistical and systematic errors. The third has both statistical and systematic errors and also considers the correlation in the same experiments.

2.3.2 Data analysis

We apply a maximum likelihood analysis of these ten measurements (z_i, SNR_i), as given in Table 2.1, to find the best fit value of R(0) and β of Eq. 2.6. Suppose redshift z_i has negligible uncertainty. The expected value of SNR_i would be SNR(z_i). We could test how well SNR_i fit the function $SNR(z_i)$ by calculating χ^2. The analysis can be seen in detail in Appendix A.

(1). If we consider only the statistical errors, we take σ as the average of the absolute values of positive and negative uncertainty. With the formula above, We obtain the minimum value of $\chi^2_{min} = 3.51$, with best fit values of R(0)=0.58 $h^3_{70}10^{-4}/yr/Mpc^3$, $\beta = 4.34$. The contours in Fig. 2.8 refer to 68.3, 90, 95.4 % confidence levels, which are defined as $\chi^2 - \chi^2_{min}$=2.3, 4.61, 6.17.

(2). If we consider the both systematic and statistic errors, with quadratic addition of errors $\sigma = \sqrt{\sigma^2_{st} + \sigma^2_{sys}}$. We obtain the minimum value of $\chi^2_{min} = 1.60$, with best fit values of R(0)=0.52 $h^3_{70}10^{-4}/yr/Mpc^3$, $\beta = 4.54$, see Fig. 2.9.

(3). If the systematic errors are correlated between data points in the same experiment, like data No. 4, 5 from the Stockholm VIMOS Supernova Survey and No. 8, 9, 10 from the Hubble Space Telescope, then the correlations between data points should be taken into account. Then the χ^2 can be expressed as,

$$\chi^2 = \sum_i \sum_j [SNR_i - SNR(z_i)] V^{-1}_{ij} [SNR_j - SNR(z_j)] \tag{2.37}$$

where V_{ij} is the correlation matrix, which is $V_{ij} = \delta_{ij}\sigma^2_{i,stat} + \sum_\alpha \sigma_{i\alpha,sys}\sigma_{j\alpha,sys}$, the α here represents the systematic error source. Then I obtain the minimum value of $\chi^2_{min} =$

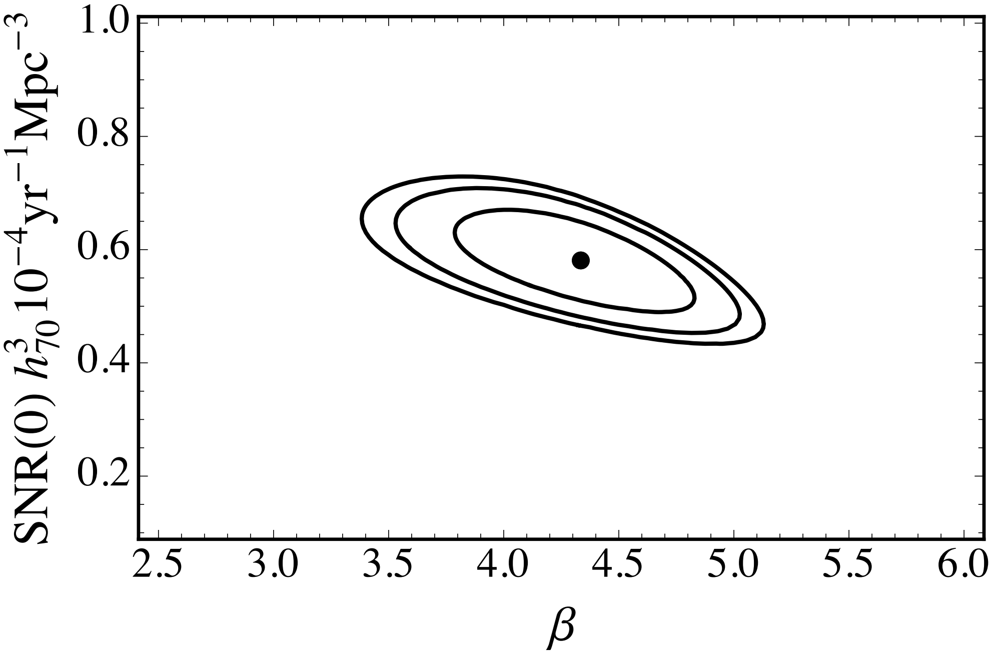

Figure 2.8: These contour plots give the allowed region of SNR(0) and β with statistic error only

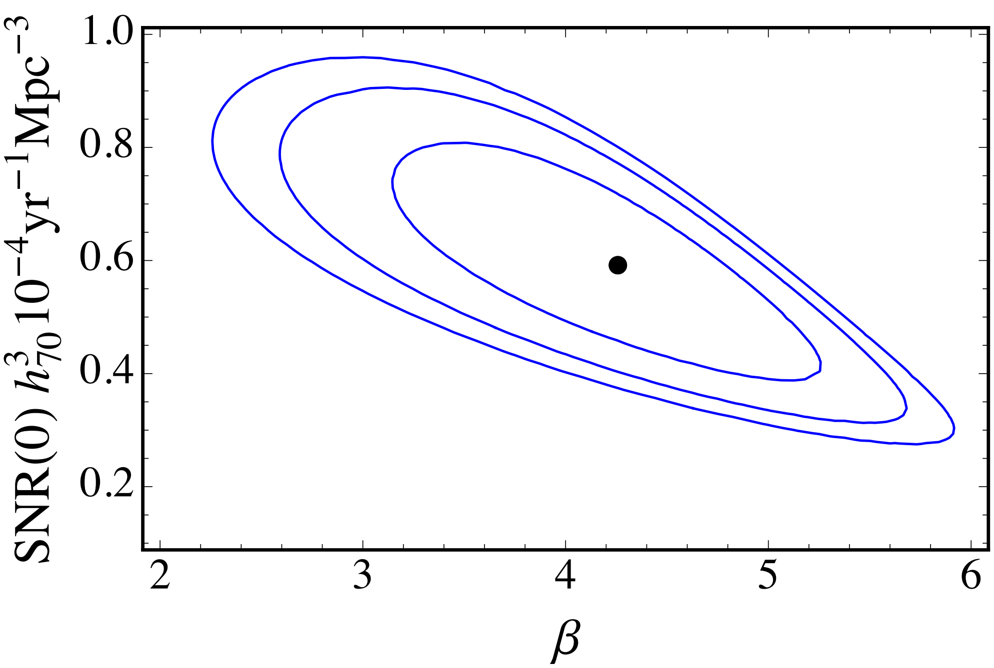

Figure 2.9: These contour plots give the allowed region of SNR(0) and β with statistic and systematic errors

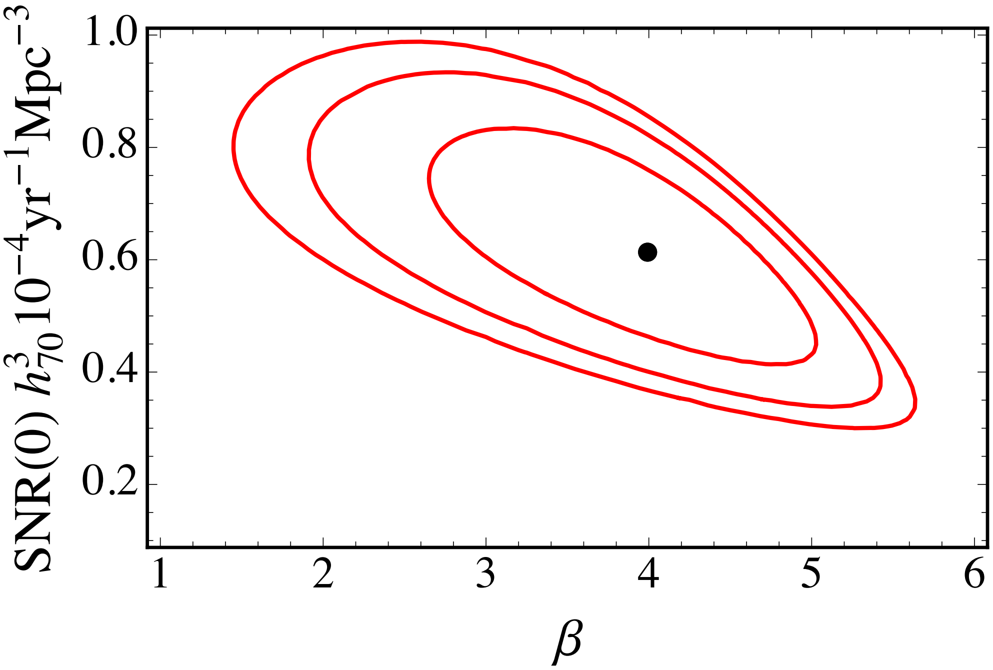

Figure 2.10: These contour plots give the allowed region of SNR(0) and β with correlated systematic errors.

2.10, with best fit values of R(0)=0.53 $h_{70}^3 10^{-4}/yr/Mpc^3$, $\beta = 4.30$, as seen in Fig. 2.10. For the statistic errors only case, the allowed region for 95.4% C.L. of SNR(0) is from 0.45 to 0.7 $h_{70}^3 10^{-4} yr^{-1} Mpc^{-3}$ and β is from 3.4 to 5.2. After getting best fit values of R(0) and β, plug them into the SNR function, I get a SNR as a function of redshift, see Fig. 2.11. All ten data points are shown in the figure with statistical errors. In Fig. 2.12, we can see the star formation rate-favored SNR(0), which is 1.33 $h_{70}^3 10^{-4}/yr/Mpc^3$ [49], about 2 times higher than what we get. That is been discussed in [49]. The discrepancy could be due to the faint supernova explosion, black hole forming collapse. It also shows the lower limit of supernova rate at z=0 by Smartt et al. [83], which is 0.96 $h_{70}^3 10^{-4}/yr/Mpc^3$. In their work, they used a 10.5 yr search with the volume of 28 Mpc and obtained a relative numbers of supernovae. The local supernova rate limit calculated is based on this search.

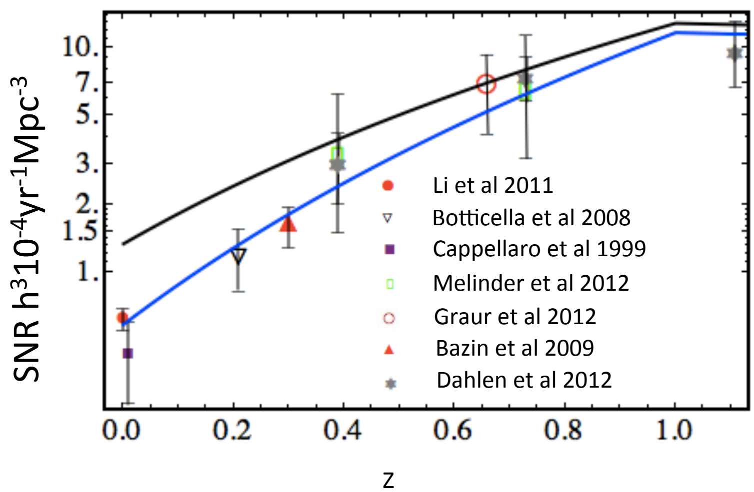

Figure 2.11: Supernova rate as a function of redshift, The black curve presents the star formation rate-favored SNR function, with (β, SNR(0)) = (3.28, 1.33), the blue curve is for the results with only statistical errors. All the marks are for data points with statistical errors in Table 2.1.

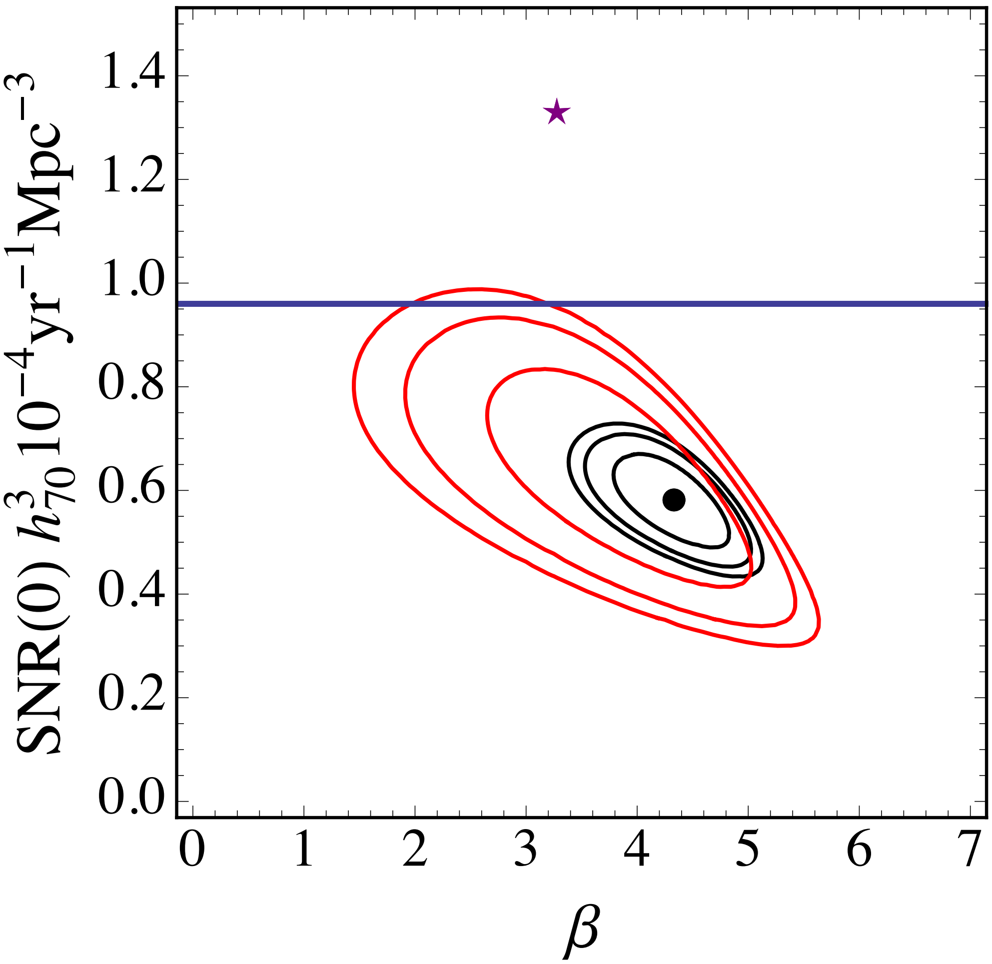

Figure 2.12: These contour plots give the allowed region of SNR(0) and β with statistic error only and with correlated systematic errors, and also provide a lower limit for SNR(0), which is 0.96. The star represents the star formation rate-favored (beta, SNR(0)), which is (3.28, 1.33)

The allowed region of (SNR(0), β) with statistic errors is smaller than that with correlated systematic errors. With large uncertainty, our allowed SNR(0) could meet the lower limit value of 0.96 $h_{70}^3 10^{-4}/yr/Mpc^3$ by [83]. The best fit value of SNR(0) is 2 times lower than the value predicted by the SFR. Our supernova rate fit provides a conservative estimation. This cause a lower DSNB prediction, compare to the other authors.

2.4 Diffuse Supernova neutrino flux

2.4.1 Expected flux

The detectors on Earth observe the diffuse neutrino flux from the whole sky, which is the sum of all the neutrino fluxes from every individual supernova, $\frac{dN_\alpha}{dE}$. After considering the supernova rate per comoving volume, and survival probability of flavor α due to neutrino oscillation, we can get the formula below:

$$\Phi(E) = \frac{c}{H_0}\int_0^{z_{max}} R_{SN}(z) \sum_{\alpha=e,\mu,\tau} \frac{dN(E)_\alpha}{dE} P_{\bar{\alpha}\bar{e}}(E,z) \frac{dz}{\sqrt{\Omega_m(1+z)^3+\Omega_\Lambda}} \tag{2.38}$$

where $\Omega_m = 0.3$ is the dark matter density, $\Omega_\Lambda = 0.7$ is the dark energy density, $H_0 = 70kms^{-1}Mpc^{-1}$ is the Hubble constant. From the equation above, we can see that the diffuse supernova neutrino flux depends on seven parameters, five from SN1987A neutrino spectrum, two from the supernova rate function. To obtain the total likelihood of SN1987A neutrino and supernova rate data, we combine the two χ^2, χ^2_{DSNB}=χ^2_{87} + χ^2_{SNR}. Using the same method as before, we find the minimum value of $\chi^2_{DSNB,min}$, with a set of best fit parameters and calculate the corresponding Φ.

We scan the seven parameter space, finding the allowed regions at 99% confidence level, and calculate the interval of flux for three energy thresholds, E $>$ 11.3, 17.3, 19.3 MeV. The 19.3 MeV is the applied threshold in the search of DSNB in SK in 2003 [86], 17.3 MeV corresponds to the new threshold in SK in 2012 [84], and 11.3 MeV corresponds to the SK detector with Gd addition [85]. Due to the large neutron capture cross section of gadolinium, this Gd addition may cause 90% efficiency of neutron capture and reduce both spallation events and invisible muons, thus increasing the accessible energies for a DSNB search [87]. As seen in Table 2.2, with lower energy threshold, the DSNB flux increases significantly. Most of the flux falls in the low energy region.

Table 2.2: The predicted flux of $\bar{\nu}_e$ in a detector above 11.3, 17.3, 19.3 MeV, in the interval of 99% C.L.

$\Phi/cm^{-2}s^{-1}$	E>19.3 MeV	E>17.3 MeV	E>11.3 MeV
$99\%C.L.$	0.07-0.37	0.11-0.55	0.52-2.37

In 2012, the Super-Kamiokande collaboration improves their analysis, and increases the flux upper limit to 2.0 $cm^{-2}s^{-1}$ for $E_\nu > 18$ MeV positron energy (19.3 MeV neutrino energy, the 1.3 MeV is due to the mass difference between proton and neutron), and 2.9 $cm^{-2}s^{-1}$ for $E_\nu >$16 MeV positron energy (17.3 MeV neutrino energy). These new published limits are five times higher than our calculation. This discrepancy could be partly made up by the higher supernova rate.

In our analysis, we consider the mass hierarchy. For normal hierarchy, the survival probability $\bar{P} = 0.68$, see Sec. 2.2.2. While for inverted hierarchy, we are using the survival probability as 0, meaning that all the detected neutrino flux is from the original μ and τ neutrino flux. For more realistic case, for 17.3 MeV threshold, we have our results shown below, with NH and IH separately, in the interval of 68%, 90%, 99% C.L., see Table 2.3.

Table 2.3: The predicted flux of $\bar{\nu}_e$ in a detector above 17.3 MeV, in the point of maximum likelihood and in the intervals of 68, 90, 99% C.L.

	best fit	68% C.L.	90% C.L.	99% C.L.
NH	0.27	0.22 - 0.34	0.16 - 0.42	0.12 - 0.59
IH	0.24	0.19 - 0.32	0.14 - 0.33	0.10 - 0.49

NH favors higher fluxes than IH. This is because NH has higher survival probability of $\bar{\nu}_e$.

Table 2.4: Neutrino Events Rate in 1Mton detector.

N yr^{-1}	E>19.3 MeV	E>17.3 MeV	E>11.3 MeV
99% *C.L.*	5.0-32.6	7.28-40.5	17.5-76.5

2.4.2 Expected neutrino events rate

Large volume water Cherenkov neutrino detectors have been operating for years and the technique is well known. The expected inverse beta decay events rate can be calculated as:

$$N_e(E_p, D) = \frac{N_p \sigma(E_p) F_{\bar{e}}(E_p - \Delta M)}{4\pi D^2}, \tag{2.39}$$

Our results are shown in Table 2.4. For 1Mton water detector, with Gd addition, 76 events could be detected per year. Even with higher energy threshold, 17.3MeV, 40 events could be observed per year.

Here we also calculate the number of events per year for NH and IH at three C.L. with 17.3 MeV threshold, see Table 2.5. The atmospheric neutrino background is obtained by integrating the flux given by Fig. 1.4. As discussed, when the energy is larger than 30 MeV, the atmospheric background dominates. Therefore, we search neutrino signals up to 30 MeV. The calculated background rate is 12 events per year.

Table 2.5: The predicted event rate for a 1Mton water Cherenkov detector above 17.3 MeV, in the point of maximum likelihood and in the intervals of 68, 90, 99% C.L.

	best fit	68% C.L.	90% C.L.	99% C.L.	Atm. BG
NH	18.8	14.9 - 23.7	11.1 - 30.1	7.28 - 40.5	12
IH	14.8	11.8 - 19.9	8.60 - 21.3	5.88 - 31.3	12

Table 2.6: The predicted event rate for a 100 kton liquid argon detector, in the point of maximum likelihood and in the intervals at 68, 90, 99 % C.L.

Nyr^{-1}	E>19.3 MeV	E>15.5 MeV	E>11.3 MeV
$99\% C.L.$	0.18-1.19	0.39-1.98	0.81-3.06

Compared to water detector, a liquid argon neutrino detector has its advantage: it is more sensitive and dense. It is strongly sensitive to electron neutrinos by the interaction,

$$\nu_e + ^{40}Ar \rightarrow X + e^-, \tag{2.40}$$

where X presents any possible products. Although we don't have electron neutrino spectrum from SN1987A, there is a possibility that $F_{\bar{e}} = F_e$. With this assumption, we use Eq. 2.39 to calculate the event rates with the cross section in [88] and 1.51×10^{33} target particles corresponding to a mass of 100 kton detector.

The potential problem to detect DSNB is the background rate which determines the energy window. For liquid argon detector, the main background is still atmospheric neutrinos. For 100 kton size detector, the atmospheric background is 0.45 events per year with energy from 19.3 to 30 MeV.

From the calculation results of two types of detectors, we can see the neutrino signal events could exceed the background events. It is realistic to observe the diffuse supernova neutrino background.

2.5 Discussion and conclusion

In this work, we update the previous work by Lunardini [73]. To estimate the diffuse supernova neutrino background, we need three ingredients: supernova neutrino spectrum, oscillations, cosmic supernova rate. Therefore, we use SN1987A data to constrain the model of neutrino emission, including neutrino oscillation, and analyze the most recent supernova rate measurements. We evaluate the diffuse supernova neutrino background signals in both Mton water Cherenkov detector and liquid argon detector.

The detection of neutrinos from SN1987A provided the most direct information on supernova neutrinos. We calculate the likelihood functions for the data from Kamiokande-II and IMB and find the best fit values and allowed regions of parameter space at various C.L.. We determine the neutrino spectrum with these parameters.

We discuss the neutrino oscillation from the production site to the detector. During the propagation, neutrinos undergo collective oscillation in the inner region of the supernova and MSW effect in the outer region of the supernova and in the earth. The oscillations depend on the mass hierarchy, especially for antineutrinos. With the well measured large value of θ_{13}, for normal hierarchy, we take the survival probability of $\bar{\nu}_e$ as 0.68; for inverted hierarchy, we take it as 0.

The observation of supernovae is getting precise and rapidly improved. We fit the supernova rate data up to redshift ~ 1.1 with three sets of uncertainties: (1). statistic only, (2). statistic with systematic, (3) statistic and systematic with correlations. Our best fit of supernova rate at z=0, is a factor of 2 lower than that predicted by SFR. This is due to part collapses that are intrinsically faint, truly dark or simply obscured.

The uncertainty on the diffuse supernova neutrino background calculation is dominated by SN1987A data. It has been suggested that the supernova emission should be larger by indirect evidence and theory. Since SN1987A is the only observed supernova neutrino emission, we do not know if it is a typical supernova. Scientists are looking forward to other supernova neutrino bursts to assure this question.

Our estimated flux is 5 times lower than the SK upper limits in 2012. This discrepancy could be made up if we have higher supernova rate and larger supernova neutrino emission. Even with these uncertainties, after comparing our neutrino events with background events, we could say there could be a few DSNB neutrino events in a detectors, like SK, however a larger detector is needed to establish the DSNB with high confidence.

Chapter 3

Detectability of neutrinos from failed supernovae

3.1 Failed Supernovae

3.1.1 Failed supernovae

As discussed in Chapter 2, supernovae are classified into various types, Type Ia, Type II, Type Ib, and Type Ic, according to their different absorption lines of typical chemical elements in the spectra. Those stars more massive than 10 $M_\odot$ (with $M_\odot$ solar mass) will end their lives with the gravitational collapse of their electron degenerate iron core. In general, stars with mass range of 10 – 25 $M_\odot$, would undergo a violent explosion and emit neutrino bursts lasting 10 – 20 s. They leave proto-neutron stars as remnants. These successful collapses are known as neutron star forming collapses (NSFC).

Stars with mass exceeding 25 $M_\odot$, may have black holes as outcomes, due to their larger iron cores. This phenomenon could occur in several mechanisms: (1) the remnant neutron star is pushed over its stable mass limit by the fallback accretion [89]; (2) during the proto-neutron star cooling process, nuclear phase transitions occur [90]; (3) fallback after a successful core collapse explosion [91]. The direct black hole forming collapses (DBHFC) are also called failed supernovae. They disappear immediately after the core implosion with no emission of electromagnetic signals. Only neutrinos and gravitational waves escape from these stars. Neutrinos are the unique massager taking the information to the earth.

The minimum mass of stars producing DBHFCs are predicted between 25 to 40 $M_\odot$ [92, 51]. According to the initial mass function, this corresponds to $9-22\%$ of all core collapses. Neutrinos are the only tracers of failed supernovae. Due to their long mean free path, they could freely propagate to the earth and provide important information of the mechanisms of direct black hole formation.

To date, neutrino detectors have only detected neutrino signals from two astrophysical sources, the Sun and SN1987A. In our galaxy, the predicted supernova rate is 1 – 3 bursts per century [93]. Therefore, the neutrino observation is limited by the long waiting times. The observation of neutrino bursts from distant sources is more difficult due to the smaller flux arriving to the earth. At the largest neutrino detector, Super-Kamiokande, (22.5 kton fiducial volume), there is still no positive result. Therefore enlarging the water Cherenkov technology to Mton scale is needed. In our work, we study the the detectability of neutrino bursts from DBHFCs with Mton size neutrino detector.

Numerical simulations show that the neutrino bursts from DBHFCs last ~ 1 second or less [94, 95], and has high luminosity, up to $L \sim 10^{53}$ ergs. The high average energy is higher than for NSFC, due to rapid contraction of the newly formed protoneutron star preceding the black hold formation. With these characteristics, it may realistic to observe neutrino bursts emitted from local DBHFCs.

Fig. 3.1 (taken from Fig. 2 of [95]), shows the average energy and luminosity from a progenitor with 40 $M_{\odot}$. We can see that the produced electron neutrinos and antineutrinos have even higher energy than neutrinos of other flavors, with up to 2×10^{53} ergs luminosity and 20 – 24 MeV average energy, due to high rate of electron and positrons captures on nuclei. Time duration is strongly dependent on the equation of state (EOS).

To estimate the observability of DBHFCs, we use the core collapse rate within 10 Mpc, taken from [96]. In their work, Shinichiro Ando et al. take the dust-corrected measurements from GALEX, and adopt the star formation rate at z=0.

In our study, we convert the core collapse supernova rate to the failed supernova rate, calculating the fraction of stars above 25 – 40 $M_{\odot}$ of all stars above 8 $M_{\odot}$. We

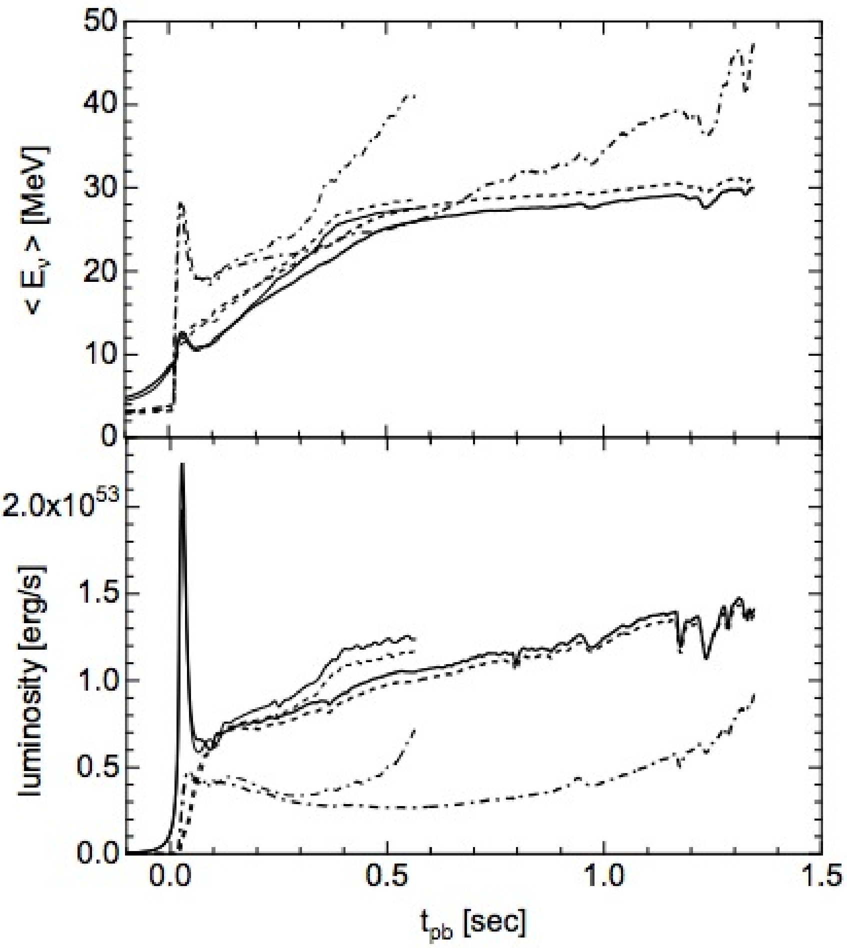

Figure 3.1: Average energies (upper) and luminosities (lower) of ν_e, $\bar{\nu}_e$, ν_x are presented as solid, dashed, dot-dashed lines for Lattimer-Swesty (thin) and Shen et al. (thick) equation of state as a function of time after bounce.

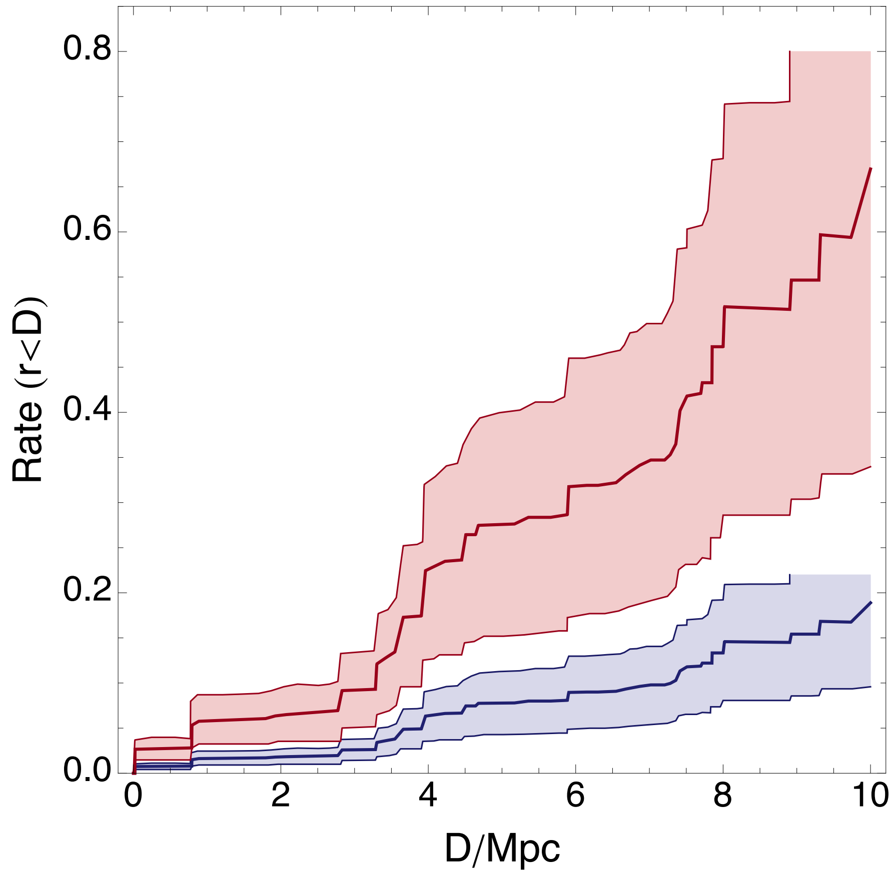

Figure 3.2: The upper shaded region with uncertainty is the cumulative NSFC rate and the lower one is the cumulative DBHFC rate within 10 Mpc. Here the fraction of DBHFC f_{BH}=0.22 is used.

assume this fraction as a distance-independent constant, 0.1 – 0.22. Fig. 3.2 shows the rates of two types of collapses per year within distance D with uncertainty.

This figure shows that there is a rapid increase of core collapse rates at 3 – 5 Mpc, due to the presence of several galaxies (mainly IC 342, NGC 2403, M 81, M 82, NGC 4945) in this interval. This is well within the typical distance of sensitivity of Mton detectors.

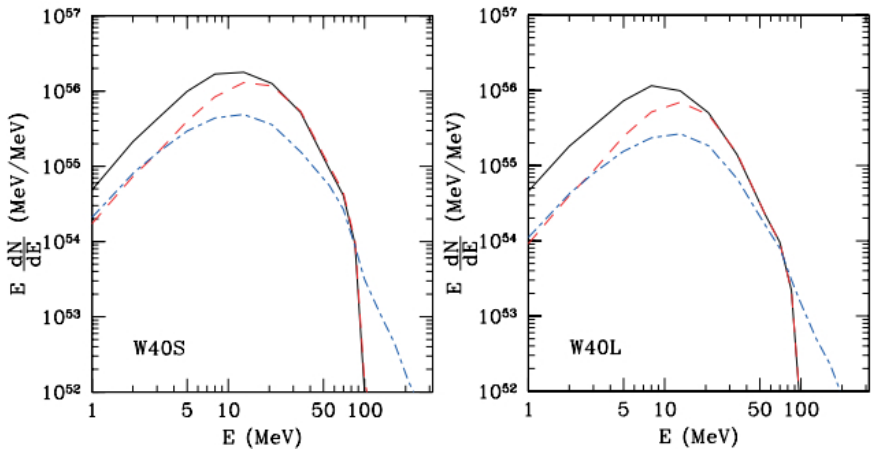

Figure 3.3: Original BH fluxes from Sumiyoshi et al. paper, left one is with EOS by Shen et al., the right one is with Lattimer & Swesty EOS. The ν_e (solid), $\bar{\nu}_e$(dashed), ν_x (dot-dashed) are shown.

3.1.2 Neutrino flux from failed supernova

For DBHFCs, we take the original neutrino fluxes before oscillation from Fig. 5 of Sumiyoshi et al. [97] (see Fig. 3.3). They adopted the 40 $M_\odot$ star model by Woosley & Weaver(1995). We then consider two sets of EOS of nuclear matter, one by Lattimer & Swesty (LS, 1991) [98], another by Shen et al. (1998) [99].

The LS-EOS is based on the non-relativistic liquid drop model, while Shen-EOS is based on the relativistic mean field theory and is stiffer. As studied in [100], the time between bounce and explosion increases with the stiffness of the EOS. For this reason, the formation of a black hole is easier and faster for Shen-EOS. The emitted total energy of neutrinos with LS-EOS is less than with Shen-EOS. In the plots, ν_x is assumed to have the same flux as $\bar{\nu}_x$.

Before neutrinos arrive at the detector, they undergo flavor conversion, see Sec. 2.2.2. In the water Cherenkov detector, the main detected interaction mode is inverse beta decay, $\bar{\nu}_e + p \to n + e^+$. The $\bar{\nu}_e$ flux detected is an admixture of the unoscillated flavor fluxes: $F_{\bar{e}} = \bar{p}F^0_{\bar{e}} + (1-\bar{p})F^0_x$. Hereafter x represent μ and τ flavors, $\nu_x = \nu_\mu, \bar{\nu}_\mu, \nu_\tau, \bar{\nu}_\tau$, and $\bar{p}$ is the survival probability. The survival probability of electron antineutrino can be expressed:

$$\bar{p} \simeq 1 - sin^2\theta_{12} = cos^2\theta_{12} \tag{3.1}$$

with normal mass hierarchy, and $sin^2\theta_{12}$=0.32. If with inverted mass hierarchy, the survival probability is:

$$\bar{p} \simeq P_H cos^2\theta_{12}, \tag{3.2}$$

where P_H is the flip probabilities at H resonance, (see Chapter 2). For a large mixing angle θ_{13}, $P_H \simeq 0$ [70]. Therefore it can be seen the $\bar{p}$ is between 0 – 0.68. In our work, we consider the extreme values of $\bar{p}$, 0 and 0.68.

3.2 Detectability of neutrino bursts

3.2.1 Number of neutrino events per burst

For a single burst, the neutrino event number as a function of distance D can be calculated as,

$$N(D) = \int_{E_{th}}^{E_{cut}} N_{E,D}(E_p)dE_p, \tag{3.3}$$

where E_p is the positron energy, $N_{E,D}(E_p)$ is the positron spectrum, as seen Eq. 2.39 for NSFC, E_{th} is the energy threshold of the detector, E_{cut} is the upper limit of the energy window, defined so that at least 80% of the events fall in the energy window $[E_{th}, E_{cut}]$. The lower limit, 16 MeV comes from the Super-Kamiokande energy threshold, discussed in Chapter 2 [84]. Fig. 3.4 gives the positron energy spectrum for a star at D= 1Mpc. For comparison, both NSFC and DBHFC results are shown in the figure. For NSFCs, the energy window is from 16 to 33 MeV; in total there are 14 events. While for DBHFCs the events number is 64, which is 4 times larger than NSFCs. The number of events increases with the survival probability $\bar{p}$.

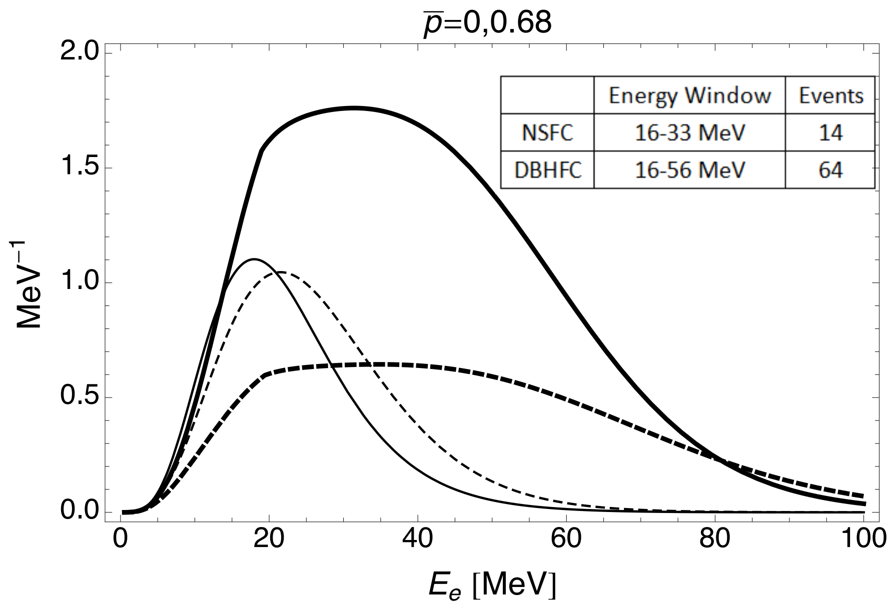

Figure 3.4: Positron energy spectra for a failed supernova (thick curves) and a neutron star forming collapse (thin curves) at 1 Mpc distance, with a Mton detector. Solid curves represent $\bar{p}_e$ survival probability $\bar{p}$=0.68, the dashed curves stand for $\bar{p}$ =0. The table shows the number of events detected in a given energy window.

3.2.2 Burst identification and rate

The duration time Δt of a failed supernova burst is less than 1s, for NSFCs it is about 10s. If there are at least N_{min}=2, 3 neutrinos detected within Δt and the energy window, they can be identified as a neutrino burst. The neutrino event number $\mu(D)$ is proportional to D^{-2}. E. g., for a failed supernova $\mu(D) = 64(Mpc/D^{-2})$. Requiring $\mu(D) = N_{min} = 2$, we find that the range of detectability of failed supernovae can go as far as 5.6 Mpc.

For a 1Mton detector, the probability of detecting N $\geq N_{min}$ neutrinos from a supernova at distance D , follows Poisson distribution:

$$P(N_{min}, D) = \sum_{n=N_{min}}^{\infty} \frac{\mu(D)}{n!} e^{-\mu(D)} \tag{3.4}$$

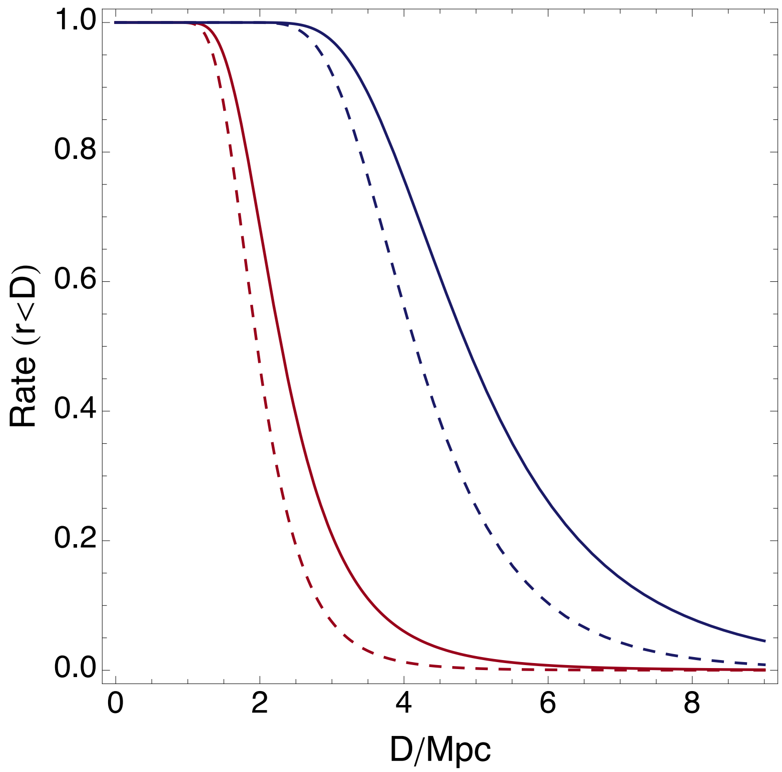

Figure 3.5: Detection probability for NSFC (red) and DBHFC (blue), with N_{min} = 2, 3, solid and dashed curves respectively. Here $\bar{p}$=0.68 is used as in Fig. 3.4.

In Fig. 3.5, we see the probability of detection of a neutrino burst (N $\geq N_{min}$=2, 3). Requiring that this probability is as large as 80 percent, the sensitive distance can reach 4 – 4.5 Mpc for DBHFC, and 2 – 2.5 Mpc for NSFC. From Fig. 3.2, it appears that it is very possible to observe neutrino bursts from failed supernova within 9 Mpc distance.

Then the rate of detection of bursts from failed supernovae can be expressed as:

$$R(N_{min}, D)_{BH} = \sum_{i, D_i < D} P(N_{min}, D_i) \Delta R_i \tag{3.5}$$

where ΔR_i is the DBHFC rate in each distance bin i. The equation above is a sum over the distance bin D_i. Similarly, one can obtain the rate of detection R_{NS}

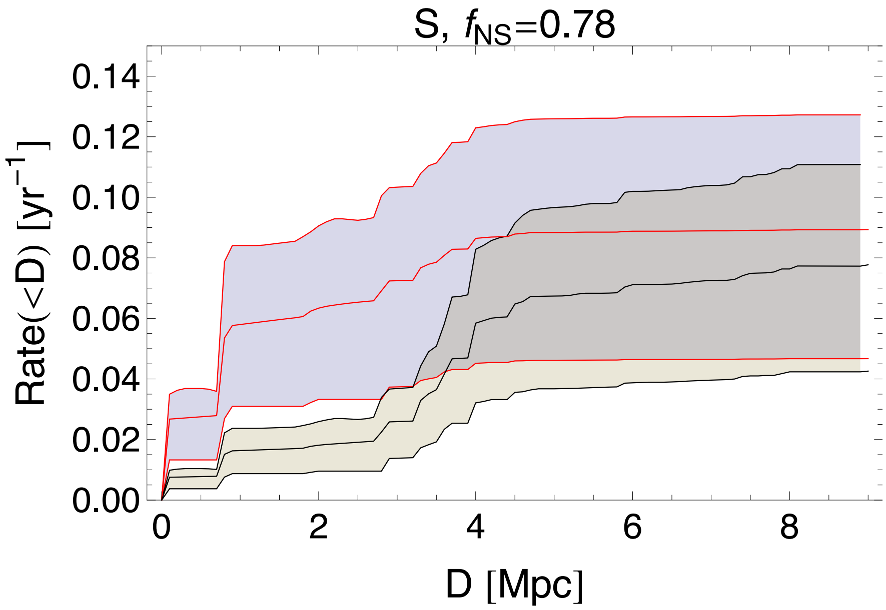

Figure 3.6: With Shen-EOS, and the fraction of NSFC f_{NS}=0.78, the upper shaded regions gives the rate of detection of neutrino bursts from NSFC, and the lower one shows that from DBHFC.

of bursts from NSFCs. The calculated results can be seen in Fig. 3.6. The rates reach an asymptotic limit after 4 Mpc for NSFCs, and at 9 Mpc for DBHFCs. The flattening is due to the small detection probability at larger distance. Depending on the normalization of core collapse rate, the burst rates with $N_{min} = 2$ reach $R_{NS} \sim 0.05$ – 0.13 per year, $R_{BH} \sim 0.04$ – 0.11 for NSFC and DBHFC respectively. Therefore, it is possible to detect neutrino signals from failed supernovae, whose detection rates are comparable to ordinary core collapse. The detector could have two detections within 10 years.

3.2.3 Background rate

If the estimated detection rates exceed the corresponding background rates, then a detected burst can be identified as being from a supernova with considerable likelihood. For the Super-Kamiokande (SK) detector [84], the main backgrounds are cosmic muon-induced spallation products, solar neutrinos, atmospheric neutrinos, reactor neutrinos and radioactivity as discussed in Chapter 1. The interactions of cosmic rays can produce high energy muons and neutrinos. These muons can spall oxygen nucleus ($\mu +^{16} O \rightarrow \mu + X$) and generate unstable nuclei X, which decay into neutrons and then fake neutrino signals. These spallation products have energy up to 21 MeV. Therefore, the need to remove these backgrounds determines the lower energy threshold. The spallation cut utilizes a likelihood method, and has been improved to 16 MeV with 91% efficiency.

The remaining muons from the interaction of atmospheric ν_μ can be removed by Cherenkov angle cut. Since positrons with energy larger than 18 MeV have a Cherenkov angle of 42 degrees. Heavier charged particles, like muons, pions, may have a Cherenkov angle less than 42 degrees. Therefore the events with Cherenkov angle less than 38 degrees would be cut. For muons from charged current interactions of atmospheric ν_μ with decay electrons can mimic neutrino signals. These muons can be removed by time correlation due to the products with shorter lifetime. Solar neutrinos can be removed due to their direction. Gamma rays from the surrounding rocks and detectors may be cut by the travel distance less than 450 cm.

By rescaling the Super-Kamiokande background rates by the volume ratio $\left(\frac{Mton}{22.5kt}\right)$, within the same energy and time windows, the rate of accidental coincidences of unrelated events is $\lambda = 1855yr^{-1}$, $\lambda = 680yr^{-1}$ for DBHFC and NSFC respectively. The rates of two and three unrelated events within duration Δt are:

$$\int_0^{\Delta t} \lambda e^{-\Delta t \lambda} dt \simeq \lambda^2 \Delta t \tag{3.6}$$

$$\int_0^{\Delta t} \lambda^2 \Delta t e^{-\Delta t \lambda} dt \simeq \lambda^3 \Delta t^2 \tag{3.7}$$

Therefore, with some simple calculation, one has the rate of coincidence of two or three such uncorrelated events in the time window for failed supernova (Δt=1s), $\omega_{2,BH} \sim$

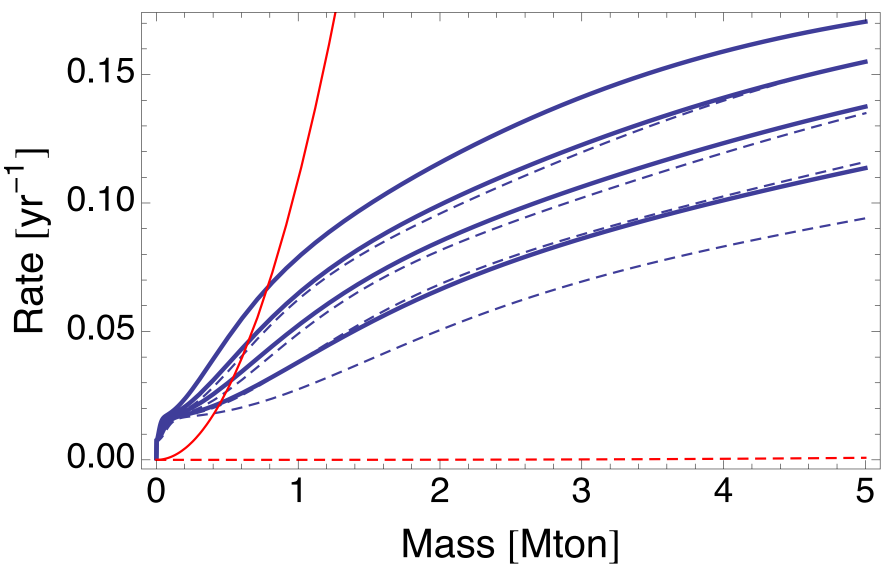

Figure 3.7: Red curves represent background rates,(ω_2 solid and ω_3 dashed.) The solid blue lines show R_{BH} for N_{min} = 2, changing with $\bar{p}$, 0, 0.2, 0.4, 0.68, from lower to higher.The dashed blue lines are the same results while N_{min} = 3.

$0.10yr^{-1}$, $\omega_{3,BH} \sim 6.4 \times 10^{-6} yr^{-1}$, and for NSFCs with Δt=10s, $\omega_{2,NS} \sim 0.15 yr^{-1}$, $\omega_{3,NS} \sim 3.1 \times 10^{-5} yr^{-1}$.

For both DBHFC and NSFC, the background doublet rate is comparable to or slightly higher than the burst rate. Therefore, if there are two detected events in such short time window, a supernova detection could be claimed. If there are three detected events, it is certainly identified as a supernova detection.

Since $\omega_2 \propto \lambda^2 \propto M^2$, $\omega_3 \propto \lambda^3 \propto M^3$, the background rates depend on the mass of the detector, quadratically. Also, the detection rate R_{BH} increases with M and with $\bar{p}$, as seen in Fig. 3.7. For $N_{min} = 2$, when the mass of the detector is beyond 0.8 Mton, the background rate is higher than the neutrino burst rate. However for $N_{min} = 3$, the neutrino bursts rate is much higher than the background rate. R_{BH} is also proportional to f_{BH}, which corresponds to the fraction of failed supernovae.

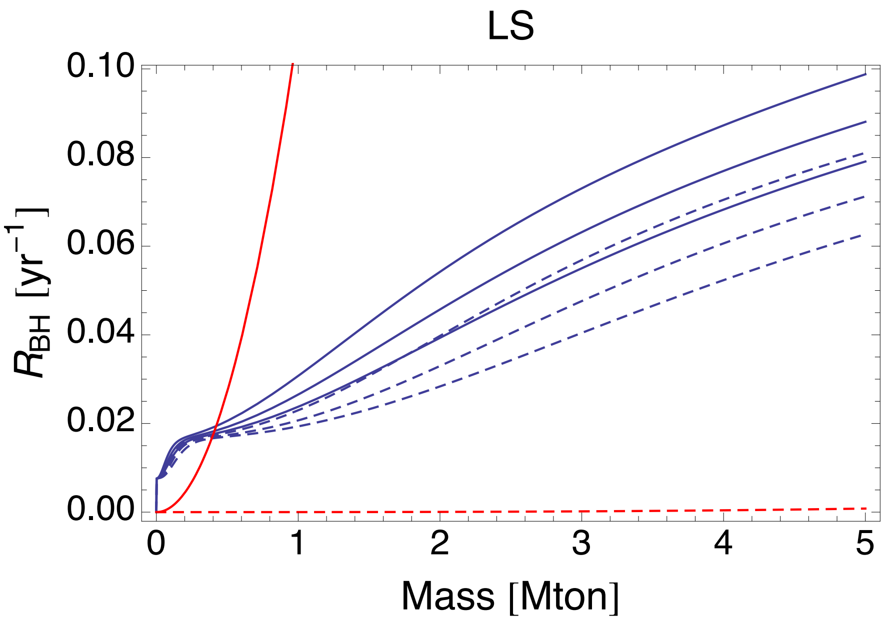

Figure 3.8: Red curves represent background rates,(ω_2 solid and ω_3 dashed). The solid blue lines show that $N_{min} = 2$, R_{BH} change with $\bar{p}$, 0, 0.2, 0.4, 0.68, from lower to higher.The dashed blue lines are the same results while $N_{min} = 3$.

For different EOS, the results vary. With the LS-EOS, the emitted neutrinos from failed supernova are less luminous and have lower average energies. The Fig. 3.8 shows the results for the LS-EOS, one of the results of the LS-EOSwill have lower neutrino burst rates due to the reduction of distance sensitivity. With the same quantities, with $N_{min} = 2$, $R_{BH} \simeq 0.016 - 0.045\ yr^{-1}$. When the mass of the detector is beyond 0.4 Mton, the identification of the neutrino bursts with background bursts is much harder.

3.3 Conclusion

The expected rates of detection of neutrino bursts from failed supernovae for a Mton scale water detector depend on the size (mass) of the detector, fraction of failed supernovae, equation of state, and survival probability. It is a realistic possibility to have a detection rate of one per decade, which means that a detection would be likely within the lifetime of the detector. More inspiring, once the neutrino bursts contain at least three neutrinos within the short time duration, approximate 1s, it is easily distinguishable from the background events and with identify a failed supernova.

Due to the properties of failed supernovae, invisibility, high neutrino luminosity and high average energy, and short time duration of the neutrino burst, a neutrino water Cherenkov detector is possibly the only way to reveal local failed supernovae. The observation might tell us how a black hole forms via collapse, what the mechanism is. It might also explain why the bright supernova rate is lower than the star formation rate, see Sec. 2.1.3.

Chapter 4

Ultra high energy neutrinos

4.1 Ultra high energy neutrino propagation

In the previous chapters, I discussed the big bang relic, solar, supernova bursts 1987A, reactor, supernova relic and atmospheric neutrinos with energies from eV to TeV scale. Extending this range to higher energies will reveal new phenomena in the early universe.

Since the discovery of the neutrino in the 1950's, people realized that neutrino is possibly a unique messenger for astronomy. Although the invention of the gamma ray telescope has been advanced, photons are limited to energies above tens of TeV due to the interaction of these photons with background photons, $\gamma\gamma_B \to e^+e^-$. The threshold of this reaction is $4E_\gamma E_{\gamma_B} \approx 4m_e^2$ [101]. Then the TeV photons are attenuated by the infrared background and PeV photons by the cosmic microwave background. Neutrinos can travel cosmological distance without being absorbed. Furthermore, the ultra high energy (UHE) neutrinos with $E > 10^{11}$ GeV provide unique opportunity to test the fundamental interactions.

The UHE neutrinos can directly carry the information from the distant sources or deeply hidden sources. The high energy neutrino observations are primarily motivated by the search for point sources, which could help to identify the sources of cosmic rays, and by the search for diffuse neutrino flux [28]. The relevant experiments to this high energy regime have shown successful progress and exciting results. IceCube has recently reached the PeV energy scale [10]. A new generation of detectors is expected to operate soon and start to probe the parameter space predicted by theory. The detection of UHE neutrinos will help distinguishing between various models of neutrino fluxes in great detail and studying the neutrino oscillations and absorption.

4.1.1 UHE neutrinos

UHE neutrinos can be produced in two mechanisms, acceleration processes and annihilation or decays of exotic massive particles. They can provide information about distant astronomical objects, such as gamma ray bursts (GRB), active galactic nuclei (AGN), and possible exotic sources like heavy relics and topological defects. The detailed description will be elaborated below.

The UHE neutrinos are largely absorbed by the cosmic neutrino background (CνB) via scattering. Due to this effect, the universe is transparent for neutrinos up to a redshift z_t. For energies $E \gtrsim 10^{11}$ GeV, the neutrino horizon is $z_t \sim 140$ [102]. The mean free path of neutrinos depends on the neutrino energy and mass, and it is resonantly suppressed due to neutrino-antineutrino annihilation via the Z^0 boson (resonant absorption). The shape of the horizon is rather complicated. This annihilation causes one or more characteristic absorption dips in the neutrino spectrum.

The signature of resonant absorption was first studied by Weiler in 1982 [103], with the so called "Z-dip" scenario. Within decades, subsequent works made effort on modeling the sharp dips with the consideration of non-relativistic neutrino background [104, 105]. Then the thermal effect on the $C\nu B$ was taken into account for at least the lowest of the three masses. D'Olivo et al. [106] presented the thermal effect on the shape of the absorption dips for a single neutrino species. Further research on a more realistic three neutrino mass spectrum was done in [107], which provides the transmission probabilities. In our work, we develop the study of the absorption dips, including thermal effects exactly, by considering the three active neutrino species and discuss their dependence on the neutrino mass spectrum. Furthermore, the results are applied to a number of proposed mechanisms of production of UHE neutrinos.

4.1.2 Thermal effects

As discussed in Chapter 1, analogous to the cosmic microwave background, cosmic neutrino background is filling the universe and whose temperature at present epoch $T_0 \approx 1.697 \times 10^{-4}$ eV and a number density $n_{\nu 0} \approx 56 cm^{-3}$ per species. The energy of neutrinos can be expressed as,

$$E = \sqrt{p^2(1+z)^2 + m_j^2} \tag{4.1}$$

For a given mass eigenstate m_j, it is non-relativistic at $z \lesssim z_{\text{th},j}$:

$$(1 + z_{\text{th},j})\bar{p}_0 \sim m_j. \tag{4.2}$$

where $\bar{p}_0 = \sqrt{< p^2 >} = 3.597\, T_0 = 6.1044 \times 10^{-4}$ eV. Eq. (4.2) means that a mass eigenstate is non-relativistic at $z_{\text{th},j} \sim 16 \left(\frac{m_j}{10^{-2}\text{ eV}} \right) - 1$. For instance, a mass eigenstate $m_j \gtrsim 0.05$ eV) is non-relativistic at $z \lesssim 83$.

Therefore, when $z \gtrsim z_{\text{th},j}$, thermal effects become substantial for ν_j component of the $C\nu B$ in the scattering with UHE neutrinos. One could estimate $z_{\text{th},j}$ from Eq. (4.2) of the production redshifts where these effects should be included.

To numerically study thermal effects of $C\nu B$, we choose to work with eight representative mass spectra (see Table 4.1), four for each hierarchy, where the smallest mass equals $m_{\text{min}} = 10^{-5}, 10^{-3}, 2 \times 10^{-2}, 8 \times 10^{-2}$ eV. In order, these correspond to spectra that are extremely hierarchical, moderately hierarchical, moderately degenerate and very degenerate.

4.2 Neutrino absorption effects

From the production site to the detector, UHE neutrinos undergo oscillations and scatterings. The observed neutrino flux is significantly different from original one. The oscillation length $l_{osc} = \frac{4\pi E}{\Delta m^2}$ is about orders of 10 pc, which is much smaller than the

m_1	m_2	m_3
0.00001	0.0084	0.055
0.001	0.0084	0.055
0.02	0.022	0.058
0.08	0.080	0.097

m_1	m_2	m_3
0.055	0.055	0.00001
0.055	0.055	0.001
0.058	0.059	0.02
0.097	0.097	0.08

Table 4.1: Values of the neutrino masses (in eV) used in this work for NH (left) and IH (right).

distances L to the sources, $L \gg l_{osc}$. Therefore, $\langle sin^2(L/l_{osc})\rangle \approx 0.5$. The transition probability as in Eq. (1.10) is simplified as

$$P(\nu_\alpha \to \nu_\beta) = 2|U_{\alpha 3}|^2|U_{\beta 3}|^2 \tag{4.3}$$

Since in general all models UHE neutrinos are generated as the secondaries from pion decays.

$$\pi^{+,-} \to \mu^{+,-} + \nu_\mu(\bar{\nu}_\mu) \tag{4.4}$$

$$\mu^{+,-} \to e^{+,-} + \nu_e(\bar{\nu}_e) + \bar{\nu}_\mu(\nu_\mu) \tag{4.5}$$

The composition of neutrinos flux at the sources is $\nu_e : \nu_\mu : \nu_\tau = 1 : 2 : 0$. Then at observation the composition is 1:1:1, which is flavor equipartition. Before the UHE neutrinos reach the detector, they propagate through the CMB and $C\nu B$ without significant energy loss except the resonant annihilation of UHE neutrinos on relic neutrinos. Detectors are not usually sensitivity to neutrino flavor composition, however the resonant absorption dips are sizable in the spectrum. In our work, we focus on the resonant and non-resonant absorptions and include the effect of cosmological redshift.

4.2.1 Cross section

UHE neutrinos interact with relic neutrinos via several channels, $\nu\bar{\nu} \to$ anything. The total cross section $\sigma_{tot}(E, p, m_j, z)$ is summed over all the contributions from resonant and non-resonant channels. The cross sections of all the channels are summarized in Appendix B, and are shown in Fig. 4.1.

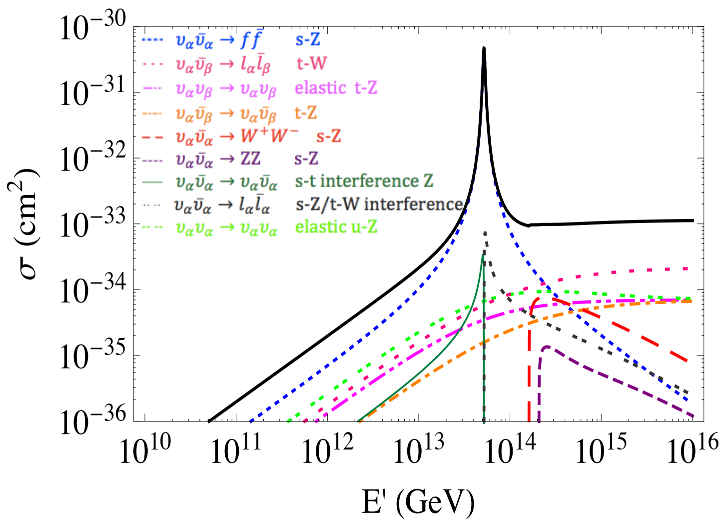

Figure 4.1: Cross sections (colors, thin) contributing to the $\nu\bar{\nu} \to$ anything process, and total cross section are shown (black, thick), for a representative neutrino mass $m_\nu = 0.08$ eV. Thermal effects are not included.

These cross sections are as functions of Mandelstam variable, which is,

$$s = (q^\mu + p^\mu)^2 \approx 2E' \left(\sqrt{p^2(1+z)^2 + m_j^2} - p(1+z)\cos\theta \right), \tag{4.6}$$

$$q^\mu = [E', \mathbf{q}], \tag{4.7}$$

$$p^\mu = \left[\sqrt{p^2(1+z)^2 + m_j^2}, \mathbf{p} \right], \tag{4.8}$$

where q^μ and p^μ are the four momenta of the UHE neutrino (beam neutrino) and the background neutrino, respectively, and E' = E(1+z), E is the beam neutrino energy at earth. And $\mathbf{q}\cdot\mathbf{p} \equiv p\ q\cos\theta$, θ is the scattering angle between them. Since beam neutrino is ultrarelativistic with $q \gg m_j$, we make the the approximation $E' = q$.

The resonant channel corresponds to annihilation of an UHE neutrino (antineutrino) with a background antineutrino (neutrino) via a Z^0 boson resonance in the s channel. The resonance occurs at $s = M_Z^2$, where $M_Z = 91.1876$ GeV is the Z^0 boson mass. As seen in Fig. 4.1, it is supposed the background neutrino at rest or $m_j \gg p$, which is realized for the $C\nu B$ at the present time and $m_j \gtrsim 10^{-3}$ eV. Hence the Mandelstam variable is $2E'm_j$, and the resonant peak is at energy of $M_Z^2/(2m_j)$.

There are totally nine non-resonant channels in our calculation. The detailed expression of total cross section is in Appendix B), and it shows three regimes in Fig. 4.1: sub-resonance, where the cross section linearly depends on the energy of the beam neutrino E'; at or near resonance, where the cross section is dominated by the resonant term; above resonance, where the non-resonant cross sections approach an asymptotic value $\sigma_{\rm nr} \sim 10^{-33}$ cm^2.

4.2.2 Thermal distribution of background neutrino

In the most general case, the momentum of the background neutrino is not negligible. The exact expression of s, given by Eq. (4.6), should be taken into account. To do so, we first study the differential cross section for resonant s-channel $d\sigma_r/d\Omega$, which depends on θ through s. Since $C\nu B$ is isotropic, to obtain the cross section σ_r, we integrate $d\sigma_r/d\Omega$ over the angular variables. The analytical result as in [106] is very complicated , see Appendix B. Compare it with the cross section with target neutrino at rest, see Fig. 4.2. It has a spread in the resonance peak. This feature could be explained as now the resonance is realized for an interval of the beam neutrino energy, corresponding to θ varying between 0 and π [see Eq. (4.6)]. The cross section at resonance is larger for a head-on collision, $\theta = \pi$. This is because, there, the energy E' required to realize the resonance is minimum, and therefore the prefactor $1/E'$ in the cross section [Eq. (B.2)] is less suppressed.

The calculation of the neutrino optical depth requires the convolution of the total cross section σ_Z for a given momentum of the background neutrino with the momentum distribution of the $C\nu B$ [Eq. (4.9)]. In our work, we calculate the cross section averaged over the momentum as in Eq. 4.10.

$$dn_\nu(p,z) = (1+z)^3 \frac{d^3p}{(2\pi)^3} \frac{1}{e^{p/T_0}+1} \ , \tag{4.9}$$

$$\bar{\sigma}(E;z,m_j) = \frac{\int dn_\nu(p,z)\, \sigma(E,p;m_j,z)}{\int dn_\nu(p,z)}. \tag{4.10}$$

In addition to the resonant channel, we take care of the non-resonant channels with the same considerations above. As seen in Appendix B, the non-resonant contributions are linear functions of s, therefore the smearing effect due to the background temperature is well captured by using an averaged value of s instead of the exact expression in Eq. (4.6):

$$\bar{s}(E,m_j,z) \sim 2E(1+z)\sqrt{\bar{p}^2(1+z)^2+m_j^2}. \tag{4.11}$$

For simplicity, we use this prescription to calculate the contribution of the non-resonant channels to the total momentum-averaged cross section, $\bar{\sigma}_{\rm nr}(E,m_j,z) = \sum\limits_i \sigma_{{\rm nr},i}(\bar{s})$, where $\sigma_{{\rm nr},i}(s)$ is the non-resonant cross section for a given channel, i (Appendix B).

Then we obtain the total cross section σ_Z averaged over all momenta and angles summed over all channels. For this calculation, we show σ_Z as functions of beam energies as in Fig. 4.3 with various background neutrino masses m_ν with temperature at present epoch (z=0). As expected, the smaller m_ν which is more comparable to the root mean square of the $C\nu B$ momentum $\bar{p}$, has more obvious effect of including the momentum distribution of the background than the others with larger masses. The resonant peak gets smoother and broader than others in addition to the broadening due to the angular integration, here the momentum distribution of the background further widening the range of beam energy where the resonance can be realized.

In Fig. 4.4, we show the same cross section with various background neutrino temperatures (various redshifts) with a fixed neutrino mass. As the temperature rises so that $\bar{p}$ becomes comparable to the mass. Hence, the thermal effects become important at redshifts larger than $z_{\mathrm{th},j}$ as in Eq. (4.2).

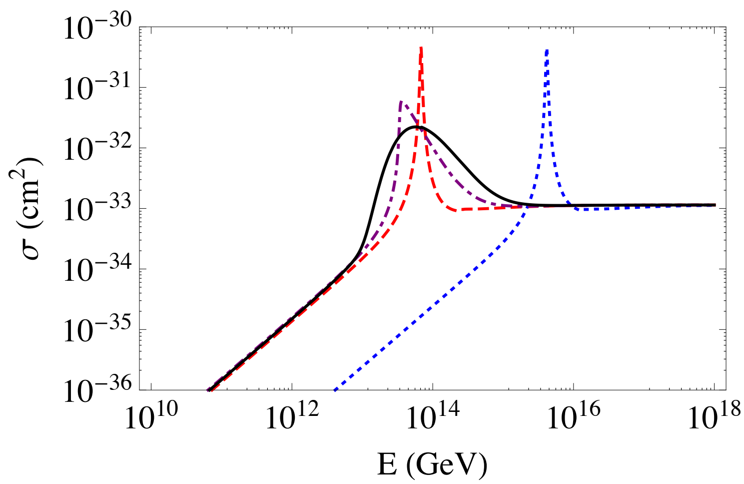

Figure 4.2: The total cross section for a source at z=100 with neutrino mass of 0.08 eV: (i) no thermal effects(Red with average momentum, blue with 0 momentum) (ii) cross section calculated at the average neutrino energy ($\sigma(\langle E \rangle)$, Purple) (iii) thermal effect(Black).

As a summary, the momentum-averaged cross section gives a fully realistic description, that can be compared with some approximate treatments of the problem, shown in Fig. 4.2. In order of sophistication, they include: (i) neglecting the background neutrino momentum altogether, which overestimates the energy of the resonant enhancement (ii) including the background temperature in the form of an effective neutrino mass $m_{\mathrm{eff},j} \simeq \sqrt{\bar{p}^2 + m_j^2}$, which reproduces the position of the resonance peak, and (iii) using the total cross section for the background neutrino momentum fixed at its root mean square value and averaged over the scattering angle. This captures in part the spread of the resonance peak over a range of energies. This range is further broadened for the full result, $\bar{\sigma}$.

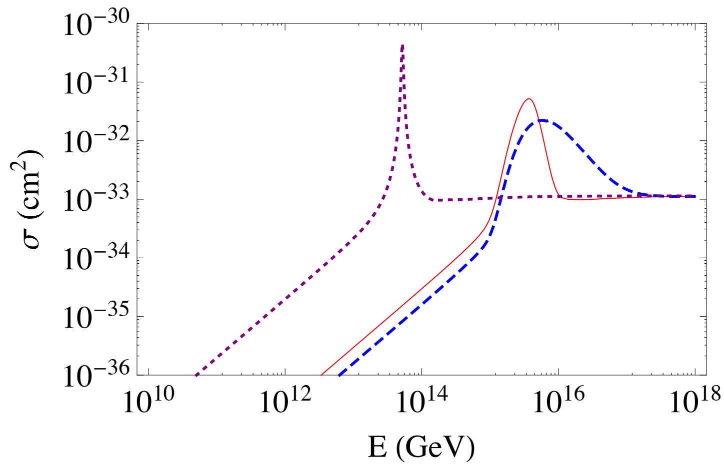

Figure 4.3: The total ($\nu + \bar{\nu} \to$ anything) cross section, inclusive of thermal effects, when averaged over a neutrino background with a momentum distribution as in Eq. (4.9), with temperature $T_0 = 1.697 \cdot 10^{-4}$ eV. Different lines correspond to neutrino masses: $m_\nu/\text{eV} = 8 \times 10^{-2}$ (purple-dotted), 10^{-3} (solid-red), 10^{-5} (dashed-blue).

4.2.3 *Optical depth and transition probability*

The scattering rate of an α flavor beam neutrino of energy E' on a background neutrino whose momentum distribution is given by Eq. (4.9) is

$$d\Gamma_i(E,p,m_{\nu_j},z) = \sum_{j=1}^{3} |U_{\alpha j}|^2 \, dn_{\nu_j}(p,z) \; \sigma_i(E,p,m_{\nu_j},z), \tag{4.12}$$

where the index j represents the mass eigenstate of $C\nu B$, the index i represents a specific interaction channel, and the sum is over all mass eigenstates. Therefore, the total interaction rate of an α flavor would be (see Appendix C for detailes)

$$\begin{aligned} \Gamma_\alpha(E',T) &= \sum_j |U_{\alpha j}|^2 \int \sigma(E',p,m_j) \; dn(p,T) \\ &\equiv \sum_j |U_{\alpha j}|^2 \; n(T) \; \bar{\sigma}(E',T,m_j), \end{aligned} \tag{4.13}$$

where σ_{tot} is summed over all the contribution channels and $n(T) = \int dn(p,T)$ is the number density of each neutrino species. Then we need to calculate the optical

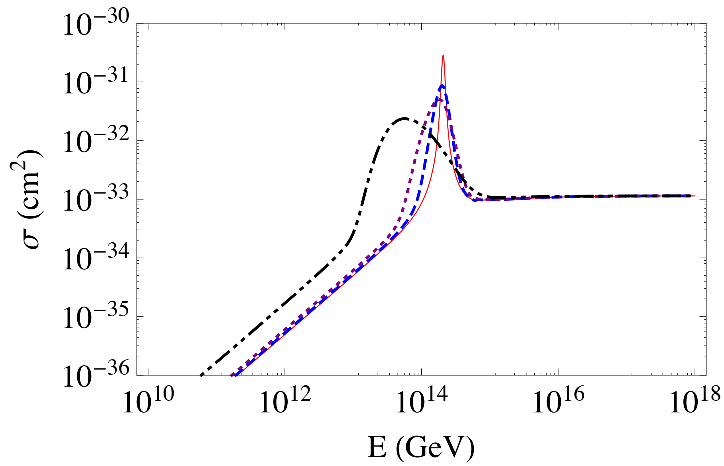

Figure 4.4: The total ($\nu + \bar{\nu} \to$ anything) cross section, inclusive of thermal effects, when averaged over a neutrino background with a momentum distribution as in Eq. (4.9) for the neutrino mass of $m_\nu = 2 \times 10^{-2}$ eV and a neutrino background with temperatures $T/\text{eV} = 3.394 \times 10^{-4}, 1.867 \times 10^{-3}, 3.56 \times 10^{-3}, 1.713 \times 10^{-2}$ corresponding to $z = 1$ (red-solid), 10(blue-dashed), 20 (purple-dotted), 100 (black-dash-dotted).

depth, with the consideration that the energy of the beam and the momentum and temperature of the background undergo redshift. This quantity expresses the total number of collisions of an α flavor beam neutrino with the $C\nu B$ through its path. It is the interaction rate integrated over the traveling time from t_0 to t(z), as

$$\tau_\alpha(E,z) = \int_{t(z)}^{t_0} dt' \; \Gamma_\alpha(E,T) = \int_0^z \frac{dz'}{(1+z')H(z')} \; \Gamma_\alpha[E, T_0(1+z')], \tag{4.14}$$

where the relation between proper time and redshift is $dt = \frac{dz}{(1+z)H(z)}$ in the Friedmann-Robertson-Walker metric, and T_0 is the temperature today. If a beam neutrino has more than one collisions with the background neutrinos during the propagation, $\tau_\alpha \gtrsim 1$, we could say the absorption is significant. For non-resonant channels, their total cross section is as constant when $s \gtrsim M_W^2$, which is approximately $\sigma_{\text{nr}} \approx \sigma_{tZ} + \sigma_{tW} \approx 7.8 \; G_F^2 \; M_W^2/\pi \sim 8.3 \times 10^{-34}$ cm^2 [see Eqs. (B.6) and (B.8)]. Therefore, we could use this value in Eq. (4.14), getting

$$\tau_{\text{nr}} \approx 1.0 \left(\frac{1+z}{140}\right)^{3/2}. \tag{4.15}$$

Therefore, we could estimate the neutrino horizon for $s \gtrsim m_W^2$, beyond which all the neutrinos are completely absorbed at all energies due to non-resonant scatterings. This horizon is expected at $z \gtrsim z_\nu \approx 140$.

Similarly, by using the maximum value of the resonant cross section, $\sigma_{\rm r} \sim 5 \times 10^{-32}$ cm^2 [Eq. (B.4)], we get an estimate of the optical depth for the resonant channels:

$$\tau_{\rm r} \approx 1.0 \left(\frac{1+z}{10}\right)^{3/2}. \tag{4.16}$$

Thus, resonant absorption occurs if the beam energy is around the resonant energy $E'_{\rm res} \sim m_Z^2/\sqrt{\bar{p}_0^2(1+z)^2+m_j^2}$ at $z \gtrsim z_{\rm dip} \approx 10$.

Then we could get the suppression of a number of neutrino ν_α N(0) produced at redshift z and arriving at the Earth with energy E,

$$P_\alpha(E,z) = \frac{N(E,z)}{N_0} = e^{-\tau_\alpha(E,z)}. \tag{4.17}$$

The UHE neutrino detectors are not sensitive to neutrino flavor. So the flux-averaged transmission probability can be shown as

$$P(E,z) \equiv \frac{\sum_\alpha \phi_\alpha(E) P_\alpha(E,z)}{\sum_\alpha \phi_\alpha(E)}\ , \tag{4.18}$$

here $\phi_\alpha(E)$ are the flux of neutrinos and antineutrinos of a given flavor α (under the assumption that neutrinos and antineutrinos have the same transmission and oscillation probabilities, which is justified for a CP-symmetric neutrino background). As discussed before, the flavor composition is $\phi_e : \phi_\mu : \phi_\tau = 1 : 1 : 1$ at all energies. Eq. 4.18 could be simplified as,

$$P(E,z) = \frac{1}{3}(P_\nu(E,z)+P_\tau(E,z)+P_\mu(E,z)). \tag{4.19}$$

Fig. 4.5 illustrates the features of P_e, P_μ, P_τ and P. It is expected to exhibit three suppression dips for every probability, named D_1, D_2, D_3, corresponding to the three values of the neutrino masses, m_1, m_2, m_3. Since neutrinos have resonant absorption at beam neutrino energy of $\sim M_Z^2/m_j$, the smaller background neutrino mass m_j has resonance at higher beam neutrino energy and with broader resonant cross section peak seen in Fig. 4.3. Therefore the order of the dips with increasing energy is the inverse of the order of masses, therefore the order is D_3, D_2, D_1 for NH and D_2, D_1, D_3 for IH. And the dips get more and more broader. For z larger than a few, D_1 and D_2 get merged into a single dip (D_{12}) due to the thermal effects. This is because the mass gap is comparable with the neutrino average momentum, $m_2 - m_1 \lesssim 10^{-2}$ eV $\simeq \bar{p}$ at redshift $z = 10$. And it could be observed for P_e the dip D_3 is suppressed, as a result of U_{e3} being small. This explains the dip structure of the flavor-averaged probability, P, and in particular the fact that the lowest energy dip is less deep for NH than for IH.

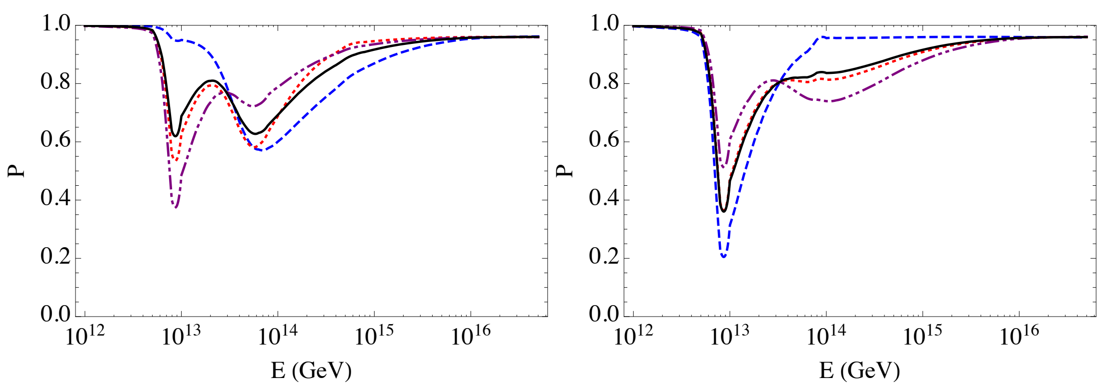

Figure 4.5: Transmission probabilities for UHE neutrinos with different flavors P_e, P_μ, P_τ (Blue, Red, Purple) and the average survival probability, P (Black) for a source at $z = 10$. Left (right) panel is for normal (inverted) hierarchy. The lightest neutrino has mass m_1 $(m_3) = 10^{-5}$ eV.

Fig. B.4 shows the the dependence of P on the energy, on the production redshift and on the background neutrino mass for NH and IH. We can see as the background neutrino mass spectrum from hierarchical to degenerate, the dips merge closer to each other. And for $z \gtrsim 10$, resonant absorption becomes substantial ($P \lesssim 0.5$) as expected from Eq. (4.2). For $z \sim 50-100$, the three absorption dips fuse into a single wide suppression well, that spans more than one oder of magnitude in energy; suppression in the regime above resonance ($s \gtrsim m_W^2$) is of more than 50%. Finally, for $z \sim 200$ far beyond the neutrino horizon, suppression is nearly complete at $E \gtrsim 10^{11}$ GeV, where the non-resonant contribution to the cross section alone is enough to have $\tau(E,z) > 1$.

4.3 UHE neutrino sources

In the universe, the UHE neutrino fluxes are usually the production of two mechanisms. One is top down scenarios, where UHE neutrinos are produced from decay of relics of superheavy particles, and topological defects, like cosmic necklaces and cosmic strings. Another is acceleration mechanism (astrophysical neutrino sources), where relatively low energy particles get UHE through multiple interactions in the sources, such as cosmogenic neutrinos and active galactic nuclei.

UHE neutrinos are expected to be detected in the form of a diffuse flux from all the sources in the universe. To calculate this flux, it is necessary to model the number of sources per comoving volume, per unit of physical time, t:

$$\eta(z) \equiv \frac{1}{r^2}\frac{d^3N_\mathrm{s}}{d\Omega dr dt} \ , \tag{4.20}$$

and the neutrino flux from a single source:

$$\phi(E') \equiv \frac{dN_\nu}{dE'} \ . \tag{4.21}$$

The product of the two gives the emissivity of an ensemble of sources:

$$\mathscr{L}_\nu(E',z) = \eta(z)\phi(E') \ , \tag{4.22}$$

with this, we get the diffuse flux (i.e., the number of neutrinos per unit energy per unit area per unit time per solid angle), in terms of the neutrino energy at Earth $E = E'/(1+z)$ [105]:

$$J_\nu(E) = \frac{1}{4\pi}\int_0^\infty \frac{dz}{H(z)}\, P(E,z)\, \mathscr{L}_\nu[E(1+z),z], \tag{4.23}$$

where Eq. (1.14) was used, and $P(E,z)$ is the average transmission probability given by Eq. (4.19).

Due to the integration over redshift, the suppression of the diffuse flux is less rich of structures compared to the case of a single source at fixed redshift. Therefore, we expect that only a single, wide suppression dip will appear in the neutrino spectrum. This suppression should be stronger for sources whose distribution extends to high redshifts, $z \gtrsim 10$, where $P \lesssim 0.5$ in the resonance region (see Fig. B.4).

4.3.1 Top-down scenarios

Top-down neutrinos are predicted by the models beyond standard model. They are produced in the decay/annihilation of topological defects or super heavy dark matter (SHDM). They have very high energy up to $\sim 10^{25}$ eV or above. The examples discussed here are unstable superheavy particles and topological defects, such as cosmic strings and cosmic necklaces.

4.3.1.1 Super heavy dark matter

In the ΛCDM model, we know the universe contains about 22.7 percent dark matter, whose fundamental properties are largely unknown . Considering that the standard model has a zoo of particles of 3 families, it is natural to imagine that the dark matter sector may consist of multiple particle species. There could have one kind of lone lived super heavy particle, called X-particle, with masses $m_X \leq 10^{16}$GeV. These particles take a tiny fraction ξ_X of total dark matter, i.e., $\Omega_{\rm SHDM} \equiv \xi_X \Omega_{\rm CDM}$ with $\xi_X \ll 1$. The life time τ_X of these objects can be as long as the age of the universe.If they decay or annihilate into partons between horizon and today, and then proceed to pions and neutrinos. Then the produced neutrinos have emissivity as [108],

$$\mathscr{L}_\nu^{\rm SHDM} = \frac{3 r_x \Omega_{\rm CDM}}{16\pi} \frac{\Theta[m_X - E(1+z)] e^{-E(1+z)/m_X}}{\ln[m_X/(1{\rm GeV})](1+{\rm z})^2} \frac{m_p H_0^2}{E^2 t_0 t_p}, \tag{4.24}$$

where $r_x \equiv \xi_X t_0/\tau_X$. Here we use the parameters are $m_X \sim 5\times10^{15}$ GeV, $r_X \sim 3\times10^{-7}$, and $\Omega_{CDM} = 0.227$. The model has a minimum redshift, corresponding to the time where most of the X particles have decayed (assuming that their lifetime is shorter than the age of the universe). We apply $z_{min} = 10$.

For SHDM whose emissivity is given by Fig. 4.24, we apply the propagation effects to the flux, and then get the results shown in Fig. 4.8. It is obviously to see the absorption dips around 10^{13}GeV.

4.3.1.2 Cosmic strings

Cosmic strings are predicted in field theory models whose vacuum manifold is not simply connected. Cosmic F- and D-strings of superstrings theory may also be produced in the brane inflation models in string theory [109]. If they exist, cosmic strings are stable relics formed in the very early universe, thus, they have incredibly high energy densities in their core. They are characterized by their tension, μ (mass per unit length) denoted in Planck units as a dimensionless parameter $G\mu$, where G is Newton's constant. The upper bound on cosmic string tension from CMB anisotropy measurements of WMAP and SPT is $G\mu \lesssim 1.7\times10^{-7}$ [110], and it has recently been updated by Planck to $G\mu \lesssim 1.5\times10^{-7}$ [111] which corresponds to a mass scale $m_s \lesssim \sqrt{\mu} \sim 5\times10^{15}$ GeV. This suggests that cosmic strings may be responsible for extremely high energy cosmic rays in the universe if they can emit particles efficiently.

Various mechanisms to produce particles from cosmic strings have been studied [112, 113, 114, 115, 116, 117, 118, 119], but only a few of them yield observable fluxes. For instance, observable UHE neutrinos can be achieved at the cusps of superconducting cosmic strings [117], which are short segments where the string velocity momentarily gets very close to the speed of light, and also at the cusps [118] and kinks [119] of cosmic strings and cosmic superstrings. Recently, Kaluza-Klein mode emission from cosmic superstring cusps has been shown to be an efficient radiation mechanism [120, 121], which can also lead to UHE neutrinos, and can be a potentially interesting signature of superstring theory.

In what follows, as an example, we discuss the case of neutrino emission from cosmic string cusps and kinks via heavy scalars (moduli) [117, 118, 119].

The neutrino emissivities from cusps [118] and kinks [119] (via modulus emission from cosmic strings) are respectively given by:

$$\mathscr{L}_\nu^{\rm cusp} = 9.5\times 10^{23}\frac{\alpha^2 (G\mu)^{1/2}\ln[(G\mu)^{1/2} m_p/m]}{p(1+z)^5}\frac{m_p}{E^2 t_p^{1/2} t(z)^{7/2}}, \quad (4.25)$$

$$\mathscr{L}_\nu^{\rm kink} = 1\times 10^{23}\frac{\alpha^2 (m_p/m)^{1/2}}{p(1+z)^5}\frac{m_p}{E^2 t(z)^4}, \quad (4.26)$$

where m_p is the Planck mass, t_p is the Planck time, $t(z)$ is the cosmic time given by the integral of Eq. (1.13) from epochs z to ∞, $p \lesssim 1$ is the string reconnection probability, $G\mu$ is the string tension, m is the modulus mass and α is the modulus coupling constant. In both models, the neutrino production has a redshift cutoff,

$$z_{\rm min}^{\rm str} \sim 122\left(\frac{G\mu}{10^{-17}}\right)^{2/7}\left(\frac{m}{10^4\ \rm GeV}\right)^{2/7}\left(\frac{E}{10^{11}\ \rm GeV}\right)^{-4/7}, \quad (4.27)$$

that corresponds to the minimum energy at which the hadronic cascade produces pions ($\varepsilon \sim 1$ GeV in the rest frame of the modulus), therefore the expressions above are valid for $z > z_{\rm min}^{\rm str}$. Eqs. (4.25) and (4.26) show that in both cases the emissivity is dominated by the emission at low redshifts, therefore the suppression of the diffuse flux due to absorption should be roughly determined by $P(E, z_{\rm min}^{\rm str})$. Here, we used the following parameter values: for kinks, $\alpha \sim 1$, $m \sim 10^4$ GeV, $G\mu \sim 10^{-17}$ and $p \sim 1$, corresponding to $z_{\rm min}^{\rm str} \simeq 2.3 - 122$ in the interval $E \simeq 10^{11} - 10^{14}$ GeV; for cusps, $\alpha \sim 2\times 10^7$, $m \sim 10^4$ GeV, $G\mu \sim 6\times 10^{-19}$ and $p \sim 1$, which give $z_{\rm min}^{\rm str} \simeq 1.0 - 54$ for $E \simeq 10^{11} - 10^{14}$ GeV.

Fig. 4.9 shows the diffuse flux from cosmic string kinks and cusps, with absorption effects, for the eight neutrino mass spectra (four for each hierarchy) listed in

Table 4.1. The flux has a sharp cutoff at about $E \sim 10^{10} - 10^{11}$ GeV. This is where the $z_{\rm min}^{\rm str} \sim z_\nu \sim 140$, so that the entire flux is emitted beyond the neutrino horizon z_ν, and is completely absorbed before reaching Earth.

In the spectrum, we observe the expected smearing of the dips into a single, broad suppression feature in the energy interval $E \sim 10^{11} - 10^{14}$ GeV. The suppression is overall stronger for kinks, due to the higher values of $z_{\rm min}^{\rm str}$. The dependence of the suppression on the neutrino mass spectrum is fairly weak: the spectrum shape is nearly identical for the all cases except for the one with the largest mass. This is due to a combination of the two smearing effects discussed above, due to redshift integration and to the thermal effects. Considering large values of $z_{\rm min}^{\rm str}$, thermal effects influence the position and depth of the dips more than the neutrino mass itself, at least for the strongly hierarchical neutrino spectra.

For superconducting string cusps, the neutrino emissivity is given by [117]

$$\mathscr{L}_\nu^{\rm sup} = 1.4 \times 10^{22} \frac{i_c f_B}{(1+z)^{5/2}} \frac{B m_p t_p^{1/2}}{E^2 t(z)^{5/2}}, \tag{4.28}$$

where $i_c \lesssim 1$ is the dimensionless string parameter characterizing the maximum current on the string, $f_B \sim 10^{-3}$ is the magnetic field filling factor, $B \sim 10^{-6}$ G is the magnetic field strength. In Fig. 4.10, we take $i_c \sim 0.1$. Like in the previous case, the emissivity is dominated by low redshifts, and has a lower redshift cutoff,

$$z_{\rm min}^{\rm sup} \sim 1.2\, i_c^{3/2} \left(\frac{G\mu}{6.7 \times 10^{-19}}\right)^{-3/4} \left(\frac{B}{10^{-6}\,{\rm G}}\right)^2 \left(\frac{E}{10^{-12}\,{\rm GeV}}\right)^{-3/2}, \tag{4.29}$$

furthermore, $z < z_{\rm max} \sim 5$, because in Ref. [117], it was assumed that the magnetic fields trace galaxies and clusters, and thus strings have no current at times prior to structure formation.

In Fig. 4.10, we plot the neutrino flux from the superconducting cosmic string cusps. It can be clearly seen that the absorption dips are too tiny to be observable.

Because the dominant redshift $z_{\rm min}^{\rm sup}$ is small, the optical depth is much less than unity, hence absorption in only at the level of 10% or less. Similarly to cosmic string cusp and kinks, the flux vanishes at about $E \sim 10^{11}$ GeV, when $z_{\rm min} \sim z_\nu$.

4.3.1.3 Cosmic necklaces

Cosmic necklaces are topological defects made up of strings and monopoles [122, 123]. They are predicted in field theory models, where the symmetry breaking sequence has the form $G \to H \times U(1) \to H \times Z_2$, where G is a semi-simple Lie group. As a result of the first symmetry breaking, monopoles form, and after the $U(1) \to Z_2$ breaking, each monopole is attached to two strings, each of which carries out half unit of flux as a result of the remaining Z_2 symmetry, hence the name cosmic necklace. As the monopoles and antimonopoles on loops of necklaces meet, they annihilate and produce heavy X-bosons related to the corresponding symmetry breaking scales of monopoles or strings. The bosons then decay via hadronic cascades into pions, that eventually decay producing numerous UHE neutrinos.

The neutrino emissivity from cosmic necklaces is given by [123] (see however Ref. [124])

$$\mathscr{L}_\nu^{\rm neck} = \frac{\Theta[m_X - E(1+z)]e^{-E(1+z)/m_X}}{2\ln[m_X/(1\mathrm{GeV})](1+\mathrm{z})^6} \frac{r}{E^2 m_p t_p t(z)^3}, \tag{4.30}$$

where m_X is the mass of the emitted heavy boson, and r is a parameter that depends on the monopole mass and the string tension. The model has a minimum redshift of neutrino emission, $z_{\rm min}^{\rm neck}$, which depends on the lifetime of the necklace. There is also a maximum energy cutoff, where $E' = E(1+z) \sim m_X$; the flux vanishes beyond this point. Here we take $m_X \sim 5 \times 10^{15}$ GeV, $r \sim 2 \times 10^{30}$ GeV^2 and $z_{\rm min}^{\rm neck} = 10$.

Fig. 4.9 shows the diffuse flux expected in this model, with absorption included for the eight mass configurations of Table 4.1. The flux suppression effect is similar to the case of cosmic string cusps and kinks: all these models share the common feature of a large redshift cutoff, $z_{\rm min} \gtrsim 10$, which controls the degree of absorption. We note, however, that the cutoff is parameter-dependent: smaller values of $z_{\rm min}$ (i.e., longer lifetime of the necklace) are allowed, and would result in weaker suppression. Even for large $z_{\rm min}^{\rm neck}$, the flux from cosmic necklaces may show no absorption effects, if $m_X \lesssim 10^{12}$ GeV, which means that the maximum neutrino energy cutoff is below the range of energy where absorption is relevant.

4.3.2 Bottom-up scenarios

In the bottom-up scenario, it is assumed that UHE neutrinos are generated from some cosmic accelerators via hadronic cascades. The possible sources are gamma ray bursts, active galactic nuclei, young supernova remnants, pulsars and so on. I will discuss some of them below.

4.3.2.1 Cosmogenic neutrinos

Cosmogenic neutrinos are produced during the propagation of ultra high energy cosmic rays (UHECR). The UHECRs with energies larger than threshold energy of $\sim 5 \cdot 10^{19}$eV interact with cosmic microwave background, produce pions via Δ^+ resonance.

$$p + \gamma \to \Delta^+ \to p/n + \pi^{0,\pm} \tag{4.31}$$

Then the π^0 decay into gamma rays, and the $\pi^\pm$ decay into three neutrinos and one position/electron. These produced neutrinos are called cosmogenic neutrinos. With this UHE neutrino source, I apply propagation effect to its energy spectrum. Here, the neutrino spectrum is taken from R. Engel et al. Since the Z^0 resonance occurs around energy of 10^{13}GeV, and the adopted spectrum goes down rapidly after that energy, the effect can not be observable in this case.

This is the same phenomenon as the origin of the observed GZK cutoff of the cosmic ray proton spectrum [25, 26]. The neutrino production is dominated by the Δ^+

resonance, which for CMB photons is realized at $E_p \gtrsim 5 \times 10^{10}$ GeV of proton energy. Through the resonance, pions are produced, and their decay chain generates muon and electron neutrinos. Since the parent protons are absorbed efficiently, we expect that the neutrino flux can be higher than the observed proton one. The cosmogenic neutrino spectrum $\phi(E')$ has been calculated in Refs. [125, 126].

The neutrino emissivity for cosmogenic neutrinos is given by

$$\mathscr{L}_\nu^{\mathrm{cosm}} = \mathscr{N}_0 (1+z)^{n-1} \phi(E') \tag{4.32}$$

where $\mathscr{N}_0$ and n characterize the source population in normalization and redshift evolution. The neutrino spectrum $\phi(E')$ has an exponential cutoff at the maximum proton acceleration energy E_{max}.

Under the assumption that UHE protons are produced by stellar or galactic-size objects, the evolution of the source should have $n \simeq 3-4$, with a maximum redshift $z_{\mathrm{max}} \simeq 7-10$. Here we take $n = 3$ and $z_{\mathrm{max}} = 10$, and use the single source spectrum from Ref. [125], which has maximum acceleration energy $E_{\mathrm{max}} \sim 10^{11}$ GeV. The resulting diffuse flux is shown in Fig. 4.7, and is practically the same with and without resonant absorption. Neutrino-neutrino scattering effects are completely negligible, since the sources are at low redshifts, $z_{\mathrm{max}} \lesssim 10$, where the optical depth is very small, $\tau \ll 1$. Besides, even a modest absorption dip would probably be unobservable because the flux declines sharply with energy above E_{max}, and is greatly suppressed in the part of the spectrum relevant for absorption, $E \sim 10^{12} - 10^{13}$ GeV.

4.3.2.2 Gamma ray bursts and Active galactic nuclei

Gamma ray bursts (GRB) and Active Galactic Nuclei (AGN) are sources of high energy gamma rays, and candidate sources of UHE neutrinos. The UHE neutrinos are produced via hadronic cascades in the interactions of high energy protons with the intense photon background in the source. The redshift evolution of these sources is believed to be stronger than the star formation rate history. Specifically, their comoving rate can be written as:

$$\frac{dN}{dz} = A \cdot \eta_{SFR}(z)(1+z)^{\beta} \, \frac{dV_c}{dz} \frac{1}{1+z}, \tag{4.33}$$

where V_c is the comoving volume, A is a normalization constant, and $\beta \simeq 1.5$ for GRB [127] and $\beta \simeq 2$ for AGN [128]. Here η_{SFR} is star formation rate density [129]:

$$\eta_{SFR}(z) = \eta_0 \left[(1+z)^a + \left(\frac{1+z}{B} \right)^b + \left(\frac{1+z}{C} \right)^c \right]^{-0.1} . \tag{4.34}$$

with $\eta_0 = 0.02\ M_\odot\ \mathrm{yr}^{-1}\mathrm{Mpc}^{-3}$ ($M_\odot$ is the mass of the Sun), $a = -34,\ b = 3,\ c = 3.5,\ B = 5000,\ C = 9$ [129].

The neutrino spectra follows a power law, $\phi(E') \propto E'^{-2}$, with a lower and upper energy cutoffs. Therefore the neutrino emissivity is given by,

$$\mathscr{L}_\nu^{\mathrm{GRB}} = j_0 \frac{dN}{dz} \left(\frac{E(1+z)}{E_{\max}} \right)^{-2} \Theta[E(1+z) - E_{\min}]\ \Theta[E_{\max} - E(1+z)] \, . \tag{4.35}$$

Here we use the normalization $j_0 \simeq 10^{-49}$GeV cm/s, $E_{\min} \simeq 10^9$GeV, and $E_{\max} \simeq 10^{12}$GeV [105].

Similar to cosmogenic neutrinos, our results show that absorption is negligible for GRB and AGN neutrinos, since their flux is dominated by small redshifts of order a few, and is cut off below the energy range of interest for absorption.

4.4 Discussion and conclusion

In this work, we have studied the absorption of cosmic UHE neutrinos propagating through the CνB, including the effects of the thermal distribution of the background relic neutrinos. The thermal effects have been fully calculated, with three active neutrino species, and realistic neutrino mass spectra and mixings. The resonant production of Z^0 through annihilation results in absorption dips in UHE neutrino spectrum. The thermal effects cause the resonance to be realized for an interval of the beam neutrino energy, depending on the scattering angle and the temperature of the background. That is, with the consideration of the thermal effects, the shape and position of the absorption dips will both change.

The suppression of the UHE neutrino spectrum changes from sharp to wide as the thermal effects become important. This transition occurs when $\bar{p}(1+z) \sim m_{\min}$, with $m_{\min}$ being the smallest of the three neutrino masses. In terms of cosmic time, this corresponds to redshift $1+z_{\text{th}} \sim 16\ m_{\min}/(10^{-2}\ \text{eV})$. For $m_{\min} \lesssim 10^{-4}$ eV, thermal effects are already substantial, for the lightest neutrino species, at the present time. However, this does not translate in a flux suppression, due the insufficient optical depth. We find that the optical depth is substantial, $\tau \gtrsim 1$, for neutrino sources at $z \gtrsim 10$ [Eq. (4.16)].

The fact that $z \gtrsim 10$ is required to have significant suppression has two important consequences. First, neutrinos from stellar and galactic sources (e.g., cosmogenic neutrinos and neutrinos from AGN and GRBs), which extend up to $z \sim 5$ or so, have negligible absorption, and therefore their spectrum is a direct representation of the physics of the sources. Secondly, an observable spectrum distortion should have at most two dips, not three. This is because, at $z \gtrsim 10$, the mass difference between m_1 and m_2 is comparable with the average neutrino energy, i.e., $m_2 - m_1 \sim 10^{-2}\ \text{eV} \simeq \bar{p}$, therefore the scattering off ν_1 and ν_2 causes a single dip instead of two separate ones.

A further smearing of the suppression dips is produced by integrating over the spatial distribution of the sources. We worked out specific examples of diffuse UHE neutrino fluxes, with a focus on neutrinos from top down mechanisms, for which the sources extend beyond $z \sim 10$, and therefore a strong absorption is expected. The cases considered were cosmic string kinks and cusps, super-heavy dark matter, cosmic necklaces and superconducting strings. In all these models the flux is dominated by the contribution of sources closest to us, i.e., at the lowest redshift, $z_{\min}$, which, in general, depends on energy. Therefore, in first approximation the flux suppression is described by $P(E, z_{\min})$, with $P(E, z)$ being the probability of transmission for a neutrino of energy E (at Earth) and production epoch z [Eq. (4.19)].

We have found that, indeed, for sources with $z_{\min} \gtrsim 10$, the diffuse flux is suppressed strongly, up to an order of magnitude or even more, in some cases. A broad suppression valley is localized between 10^{12} and 10^{14} GeV; its shape and extent in energy depends on the details of the model and on the neutrino mass spectrum. However, the dependence on the neutrino mass spectrum, and especially on the mass hierarchy, is relatively weak.

This generality is a result of the thermal effects, which, at least for the hierarchical mass spectra, dominate over the neutrino mass effect, and tend to make the suppression mass-independent. This has an immediate implication: the energy interval $10^{12} - 10^{13}$ GeV is potentially the worst place to look to discover UHE neutrinos. This might have to be taken into account in the design of UHE neutrino detectors. We note that SKA (which is not optimized for neutrino detection) has maximum sensitivity exactly in this range (see Fig. 4.7), therefore it might find itself in a position of disadvantage compared to other probes with different energy sensitivity.

Without being too specific, here we assume that UHE neutrino detectors can identify, at least roughly, a suppression in the neutrino spectrum. In the worst case of energy-blind detectors, some sensitivity can be gained by comparing the fluxes measurements or upper limits from different techniques probing different parts of the neutrino spectrum. For a single detector, a suppression may be defined only relative to a model of reference.

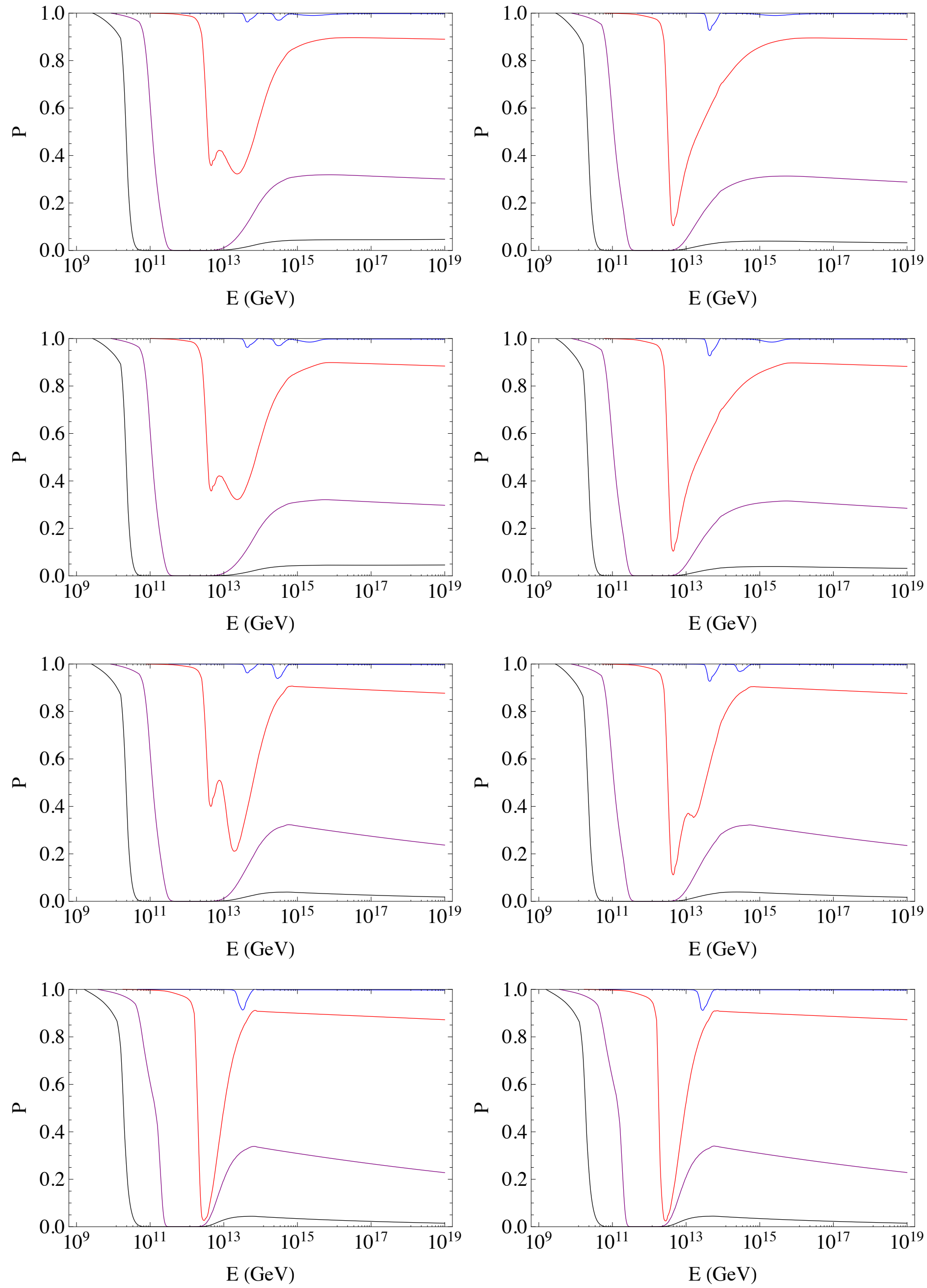

Figure 4.6: Flavor-averaged survival probability given by Eq. (4.19), as a function of the observed neutrino energy, for a source located at $z = 1$ (blue), 20 (red), 100 (purple), 200 (black) (curves from top to bottom in each figure). Left (right) column is for normal (inverted) hierarchy. Figures from top to bottom correspond to the lightest neutrino mass m_1 (m_3) in eV: 10^{-5}, 10^{-3}, 2×10^{-2}, 8×10^{-2}.

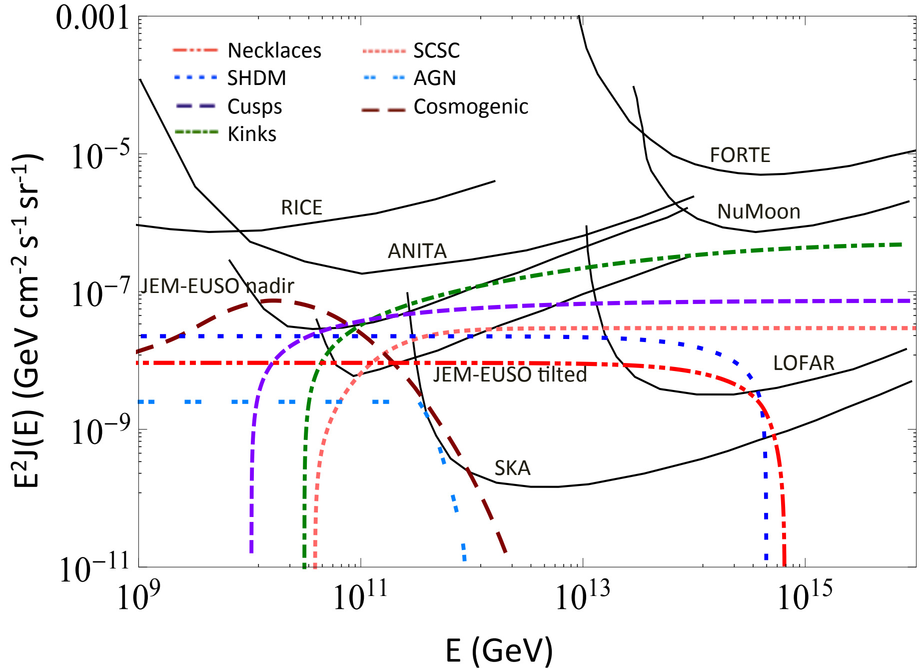

Figure 4.7: Solid (black) curves: existing upper bounds on the UHE neutrino flux from RICE, ANITA, FORTE, NuMoon, and expected sensitivities at JEM-EUSO (nadir and tilted modes), LOFAR and SKA. Non-solid (color) curves: UHE neutrino fluxes from cosmic string cusps, cosmic string kinks, superconducting cosmic string cusps (SCSC), cosmic necklaces, superheavy dark matter (SHDM), cosmogenic neutrinos and active galactic nuclei (AGN) (see the legend in the figure).

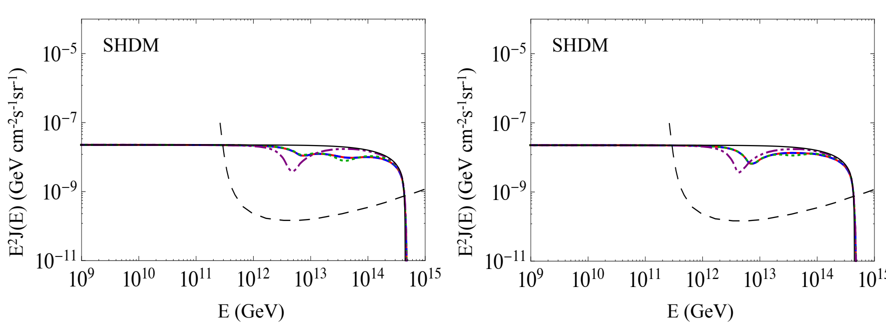

Figure 4.8: Neutrino fluxes from super heavy dark matter with propagation effects, as a function of the energy. Left (right) one is for normal (inverted) hierarchy, $m_1(m_3)=10^{-5}$, 10^{-3}, $2\cdot10^{-2}$, $8\cdot10^{-2}$ (As shown in brown, blue, green, purple)

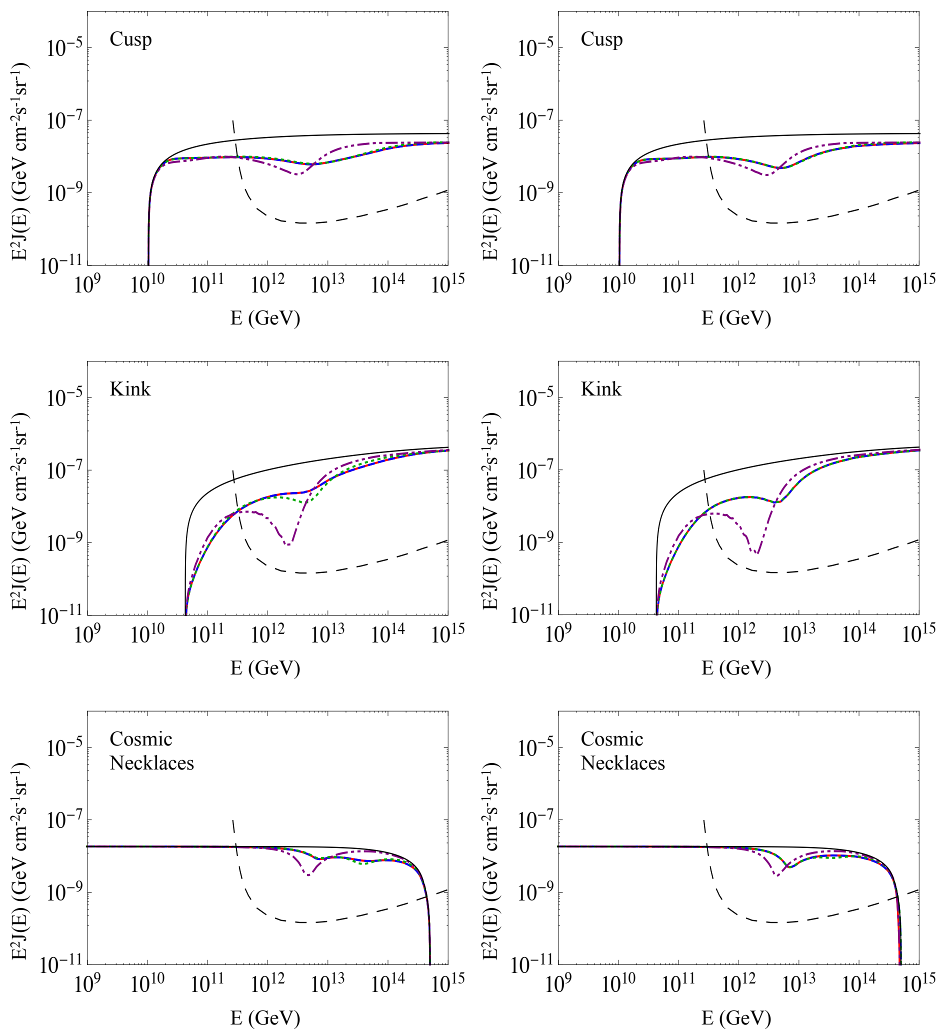

Figure 4.9: Neutrino fluxes from top down models. From top to bottom panels: cosmic string cusps, cosmic string kinks, cosmic necklacesas a function of the energy, for the masses as in fig. B.4. Left (right) column is for normal (inverted) hierarchy, $m_1(m_3)$=10^{-5}, 10^{-3}, $2\cdot10^{-2}$, $8\cdot10^{-2}$ (As shown in brown, blue, green, purple)

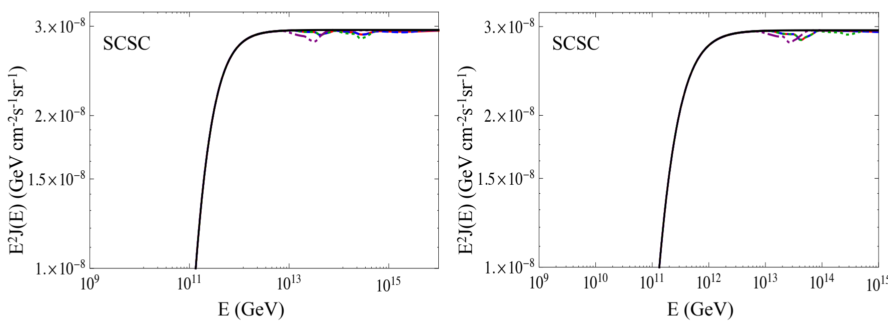

Figure 4.10: Expected neutrino flux from superconducting cosmic string cusps (SCSC) as a function of energy, for the same neutrino mass values (and color coding) as in Fig. 4.9. Left (right) column is for normal (inverted) hierarchy.

If UHE neutrinos are detected, and the data are compatible with a suppression due to neutrino absorption, what can be learned from them? Considering that the suppression bears only little dependence on the neutrino mass and mixing pattern, the main information will be on the physics of the sources. In particular, the observation of neutrino absorption will indicate, beyond doubt, a population of sources extending to $z \gtrsim 10$, earlier than the time of formation of stars and galaxies. Therefore, this might be a way to discover, or further substantiate, the existence of cosmological relics like superheavy dark matter, cosmic strings or necklaces. The detailed shape of the suppression dip (if available) would in principle allow to reconstruct $z_{\rm min}$ as a function of energy since the distortion is roughly determined by $P(E, z_{\rm min})$. This can help to discriminate between different source models, if combined with other elements like the presence of a minimum energy cutoff (favoring cosmic string cusps and kinks) or a high energy flux termination (which would favor cosmic necklaces and superheavy dark matter).

Spectral distortions due to resonant absorption are, at least in principle, an interesting probe of the CνB at relatively recent cosmological times, $z \sim 10-100$, that are out of the reach of both cosmological surveys [like those of Large Scale Structure ($z \lesssim 10$), and of the CMB ($z \sim 1100$), etc.] and direct detections of the CνB (e.g., by zero-threshold nuclear decay [131], testing $z = 0$). In particular, an observed absorption pattern could help to constrain, or even reveal, several exotic effects:

(i) Non standard neutrino number density. An increased population of active neutrinos would result in stronger absorption dips. For example, we could consider an increase in number density by a factor $4/3$, corresponding to an effective number of cosmological relativistic degrees of freedom $N_{\rm eff} = 4$, which has recently attracted some interests (see e.g., [132, 133]). This increase would change the optical depth by the same amount, and shorten the neutrino horizon down to $z \sim 120$. A depletion of the neutrino pop-

ulation at late times is also possible, for example due to neutrino decay into a sterile neutrino or very weakly interacting species (e.g., [134]). This would suppress the absorption and extend the neutrino horizon.
(ii) Non-standard neutrino spectrum. Currently, there is no direct information on the CνB spectrum, and indirect constraints are limited. Deviations from a thermal spectrum have been suggested, e.g., as a consequence of active-sterile neutrino conversion (e.g., [135]). They would influence the shape of the absorption dips, which could be narrower for a narrower neutrino spectrum or if the spectrum is much colder than expected, so to make most of the neutrinos non-relativistic at the epochs of interest.
(iii) Neutrino asymmetry, anomalous flavor composition, non-standard neutrino interactions, and other exotica. Our results could be generalized to consider a broader range of situations, including a neutrino population which is not flavor and CP-symmetric. Although these possibilities are interesting, to study them with UHE neutrino absorption may be complicated by degeneracies between the physics of the CνB and the physics of the sources: for example, there is a degeneracy between the neutrino number density and the redshift distribution of the sources such that they both affect the depth of the spectral dips in a similar way.

If nothing else, it is important to accurately model the absorption dips to correctly interpret observations, and in particular to distinguish the effect of resonant $\nu - \bar{\nu}$ annihilation from spectral features of different nature, e.g., due to the overlap of two fluxes of different origin (bimodal spectrum), that could roughly mimic an absorption dip.

Although some of the effects described here require high precision and statistics, we can not underestimate the potential of this field to open a completely new way to explore the sky and learn about neutrinos.

REFERENCES

[1] F. Reines and C. L. Cowan, Nature **178**, 446 (1956).

[2] M. Goldhaber, L. Grodzins and A. W. Sunyar, Phys. Rev. **109**, 1015 (1958).

[3] G. Danby, J. M. Gaillard, K. A. Goulianos, L. M. Lederman, N. B. Mistry, M. Schwartz and J. Steinberger, Phys. Rev. Lett. **9**, 36 (1962).

[4] M. L. Perl, G. S. Abrams, A. Boyarski, M. Breidenbach, D. Briggs, F. Bulos, W. Chinowsky and J. T. Dakin *et al.*, Phys. Rev. Lett. **35**, 1489 (1975).

[5] Q. R. Ahmad *et al.* [SNO Collaboration], Phys. Rev. Lett. **87**, 071301 (2001) [nucl-ex/0106015].

[6] F. P. An *et al.* [DAYA-BAY Collaboration], Phys. Rev. Lett. **108**, 171803 (2012) [arXiv:1203.1669 [hep-ex]].

[7] J. K. Ahn *et al.* [RENO Collaboration], Phys. Rev. Lett. **108**, 191802 (2012) [arXiv:1204.0626 [hep-ex]].

[8] Y. Abe *et al.* [DOUBLE-CHOOZ Collaboration], Phys. Rev. Lett. **108**, 131801 (2012) [arXiv:1112.6353 [hep-ex]].

[9] K. Abe *et al.* [T2K Collaboration], Phys. Rev. Lett. **107**, 041801 (2011) [arXiv:1106.2822 [hep-ex]].

[10] M. G. Aartsen *et al.* [IceCube Collaboration], Phys. Rev. Lett. **111**, 021103 (2013) [arXiv:1304.5356 [astro-ph.HE]].

[11] G. Drexlin, V. Hannen, S. Mertens and C. Weinheimer, Adv. High Energy Phys. **2013**, 293986 (2013) [arXiv:1307.0101 [physics.ins-det]].

[12] G. L. Fogli, E. Lisi, A. Marrone, D. Montanino, A. Palazzo and A. M. Rotunno, Phys. Rev. D **86**, 013012 (2012) [arXiv:1205.5254 [hep-ph]].

[13] B. Pontecorvo, *Mesonium and anti-mesonium*, Sov. Phys. JETP **6** (1957) 429 [Zh. Eksp. Teor. Fiz. **33** (1957) 549].

[14] B. Pontecorvo, *Neutrino Experiments and the Problem of Conservation of Leptonic Charge*, Sov. Phys. JETP **26** (1968) 984 [Zh. Eksp. Teor. Fiz. **53** (1967) 1717].

[15] Z. Maki, M. Nakagawa and S. Sakata, *Remarks on the unified model of elementary particles*, Prog. Theor. Phys. **28** (1962) 870.

[16] K. Nakamura *et al.* [Particle Data Group Collaboration], J. Phys. G **37**, 075021 (2010).

[17] S. Abe *et al.* [KamLAND Collaboration], Phys. Rev. Lett. **100**, 221803 (2008) [arXiv:0801.4589 [hep-ex]].

[18] E. Komatsu *et al.* [WMAP Collaboration], Astrophys. J. Suppl. **192**, 18 (2011) [arXiv:1001.4538 [astro-ph.CO]].

[19] Y. Suzuki, Int. J. Mod. Phys. A **15S1**, 201 (2000) [eConf C **990809**, 201 (2000)].

[20] L. C. Stonehill, J. A. Formaggio and R. G. H. Robertson, Phys. Rev. C **69**, 015801 (2004) [hep-ph/0309266].

[21] L. Ludhova and S. Zavatarelli, arXiv:1310.3961 [hep-ex].

[22] M. Wurm, F. von Feilitzsch, M. Goeger-Neff, K. A. Hochmuth, T. M. Undagoitia, L. Oberauer and W. Potzel, Phys. Rev. D **75**, 023007 (2007) [astro-ph/0701305].

[23] J. G. Keehn and C. Lunardini, Phys. Rev. D **85**, 043011 (2012) [arXiv:1012.1274 [astro-ph.CO]].

[24] G. Battistoni, A. Ferrari, T. Montaruli and P. R. Sala, Astropart. Phys. **23**, 526 (2005).

[25] K. Greisen, Phys. Rev. Lett. **16**, 748 (1966).

[26] G. T. Zatsepin and V. A. Kuzmin, JETP Lett. **4**, 78 (1966) [Pisma Zh. Eksp. Teor. Fiz. **4**, 114 (1966)].

[27] M. Ikeda *et al.* [Super-Kamiokande Collaboration], Astrophys. J. **669**, 519 (2007) [arXiv:0706.2283 [astro-ph]].

[28] S. W. Barwick,

[29] C. Rubbia, CERN-EP-INT-77-08.

[30] G. Karagiorgi, arXiv:1304.2083 [physics.ins-det].

[31] C. Lunardini, arXiv:1007.3252 [astro-ph.CO].

[32] P. W. Gorham, C. L. Hebert, K. M. Liewer, C. J. Naudet, D. Saltzberg and D. Williams, Phys. Rev. Lett. **93**, 041101 (2004) [astro-ph/0310232].

[33] S. Buitink, J. Bacelar, R. Braun, G. de Bruyn, H. Falcke, O. Scholten, K. Singh and B. Stappers *et al.*, arXiv:0808.1878 [astro-ph].

[34] T. R. Jaeger, R. L. Mutel and K. G. Gayley, Astropart. Phys. **34**, 293 (2010) [arXiv:0910.5949 [astro-ph.IM]].

[35] N. G. Lehtinen, P. W. Gorham, A. R. Jacobson and R. A. Roussel-Dupre, Phys. Rev. D **69**, 013008 (2004) [astro-ph/0309656].

[36] A. Bean [RICE Collaboration], AIP Conf. Proc. **870**, 212 (2006).

[37] S. W. Barwick *et al.* [ANITA Collaboration], Phys. Rev. Lett. **96**, 171101 (2006) [astro-ph/0512265].

[38] T. Ebisuzaki, Y. Uehara, H. Ohmori, K. Kawai, Y. Kawasaki, M. Sato, Y. Takizawa and M. E. Bertaina *et al.*, Nucl. Phys. Proc. Suppl. **175-176**, 237 (2008).

[39] Y. Takahashi [JEM-EUSO Collaboration], arXiv:0910.4187 [astro-ph.HE].

[40] O. Scholten, J. Bacelar, R. Braun, A. G. de Bruyn, H. Falcke, B. Stappers and R. G. Strom, Astropart. Phys. **26**, 219 (2006) [astro-ph/0508580].

[41] C. W. James and R. J. Protheroe, Astropart. Phys. **30**, 318 (2009) [arXiv:0802.3562 [astro-ph]].

[42] C. Giunti and C. W. Kim, Oxford, UK: Univ. Pr. (2007) 710 p

[43] A. Burrows, Rev. Mod. Phys. **85**, no. 1 (2013) [arXiv:1210.4921 [astro-ph.SR]].

[44] C. M. Amaya and M. Biassoni, Astropart. Phys. **36**, 151 (2012) [arXiv:1110.3536 [astro-ph.HE]].

[45] H. -T. Janka, F. Hanke, L. Huedepohl, A. Marek, B. Mueller and M. Obergaulinger, PTEP **2012**, 01A309 (2012) [arXiv:1211.1378 [astro-ph.SR]].

[46] E. E. Salpeter, Astrophys. J. **121**, 161 (1955).

[47] S. A. Colgate and R. H. White, Astrophys. J. **143**, 626 (1966).

[48] A. M. Hopkins and J. F. Beacom, Astrophys. J. **651**, 142 (2006) [astro-ph/0601463].

[49] S. Horiuchi, J. F. Beacom, C. S. Kochanek, J. L. Prieto, K. Z. Stanek and T. A. Thompson, Astrophys. J. **738**, 154 (2011) [arXiv:1102.1977 [astro-ph.CO]].

[50] T. Fischer, S. C. Whitehouse, A. Mezzacappa, F. -K. Thielemann and M. Liebendorfer, Astron. Astrophys. **517**, A80 (2010) [arXiv:0908.1871 [astro-ph.HE]].

[51] S. E. Woosley, A. Heger and T. A. Weaver, Rev. Mod. Phys. **74**, 1015 (2002).

[52] T. Totani, K. Sato, H. E. Dalhed and J. R. Wilson, Astrophys. J. **496**, 216 (1998) [astro-ph/9710203].

[53] T. A. Thompson, A. Burrows and P. A. Pinto, Astrophys. J. **592**, 434 (2003) [astro-ph/0211194].

[54] G. G. Raffelt, M. T. .Keil, R. Buras, H. -T. Janka and M. Rampp, astro-ph/0303226.

[55] L. Wolfenstein, Phys. Rev. D **17**, 2369 (1978).

[56] S. P. Mikheev and A. Y. .Smirnov, Sov. J. Nucl. Phys. **42**, 913 (1985) [Yad. Fiz. **42**, 1441 (1985)].

[57] H. Duan, G. M. Fuller and Y. -Z. Qian, Ann. Rev. Nucl. Part. Sci. **60**, 569 (2010) [arXiv:1001.2799 [hep-ph]].

[58] Y. -Z. Qian, G. M. Fuller, G. J. Mathews, R. Mayle, J. R. Wilson and S. E. Woosley, Phys. Rev. Lett. **71**, 1965 (1993).

[59] D. Notzold and G. Raffelt, Nucl. Phys. B **307**, 924 (1988).

[60] C. Lunardini and I. Tamborra, JCAP **1207**, 012 (2012) [arXiv:1205.6292 [astro-ph.SR]].

[61] H. Duan, G. M. Fuller, JCarlson and Y. -Z. Qian, Phys. Rev. D **74**, 105014 (2006) [astro-ph/0606616].

[62] A. Mirizzi, Nucl. Phys. Proc. Suppl. **229-232**, 320 (2012).

[63] G. L. Fogli, E. Lisi, A. Marrone, A. Palazzo and A. M. Rotunno, Phys. Rev. D **84**, 053007 (2011) [arXiv:1106.6028 [hep-ph]].

[64] A. Friedland, Phys. Rev. Lett. **104**, 191102 (2010) [arXiv:1001.0996 [hep-ph]].

[65] G. L. Fogli, E. Lisi, A. Marrone and A. Mirizzi, JCAP **0712**, 010 (2007) [arXiv:0707.1998 [hep-ph]].

[66] B. Dasgupta, A. Dighe, G. G. Raffelt and A. Y. .Smirnov, Phys. Rev. Lett. **103**, 051105 (2009) [arXiv:0904.3542 [hep-ph]].

[67] A. Y. .Smirnov, Phys. Scripta T **121**, 57 (2005) [hep-ph/0412391].

[68] A. S. Dighe and A. Y. .Smirnov, Phys. Rev. D **62**, 033007 (2000) [hep-ph/9907423].

[69] E. K. Akhmedov, C. Lunardini and A. Y. .Smirnov, Nucl. Phys. B **643**, 339 (2002) [hep-ph/0204091].

[70] C. Lunardini and A. Y. .Smirnov, JCAP **0306**, 009 (2003) [hep-ph/0302033].

[71] K. Takahashi, K. Sato, A. Burrows and T. A. Thompson, Phys. Rev. D **68**, 113009 (2003) [hep-ph/0306056].

[72] C. Lunardini, hep-ph/0307257.

[73] C. Lunardini, Astropart. Phys. **26**, 190 (2006) [astro-ph/0509233].

[74] C. Lunardini and A. Y. .Smirnov, Phys. Rev. D **63**, 073009 (2001) [hep-ph/0009356].

[75] B. Jegerlehner, F. Neubig and G. Raffelt, Phys. Rev. D **54**, 1194 (1996) [astro-ph/9601111].

[76] M. T. Botticella, M. Riello, E. Cappellaro, S. Benetti, G. Altavilla, A. Pastorello, M. Turatto and L. Greggio *et al.*, Astron. Astrophys. **479**, 49 (2008) [arXiv:0710.3763 [astro-ph]].

[77] E. Cappellaro, R. Evans and M. Turatto, Astron. Astrophys. **351**, 459 (1999) [astro-ph/9904225].

[78] W. Li, R. Chornock, J. Leaman, A. V. Filippenko, D. Poznanski, X. Wang, M. Ganeshalingam and F. Mannucci, arXiv:1006.4613 [astro-ph.SR].

[79] J. Melinder, T. Dahlen, L. M. Trinchant, G. Ostlin, S. Mattila, J. Sollerman, C. Fransson and M. Hayes *et al.*, arXiv:1206.6897 [astro-ph.CO].

[80] O. Graur, D. Poznanski, D. Maoz, N. Yasuda, T. Totani, M. Fukugita, A. V. Filippenko and R. J. Foley *et al.*, arXiv:1102.0005 [astro-ph.CO].

[81] G. Bazin, N. Palanque-Delabrouille, J. Rich, V. Ruhlmann-Kleider, E. Aubourg, L. L. Guillou, P. Astier and C. Balland *et al.*, arXiv:0904.1066 [astro-ph.CO].

[82] T. Dahlen, L. -G. Strolger, A. G. Riess, B. Mobasher, R. -R. Chary, C. J. Conselice, H. C. Ferguson and A. S. Fruchter *et al.*, Astrophys. J. **613**, 189 (2004) [astro-ph/0406547].

[83] S. J. Smartt, J. J. Eldridge, R. M. Crockett and J. R. Maund, arXiv:0809.0403 [astro-ph].

[84] K. Bays [Super-Kamiokande Collaboration], J. Phys. Conf. Ser. **375**, 042037 (2012).

[85] A. Kibayashi [Super-Kamiokande Collaboration], arXiv:0909.5528 [astro-ph.IM].

[86] M. Malek *et al.* [Super-Kamiokande Collaboration], Phys. Rev. Lett. **90**, 061101 (2003) [hep-ex/0209028].

[87] F. Vissani and G. Pagliaroli, Astron. Astrophys. **528**, L1 (2011) [arXiv:1102.0447 [astro-ph.HE]].

[88] E. Kolbe, K. Langanke, G. Martinez-Pinedo and P. Vogel, J. Phys. G **29**, 2569 (2003) [nucl-th/0311022].

[89] K. Sumiyoshi, S. Yamada and H. Suzuki, Astrophys. J. **667**, 382 (2007) [arXiv:0706.3762 [astro-ph]].

[90] T. W. Baumgarte, S. A. Teukolsky, S. L. Shapiro, H. T. Janka and W. Keil, Astrophys. J. **468**, 823 (1996).

[91] W. -Q. Zhang, S. E. Woosley and A. Heger, [astro-ph/0701083].

[92] E. O'Connor and C. D. Ott, Astrophys. J. **730**, 70 (2011) [arXiv:1010.5550 [astro-ph.HE]].

[93] M. D. Kistler, H. Yuksel, S. 'i. Ando, J. F. Beacom and Y. Suzuki, Phys. Rev. D **83**, 123008 (2011) [arXiv:0810.1959 [astro-ph]].

[94] M. Liebendoerfer, O. E. B. Messer, A. Mezzacappa, S. W. Bruenn, C. Y. Cardall and F. K. Thielemann, Astrophys. J. Suppl. **150**, 263 (2004) [astro-ph/0207036].

[95] K. Sumiyoshi, S. Yamada, H. Suzuki and S. Chiba, Phys. Rev. Lett. **97**, 091101 (2006) [astro-ph/0608509].

[96] S. 'i. Ando, J. F. Beacom and H. Yuksel, Phys. Rev. Lett. **95**, 171101 (2005) [astro-ph/0503321].

[97] K. 'i. Nakazato, K. Sumiyoshi, H. Suzuki and S. Yamada, Phys. Rev. D **78**, 083014 (2008) [Erratum-ibid. D **79**, 069901 (2009)] [arXiv:0810.3734 [astro-ph]].

[98] J. M. Lattimer and F. D. Swesty, Nucl. Phys. A **535**, 331 (1991).

[99] H. Shen, H. Toki, K. Oyamatsu and K. Sumiyoshi, Nucl. Phys. A **637**, 435 (1998) [nucl-th/9805035].

[100] S. M. Couch, Astrophys. J. **765**, 29 (2013) [arXiv:1206.4724 [astro-ph.HE]].

[101] K. Zuber, Boca Raton: USA: CRC Pr. (2012) 448p

[102] V. S. Berezinsky, Nucl. Phys. B **380**, 478 (1992).

[103] T. J. Weiler, Phys. Rev. Lett. **49**, 234 (1982).

[104] E. Roulet, Phys. Rev. D **47**, 5247 (1993).

[105] B. Eberle, A. Ringwald, L. Song and T. J. Weiler, Phys. Rev. D **70**, 023007 (2004) [hep-ph/0401203].

[106] J. C. D'Olivo, L. Nellen, S. Sahu and V. Van Elewyck, Astropart. Phys. **25**, 47 (2006) [astro-ph/0507333].

[107] G. Barenboim, O. Mena Requejo and C. Quigg, Phys. Rev. D **71**, 083002 (2005) [hep-ph/0412122].

[108] V. Berezinsky, M. Kachelriess and A. Vilenkin, Phys. Rev. Lett. **79**, 4302 (1997) [astro-ph/9708217].

[109] S. Sarangi and S. H. H. Tye, Phys. Lett. B **536**, 185 (2002) [hep-th/0204074].

[110] C. Dvorkin, M. Wyman and W. Hu, Phys. Rev. D **84**, 123519 (2011) [arXiv:1109.4947 [astro-ph.CO]].

[111] P. A. R. Ade *et al.* [Planck Collaboration], arXiv:1303.5085 [astro-ph.CO].

[112] C. T. Hill, D. N. Schramm and T. P. Walker, Phys. Rev. D **36**, 1007 (1987).

[113] P. Bhattacharjee, Phys. Rev. D **40**, 3968 (1989).

[114] J. H. MacGibbon and R. H. Brandenberger, Nucl. Phys. B **331**, 153 (1990).

[115] R. Brandenberger, Y. -F. Cai, W. Xue and X. -m. Zhang, arXiv:0901.3474 [hep-ph].

[116] T. Vachaspati, Phys. Rev. D **81**, 043531 (2010) [arXiv:0911.2655 [astro-ph.CO]].

[117] V. Berezinsky, K. D. Olum, E. Sabancilar and A. Vilenkin, Phys. Rev. D **80**, 023014 (2009) [arXiv:0901.0527 [astro-ph.HE]].

[118] V. Berezinsky, E. Sabancilar and A. Vilenkin, Phys. Rev. D **84**, 085006 (2011) [arXiv:1108.2509 [astro-ph.CO]].

[119] C. Lunardini and E. Sabancilar, Phys. Rev. D **86**, 085008 (2012) [arXiv:1206.2924 [astro-ph.CO]].

[120] J. -F. Dufaux, Phys. Rev. Lett. **109**, 011601 (2012) [arXiv:1109.5121 [hep-th]].

[121] J. -F. Dufaux, JCAP **1209**, 022 (2012) [arXiv:1201.4850 [hep-th]].

[122] V. Berezinsky, X. Martin and A. Vilenkin, INFN-TH-97-03.

[123] V. Berezinsky and A. Vilenkin, Phys. Rev. Lett. **79**, 5202 (1997) [astro-ph/9704257].

[124] J. J. Blanco-Pillado and K. D. Olum, JCAP **1005**, 014 (2010) [arXiv:0707.3460 [astro-ph]].

[125] R. Engel, D. Seckel and T. Stanev, Phys. Rev. D **64**, 093010 (2001) [astro-ph/0101216].

[126] O. E. Kalashev, V. A. Kuzmin, D. V. Semikoz and G. Sigl, Phys. Rev. D **66**, 063004 (2002) [hep-ph/0205050].

[127] B. E. Robertson and R. S. Ellis, Astrophys. J. **744**, 95 (2012) [arXiv:1109.0990 [astro-ph.CO]].

[128] G. Hasinger, T. Miyaji and M. Schmidt, Astron. Astrophys. **441**, 417 (2005) [astro-ph/0506118].

[129] H. Yuksel, M. D. Kistler, J. F. Beacom and A. M. Hopkins, Astrophys. J. **683**, L5 (2008) [arXiv:0804.4008 [astro-ph]].

[130] S. Weinberg, Phys. Rev. **128**, 1457 (1962).

[131] S. Weinberg, Phys. Rev. **128**, 1457 (1962).

[132] G. Hinshaw *et al.* [WMAP Collaboration], Astrophys. J. Suppl. **208**, 19 (2013) [arXiv:1212.5226 [astro-ph.CO]].

[133] P. A. R. Ade *et al.* [Planck Collaboration], arXiv:1303.5076 [astro-ph.CO].

[134] J. F. Beacom, N. F. Bell and S. Dodelson, Phys. Rev. Lett. **93**, 121302 (2004) [astro-ph/0404585].

[135] C. T. Kishimoto, G. M. Fuller and C. J. Smith, Phys. Rev. Lett. **97**, 141301 (2006) [astro-ph/0607403].

[136] J. Beringer *et al.* [Particle Data Group Collaboration], Phys. Rev. D **86**, 010001 (2012).

[137] L. Verde, Lect. Notes Phys. **800**, 147 (2010) [arXiv:0911.3105 [astro-ph.CO]].

[138] W. H. Press, S. A. Teukolsky, W. T. Vetterling and B. P. Flannery, ISBN-9780521430647.

APPENDIX A

Maximum likelihood analysis

A.1 Maximum likelihood analysis

In the diffuse supernova neutrino flux calculation, we employ the maximum likelihood method to analyze the supernova rate and neutrino spectrum from SN1987A data. Here we follow the derivation and notation of Ref. [136]. Suppose we have the information of data D and model M. The probability of the data given the model is called the likelihood, which is expressed as P($D|M$), a conditional probability, and read as "P of D given M":

$$P(D|M) = \frac{P(D \cap M)}{P(M)} \tag{A.1}$$

Here, $P(D \cap M)$ indicates the probability that D and M both occur. Given the fact that $D \cap M$ is the same as $M \cap D$, one could express the likelihood as,

$$P(D|M) = \frac{P(D)P(M|D)}{P(M)} \tag{A.2}$$

One can have the total probability based on the three probability axioms, as

$$P(M) = \sum_i P(M \cap D_i) = \sum_i P(M|D_i)P(D_i) \tag{A.3}$$

Here i is the number of data. Therefore, the likelihood can be expressed as

$$P(D|M) = \frac{P(D)P(M|D)}{\sum_i P(M|D_i)P(D_i)} \tag{A.4}$$

P(M) is the prior probability for the theory, which interprets the degree of belief that the model M is true. If we set P(D)=1 (having collected the data) and ignore the prior, then we can identify the likelihood with P($M|D$), where P($D|M$) $\propto$ P($M|D$).

We can find the most likely model given the data by maximizing the likelihood. However, this approach with ignoring P(D) and the prior can not give in general a goodness of fit and thus can not give an absolute probability for a given model. It provides relative probabilities [137].

For the supernova rate analysis, we have 10 observations (SNR_i, z_i) with errors, and a model R_{SN}(z), described by a set of parameters ($R(0)$, β) as in Eq. 2.6. If the data are Gaussianly distributed, the probability of measuring SNR_i is,

$$P_i = \frac{1}{\sigma_i\sqrt{2\pi}} e^{-\frac{\left(SNR_i - SNR(z_i)\right)}{\sigma_i^2}} \tag{A.5}$$

The likelihood is just,

$$\mathscr{L} = \prod_{1=1}^{N=10} P_i \propto exp[-1/2\chi^2]. \tag{A.6}$$

To find the "true" value of the parameters, we search for those values that maximizing $\mathscr{L}$ and get the best model. There is another way to quantify the agreement of data and model with a least square function, which is, supposing the data are uncorrelated,

$$\chi^2 = \sum_{1}^{N=10} \left(\frac{SNR_i - SNR(z_i)}{\sigma_i}\right)^2 \tag{A.7}$$

In general, χ^2 is an indicator of the agreement of observed and expected values of some variables. We can see from above, $\mathscr{L} \propto exp[-1/2\chi^2]$. Therefore, minimizing χ^2 is equivalent to maximizing $\mathscr{L}$.

A.2 Confidence regions

After obtaining the best fit parameters, we could find the confidence region around the best fit parameters. In the n-dimensional parameter space, where k is the number of parameters, the confidence region is defined as the region that contains a given percentage of the probability distribution. If the values of the parameters are perturbed from the best fit, then χ^2 will increase by $\Delta\chi^2$. The probability that the observed χ^2 exceeds a value $\Delta\chi^2$ for the correct model is [138],

$$Q(k-n, \chi^2_{min} + \Delta\chi^2) = 1 - \Gamma((k-n)/2, (\chi^2_{min} + \Delta\chi^2)/2) = p \tag{A.8}$$

where Γ is the incomplete Gamma function, p is the confidence limit, χ^2_{min} is the minimum χ^2 value. Therefore, from this relation, we could find the $\Delta\chi^2$ for various confidence level, and the confidence region where $\chi^2 \leq \chi^2_{min} + \Delta\chi^2$. As example, Table A.1 gives the $\Delta\chi^2$ for 68.3, 90, 95.4% confidence levels for 1, 2, 5 parameter cases.

Table A.1: $\Delta\chi^2$ as a function of the number of parameters for 68.3, 90, 95.4% confidence levels.

p (%)	1	2	5
68.3	1.00	2.30	5.89
90	2.71	4.61	9.24
95.4	4.00	6.17	11.3

APPENDIX B

Cross section

B.1 Resonant cross section

The resonant neutrino-antineutrino annihilation ($\nu\bar{\nu} \to Z^0 \to f\bar{f}$) occurs in the s-channel, see Fig. B.1 for Feynman diagram. The cross section is expressed as a function of the Mandelstam variable, $s = (q^\mu + p^\mu)^2$. Here $q^\mu = [E',\ \mathbf{q}]$ and $p^\mu = [\sqrt{\mathbf{p}^2 + m_j^2},\ \mathbf{p}]$ are the four momenta of an UHE neutrino and background neutrinos, respectively. Since for UHE neutrinos $|\mathbf{q}| \gg m_{\nu_j}$, $E' \approx |\mathbf{q}| \equiv q$, then its four momentum is simply $q^\mu = E'[1, \hat{\mathbf{q}}]$. Note that in an expanding universe, we replace $E' = E(1+z)$ and $p = p_0(1+z)$, where E and p_0 are the values of the beam energy and background neutrino momentum at present epoch, respectively. Then, the Mandelstam variable, s, in the comoving frame is:

$$s(E', p, \theta) \approx 2E' \left[\sqrt{p^2 + m_j^2} - p\cos\theta \right], \tag{B.1}$$

where $\hat{\mathbf{q}} \cdot \mathbf{p} \equiv p\cos\theta$. The differential cross section for the resonant s-channel is [106]

$$d\sigma_{\rm r}(E', p, s) = \frac{G_F \Gamma M_Z}{\sqrt{2} E' \sqrt{p^2 + m_{\nu_j}^2}} \frac{s(s - 2m_{\nu_j}^2)}{(s - M_Z^2)^2 + \xi s^2} ds, \tag{B.2}$$

where $G_F = 1.16637 \times 10^{-5}$ GeV^{-2} is the Fermi coupling constant, $M_Z = 91.1876$ GeV, $\Gamma = 2.495$ GeV is the width of the Z^0 resonance, $\xi = \Gamma^2/M_Z^2$. The total resonant cross section is obtained by integrating over s:

$$\sigma_{\rm r}(E', p) = \int_{s_-}^{s_+} d\sigma_{\rm r}(E', p, s), \tag{B.3}$$

where $s_\pm \equiv 2E' \left[\sqrt{p^2 + m_j^2} \pm p \right]$ corresponding to head-on and parallel scattering, respectively. Eq. (B.3) can be expressed in an analytical form [106]

$$\begin{aligned} \sigma_{\rm r}(E', p) \;&=\; \frac{G_F \Gamma M_Z}{\sqrt{2} E' \sqrt{p^2 + m_{\nu_j}^2}} \left[\frac{s}{1+\xi} - \frac{M_Z^2(\xi - 1)}{\sqrt{\xi}(1+\xi)^2} \arctan\left(\frac{(1+\xi)\, s - M_Z^2}{M_Z^2 \sqrt{\xi}} \right) \right. \\ &+\; \left. \frac{M_Z^2}{(1+\xi)^2} \ln\left[(1+\xi) s^2 - 2M_Z^2 + M_Z^4 s \right] \right] \Bigg|_{s_-}^{s_+}, \end{aligned} \tag{B.4}$$

where we take $s - 2m_{\nu_f}^2 \approx s$. The resonant cross section $\sigma_{\rm r}(E', p)$ includes all kinematically allowed final states ($\bar{q}q, \bar{l}l$), which is taken into account in the width Γ.

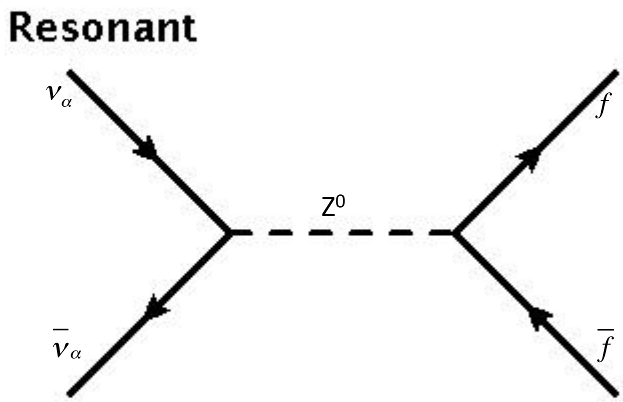

Figure B.1: Feynman diagram of resonant cross section.

B.2 Non-resonant cross sections

Non-resonant cross sections are smooth functions of the beam energy E', thus it is a very good approximation to use the value of s, averaged over scattering angle and momenta of the background neutrinos, instead of Eq. (B.1), to simplify the analysis:

$$\bar{s}(E', m_j) \equiv 2E'\sqrt{\bar{p}^2 + m_j^2}. \tag{B.5}$$

All the relevant non-resonant processes are summarized as follows [104, 107]:

(1). The t-channel Z-exchange ($\nu_\alpha \bar{\nu}_\beta \to \nu_\alpha \bar{\nu}_\beta$) cross section with multiplicity 3 (including 3 different flavors for the target neutrino) is:

$$\sigma_{tZ} = 3\frac{G_F^2 \bar{s}(E', m_j)}{2\pi} F_1(y_Z), \tag{B.6}$$

where $F_1(y) = [y^2 + 2y - 2(1+y)\ \ln(1+y)]/y^3$ and $y_Z = \bar{s}(E', m_j)/M_Z^2$.

(2). For $\alpha = \beta$, there is an s-t interference term with multiplicity 1:

$$\sigma_{stZ} = \frac{G_F^2 \bar{s}(E', m_j)}{4\pi} F_2(y_Z) \frac{y_Z - 1}{(y_Z - 1)^2 + \Gamma^2/M_Z^2}, \tag{B.7}$$

where $F_2(y) = [3y^2 + 2y - 2(1+y)^2 \ln(1+y)]/y^3$.

(3). The t-channel W-exchange ($\nu_\alpha \bar{\nu}_\beta \to l_\alpha \bar{l}_\beta$) cross section with multiplicity 3 is:

$$\sigma_{tW} = 3\frac{2G_F^2 \bar{s}(E', m_j)}{\pi} F_1(y_W), \tag{B.8}$$

where $y_W = \bar{s}(E', m_j)/M_W^2$ and $M_W = 80.385$ GeV.

(4). For $\alpha = \beta$, there is an interference between the s-channel Z-exchange and the t-channel W-exchange is with multiplicity 1:

$$\sigma_{stZW} = \frac{2G_F^2(\sin^2\theta_W - 1/2)}{\pi} y_W M_W^2 F_2(y_W) \frac{y_Z - 1}{(y_Z-1)^2 + \Gamma^2/M_Z^2}\,, \tag{B.9}$$

where $\sin^2\theta_W = 0.23149$.

(5). The elastic t-channel Z-exchange ($\nu_\alpha \nu_\beta \to \nu_\alpha \nu_\beta$) cross section with multiplicity 3 is:

$$\sigma_{tZ}^{\mathrm{el}} = 3\frac{2G_F^2 M_Z^2}{2\pi} \frac{y_Z}{1+y_Z}. \tag{B.10}$$

(6). There is also the u-channel Z-exchange that contributes to the same process ($\nu_\alpha \nu_\beta \to \nu_\alpha \nu_\beta$) with multiplicity 1:

$$\sigma_{uZ} = \frac{2G_F^2 \bar{s}(E', m_j)}{\pi} \left[\frac{1}{1+y_Z} + \frac{\ln(1+y_Z)}{y_Z(1+y_Z/2)}\right]. \tag{B.11}$$

(7). The weak charged vector boson pair production cross section in the s-channel Z-exchange and the t-channel l-exchange ($\nu_\alpha \bar{\nu}_\alpha \to W^+W^-$) with multiplicity 1 and threshold $s > 4M_W^2$ is:

$$\begin{aligned} \sigma_{WW} &= \frac{G_F^2 y_W M_W^2 \beta_W}{12\pi}\left[\frac{\beta_W^2 M_W^4}{M_Z^4(y_Z-1)^2}(12 + 20y_W + y_W^2)\right. \\ &+ \frac{2M_W^2}{M_Z^2(y_Z-1)y_W^2}\left(24 + 28y_W - 18y_W^2 - y_W^3 + \frac{48(1+2y_W)L_W}{\beta_W y_W}\right) \\ &+ \left.\frac{1}{y_W^2}\left(y_W^2 + 20y_W - 48 - \frac{48(2-y_W)L_W}{\beta_W y_W}\right)\right], \end{aligned} \tag{B.12}$$

where $\beta_W = \sqrt{1-4/y_W}$ and $L_W = \ln[(1+\beta_W)(1-\beta_W)]$.

(8). The weak neutral vector boson pair production cross section in the s-channel ($\nu_\alpha\bar{\nu}_\alpha \to ZZ$) with multiplicity 1 and threshold $s > 4M_Z^2$ is:

$$\sigma_{ZZ} = \frac{G_F^2 M_Z^2}{\pi}\frac{\beta_Z}{y_Z-2}\left(\frac{2}{y_Z} - 1 + \frac{1+y_Z^2}{2y_Z^2\beta_Z}L_Z\right), \tag{B.13}$$

where $\beta_Z = \sqrt{1-4/y_Z}$ and $L_Z = \ln[(1+\beta_Z)(1-\beta_Z)]$.

(9). Finally, ZH production cross section in the s-channel ($\nu_\alpha\bar{\nu}_\alpha \to Z^0 H$) with multiplicity 1 and threshold $s > (M_Z+M_H)^2$ is:

$$\sigma_{ZH} = \frac{G_F^2 M_Z^2}{96\pi}\frac{\sqrt{\lambda}\beta_Z}{y_Z}\frac{\lambda y_Z + 12}{(y_Z-1)^2}, \tag{B.14}$$

where $\lambda = [1-(M_H+M_Z)^2/(y_Z M_Z^2)][1-(M_H-M_Z)^2/(y_Z M_Z^2)]$ and $M_H = 125$ GeV. The total cross section is the sum of all the resonant and non-resonant channels, as shown in Fig. 4.1.

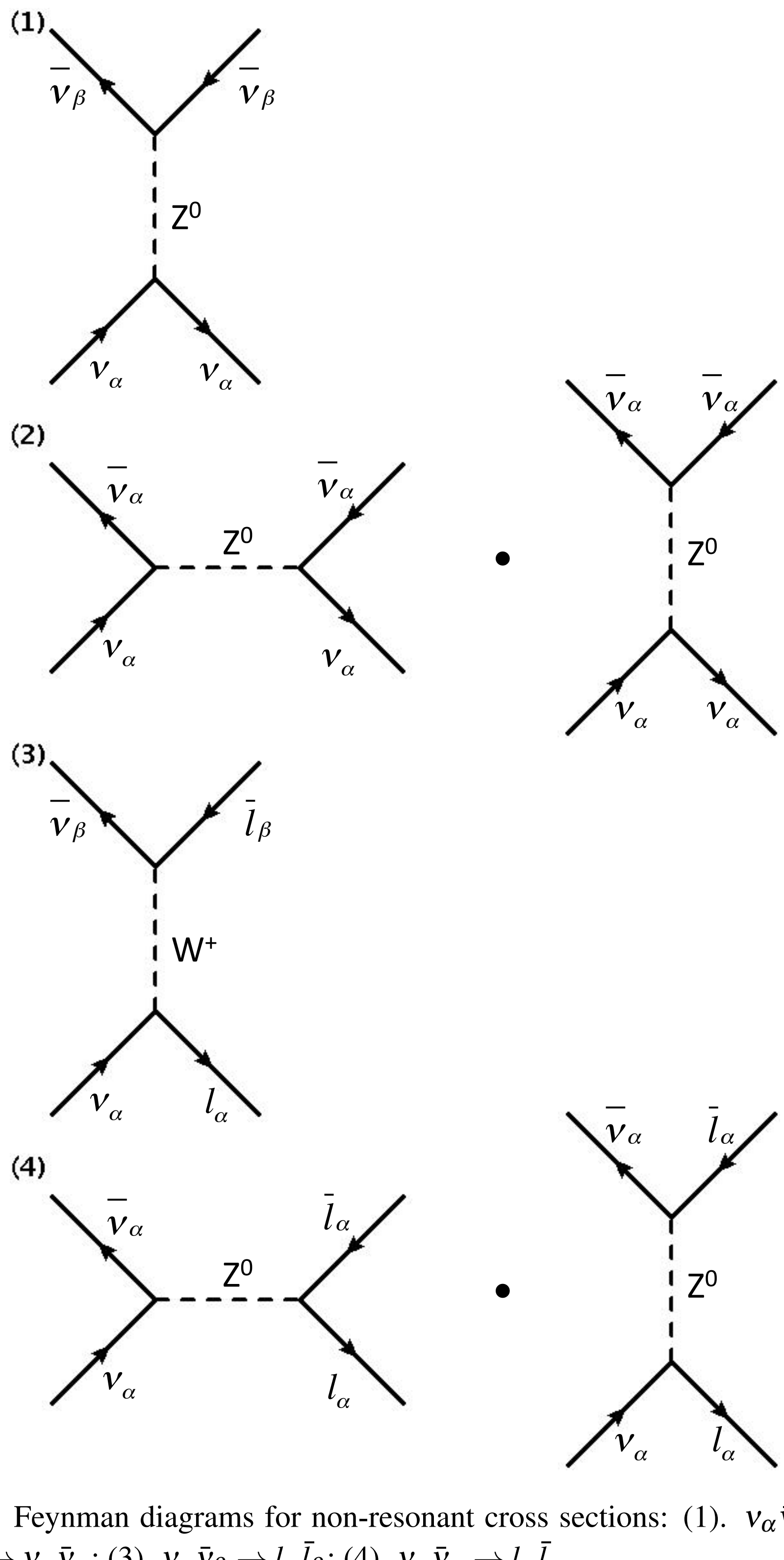

Figure B.2: Feynman diagrams for non-resonant cross sections: (1). $\nu_\alpha \bar{\nu}_\beta \to \nu_\alpha \bar{\nu}_\beta$; (2). $\nu_\alpha \bar{\nu}_\alpha \to \nu_\alpha \bar{\nu}_\alpha$; (3). $\nu_\alpha \bar{\nu}_\beta \to l_\alpha \bar{l}_\beta$; (4). $\nu_\alpha \bar{\nu}_\alpha \to l_\alpha \bar{l}_\alpha$

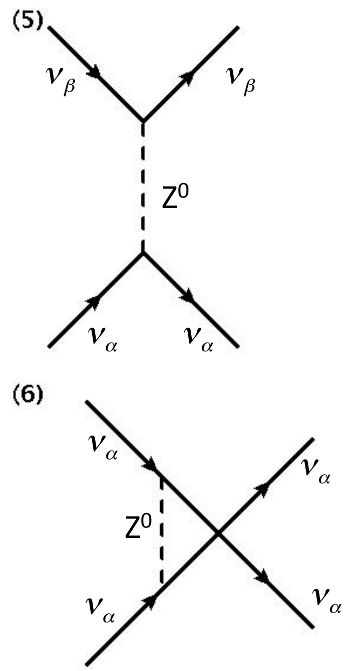

Figure B.3: Feynman diagrams for non-resonant cross sections: (5). $\nu_\alpha \nu_\beta \to \nu_\alpha \nu_\beta$; (6). $\nu_\alpha \nu_\beta \to \nu_\alpha \nu_\beta$

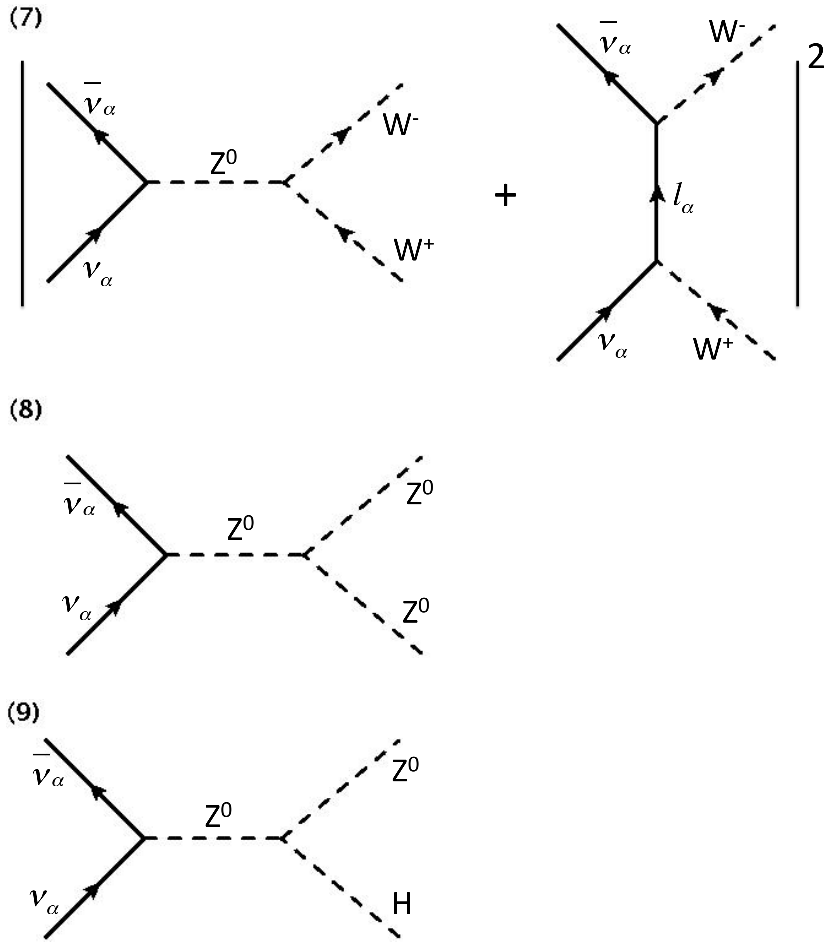

Figure B.4: Feynman diagrams for non-resonant cross sections: (7). $\nu_\alpha \bar{\nu}_\alpha \to W^+W^-$; (8). $\nu_\alpha \bar{\nu}_\alpha \to ZZ$; (9). $\nu_\alpha \bar{\nu}_\alpha \to Z^0H$

APPENDIX C

Scattering amplitude and rate

In this appendix, we schematically show the dependence of the scattering rate on the neutrino mixing matrix for an UHE neutrino in a flavor eigenstate ν_α and a CνB neutrino in a mass eigenstate ν_j, given by Eq. (4.13). For simplicity, consider the scattering amplitude for the s-channel process, $\nu_\alpha \bar{\nu}_j \to f \bar{f}$, where f is a final state fermion. The scattering amplitude $M_{\alpha j}$ is proportional to

$$M_{\alpha j} \propto \langle \bar{\nu}_j | O | \nu_\alpha \rangle = \sum_i U^*_{\alpha i} \, e^{-i\Phi_i(t)} \, \langle \bar{\nu}_j | O | \nu_i \rangle \ , \tag{C.1}$$

where $U^*_{\alpha i}$ are the elements of the neutrino mixing matrix and $\Phi_i(t) = \int_{t_i}^{t} dt' \, \sqrt{[p(t')]^2 + m_i^2}$ is the quantum phase due to the neutrino propagation in vacuum between the time of production, t_i, and the time t when the collision occurs. This phase is responsible for neutrino flavor oscillations.

In Eq. (C.1), the nonvanishing elements are the diagonal ones, i.e., $\langle \bar{\nu}_i | O | \nu_j \rangle \propto \delta_{ij} M_j$. Hence,

$$M_{\alpha j} \propto U^*_{\alpha j} \, e^{-i\Phi_i(t)} \, \langle \bar{\nu}_j | O | \nu_j \rangle \propto U^*_{\alpha j} \, e^{-i\Phi_i(t)} M_j \ . \tag{C.2}$$

The corresponding cross section is then $\sigma(m_j) \propto |M_j|^2$. Note that the phase Φ_j cancels, hence neutrino oscillations do not affect the cross section provided that the background neutrino is in mass eigenstate as we discussed in Sec. 4.2.2. Then, given dn as the number density of the CνB neutrinos of each species, we have the scattering rate for an UHE neutrino of flavor α in the CνB for a given process:

$$d\Gamma_\alpha = dn \sum_{j=1}^{3} |U_{\alpha j}|^2 \sigma(m_j), \tag{C.3}$$

which, after integration over the neutrino spectrum, recovers Eq. (4.13).